Trapped Positrons for High-Precision Magnetic Moment Measurements

A thesis presented

by

Shannon Michelle Fogwell Hoogerheide

to

The Department of Physics

in partial fulfillment of the requirements

for the degree of

Doctor of Philosophy

in the subject of

Physics

Harvard University

Cambridge, Massachusetts

May 2013

Thesis advisor

Gerald Gabrielse

Author

Shannon Michelle Fogwell Hoogerheide

Trapped Positrons for High-Precision Magnetic Moment Measurements

Abstract

A single electron in a quantum cyclotron provides the most precise measurement of the electron magnetic moment, given in units of the Bohr magneton by $g/2 = 1.001\ 159\ 652\ 180\ 73\ (28)$ [0.28 ppt]. The most precise determination of the fine structure constant comes from combining this measurement with Standard Model theory, yielding $\alpha^{-1} = 137.035\ 999\ 173\ (34)$ [0.25 ppb], limited by the experimental uncertainty of the electron g-value. The most stringent test of CPT symmetry in leptons comes from comparing the electron and positron magnetic moments, limited by the positron uncertainty at 4.2 ppt. A new high-stability apparatus has been built and commissioned for improved measurements of the electron and positron magnetic moments, a greatly improved test of lepton CPT symmetry, and an improved determination of the fine structure constant. These new measurements require robust positron loading from a retractable radioactive source that is small enough to avoid compromising the high-precision environment of our experiment. The design and implementation of such a scheme is a central focus of this work. Robust positron loading at a rate of 1-2 e^+/min from a 6.5 μCi ^{22}Na source has been demonstrated.

Contents

List of Figures

List of Tables

Papers and Publications

1. "New measurement of the electron magnetic moment and fine structure constant,"
   D. Hanneke, S. Fogwell and G. Gabrielse, *Phys. Rev. Lett.* **100**, 120801 (2008).

2. "Cavity control of a single-electron quantum cyclotron: Measuring the electron magnetic moment,"
   D. Hanneke, S. Fogwell Hoogerheide, and G. Gabrielse, *Phys. Rev. A* **83**, 052122 (2011).

3. "More accurate measurement of the electron magnetic moment and the fine structure constant,"
   D. Hanneke, S. Fogwell, N. Guise, J. Dorr, and G. Gabrielse, *Pushing the Frontiers of Atomic Physics: Proceedings of the XXI International Conference on Atomic Physics*, World Scientific, 46-55 (2009).

4. "Testing the Standard Model with Matter and Antimatter,"
   G. Gabrielse, S. Fogwell Hoogerheide, J. C. Dorr, and E. Novitski, *Precision Spectroscopy in Ion Traps for Fundamental Physics*, Springer, in preparation.

Acknowledgments

This thesis has been many years in the making and would not have been possible without the support of many people, for whom I am very grateful. First of all I would like to thank my adviser Professor Jerry Gabrielse for his enthusiasm for the project and for his guidance and suggestions as the project suffered numerous set-backs. I also thank him for his continued support and encouragement as I developed into a confident and competent researcher.

I am also indebted to my colleagues for their knowledge, help and friendship. I am grateful for David Hanneke who taught me much of what I know about the experiment and with whom I had the privilege of working on our 2008 result. Josh Dorr provided unlimited assistance as we constructed the new apparatus and dealt with all of its quirks and problems. I thank him for his help, support and perseverance as we wondered whether the new apparatus would ever work properly. I also thank him for his help and support in taking the data for this thesis. I thank Elise Novitski for her work setting up the reliquifier, taking the lead on getting the new pinbase made, and for helping with the data in this thesis. The results presented here would not have been possible without help from Josh and Elise and I know I am leaving the experiment in good hands.

I also want to particularly thank Josh Goldman who was involved in the wiring and testing of the apparatus after the decision was made to house two experiments in a single apparatus. I thank him for all of his assistance in getting the apparatus working and for his encouragement and support when things weren't going well. And I thank Nick Guise and Jack DiSciacca for offering advice on getting the new apparatus working and on constructing amplifiers, and also for providing helpful discussions on

various aspects of each of our experiments.

I am also thankful for all of the graduate students and postdocs in lab with whom I have had the pleasure of working — Dan Farkas, David LeSage, Phil Larochelle, Steve Kolthammer, Rob McConnell, Yulia Gurevich, Ben Levitt, Jonathon Wrubel, Maarten Jansen, Irma Kuljanishvili, Ben Spaun, Paul Hess, Rita Kalra, Mason Marshall, Kathryn Marable, Nate Jones, Eric Tardiff, and Stephan Ettenauer.

I thank my committee members, Professor Ike Silvera and Professor Vinny Manoharan for their support and helpful comments along the way. I am grateful for my mentor, Professor Jenny Hoffman who provided invaluable support, guidance, encouragement, and helpful conversations over the last several years and for believing that I could succeed.

Thanks to Jan Ragusa for always making being there to help when I needed her, including making sure that forms and letters and applications always got submitted on time and for finding the combination to the radioactive source storage safe when all hope seemed lost. Thanks to Stan Cotreau for encouraging me to come to the machine shop and teaching me everything I know about machining. Thanks to Jim MacArthur for helping with all of my electronics questions. Thanks also to Louis DeFeo and the machinists in his shop including Al and Rich for their excellent work in machining the majority of my experiment. And thanks to all of the others in the physics department who have provided their help and support. The National Science Foundation provided support for this project and the Harvard Center for Nanoscale Systems provided equipment for thermal evaporation.

Finally, I am grateful to my many family and friends who have supported me

throughout my graduate school endeavor and without whom I would not have gotten this far. In particular I'd like to thank my parents, Norm Fogwell and Patti Wood for their continued love and support and encouragement to pursue my goals and my husband, Dave Hoogerheide for his unwavering support, love and encouragement, and understanding and patience as I finished.

Chapter 1

Introduction

The most precisely measured property of an elementary particle is the magnetic moment of the electron [1, 2]. This thesis work includes a substantial contribution to making this 3 parts in 10^{13} measurement, followed by the building and commissioning of an entirely new apparatus, including a positron loading scheme compatible with the high-precision environment, to enable more precise measurements with an electron or positron.

This chapter introduces the electron and positron magnetic moments and the importance of our electron measurement for providing the most stringent test of the Standard Model. The incredible agreement of the measured and predicted values of the electron magnetic moment is perhaps the greatest triumph of the Standard Model. Our measurement of the electron g-value combined with a Standard Model calculation also provides the most precise value of the fine structure constant. A comparison of the magnetic moments of the electron and positron, which we hope to improve with a new measurement in the new apparatus, will provide the best test of

CPT invariance in a lepton system.

Following chapters focus on the apparatus and quantum methods used for the measurement. A particular focus is on the new apparatus built not only to make better electron measurements possible, but also to make possible single positron measurements. Positron loading from a very weak and retractable source, required for extremely precise positron measurements, was demonstrated and characterized.

1.1 The Magnetic Moment of the Electron

The magnetic moment of a spin one-half particle of charge $-e$ and mass m can be written as

$$\vec{\mu} = \mu\vec{\sigma} = -\frac{g}{2}\frac{e\hbar}{2m}\frac{\vec{S}}{\hbar/2}, \tag{1.1}$$

where $\vec{S} = \frac{1}{2}\hbar\vec{\sigma}$ is the angular momentum and g is a dimensionless factor called the g factor or g-value. For a mechanical model with identical charge and mass distributions, g would be equal to exactly 1. For a Dirac point particle, g would be equal to exactly 2. The interaction of the electron (or positron) with the vacuum, as described by quantum electrodynamics (QED), yields a value of g for an electron (or positron) that is slightly greater than 2 by roughly one part-per-thousand. This deviation from 2 is called the anomalous magnetic moment, or the anomaly, a_e, defined by $g/2 = 1 + a_e$. A measurement of the electron g-value provides a precise test of Dirac theory and QED.

1.1.1 Magnetic Moment History and Future

The idea that the electron spin must have a g-value twice that for orbital angular momentum was postulated in 1926 by Uhlenbeck and Goudsmit[3]. Dirac's theory [4, 5], published in 1928 also predicted $g = 1$ for orbital angular momentum and $g = 2$ for spin. Early experiments were in agreement with Dirac's theory that $g = 2$ for spin. In 1947, Kusch and Foley discovered the electron anomaly and measured it to be $a_e = 0.00115\,(4)$ [6]. That same year Schwinger predicted that there was a small additional component of the electron g-factor and calculated it to be $a_e = \alpha/2\pi \simeq 0.00116...$ [7]. Thus began a long series of experimental and theoretical advances in determining the value of the electron anomaly, each driving the other to ever higher precision, that continue today. The early history is reviewed in [8] and [9, Ch. 1-3].

The isolation of a single electron in a Penning trap [10] was a major step forward, initiating a new string of g-value measurements at the University of Washington, culminating in the 1987 measurement of the electron and positron g-values at 4.3 ppt [11]. The next step forward came from realizing quantum cyclotron motion. This was accomplished by cooling the cyclotron motion to its ground state within a trap cavity that inhibited spontaneous emission enough so that single quantum transitions could be detected. New methods were used to characterize the cavity well enough to correct for the corresponding shifts of the cyclotron frequency, which otherwise would have limited the measurement precision. The first fully-quantum measurement of the electron magnetic moment yielded a measurement of the electron g-value at 0.76 ppt [12]. Combining all of these features, along with additional work on understanding and correcting the cavity modes, including using the single electron to map out the

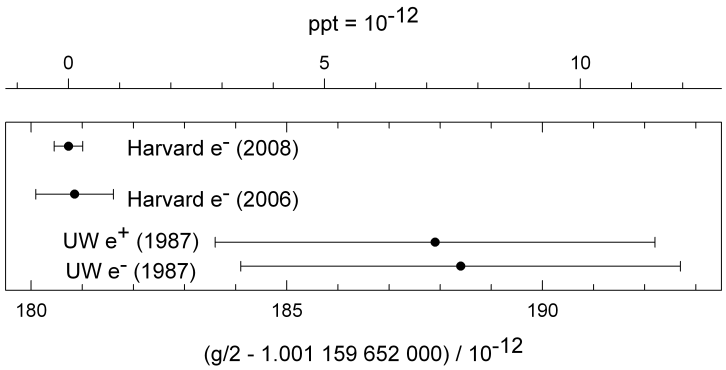

Figure 1.1: Comparison of most accurate electron and positron g-value measurements

mode coupling allowed us to make the most precise measurement of the electron g-value at 0.28 ppt [1]. A comparison of these measurements of the electron and positron g-value is shown in Fig. 1.1.

We have now built a new, high-stability apparatus that can load positrons and take advantage of these recent advances to make an improved measurement of the positron g-value. The next major step may come from cooling the axial motion to the quantum mechanical ground state (this idea will be discussed in Section 7.2.1).

1.2 The Standard Model Relates $g/2$ and α

The standard model gives the g-value as an expansion in powers of the fine structure constant,

$$\frac{g}{2} = 1 + A_2\left(\frac{\alpha}{\pi}\right) + A_4\left(\frac{\alpha}{\pi}\right)^2 + A_6\left(\frac{\alpha}{\pi}\right)^3 + A_8\left(\frac{\alpha}{\pi}\right)^4 + A_{10}\left(\frac{\alpha}{\pi}\right)^5 + ... + a_{\mu,\tau} + a_{\text{hadronic}} + a_{\text{weak}}. \tag{1.2}$$

The first term comes from the Dirac equation and the A_k coefficients are calculated using QED. The $a_{\mu,\tau}$ term encompasses additional QED coefficients involving interac-

tions with μ and τ leptons. The a_{hadronic} term includes all of the hadronic contributions and the a_{weak} term includes all of the contributions from the weak force. The first three A_k coefficients have been calculated analytically and are given by

$$A_2 = \frac{1}{2} = 0.5 \qquad \text{1 Feynman Diagram [7]} \tag{1.3a}$$

$$\begin{aligned} A_4 &= \frac{197}{144} + \frac{\pi^2}{12} + \frac{3}{4}\zeta(3) - \frac{1}{2}\pi^2 \ln 2 \qquad \text{7 Feynman Diagrams [13, 14, 15]} \\ &= -0.328\,478\,965\,579\ldots \end{aligned} \tag{1.3b}$$

$$\begin{aligned} A_6 = {} & \frac{83}{72}\pi^2\zeta(3) - \frac{215}{24}\zeta(5) \qquad \text{72 Feynman Diagrams [16]} \\ & + \frac{100}{3}\left[\left(\sum_{n=1}^{\infty}\frac{1}{2^n n^4} + \frac{1}{24}\ln 2^4\right) - \frac{1}{24}\pi^2 \ln 2^2\right] \\ & - \frac{239}{2160}\pi^4 + \frac{139}{18}\zeta(3) - \frac{298}{9}\pi^2 \ln 2 + \frac{17101}{810}\pi^2 + \frac{28259}{5184} \\ = {} & 1.181\,241\,456\ldots. \end{aligned} \tag{1.3c}$$

Both A_8 and A_{10} are calculated numerically,

$$A_8 = 1.910\,6\,(20) \qquad \text{891 Feynman Diagrams [17, 18]} \tag{1.4a}$$

$$A_{10} = 9.16\,(58) \qquad \text{12\,672 Feynman Diagrams [17, 18]} \tag{1.4b}$$

Although some of the diagrams for these higher order terms have been calculated analytically, a full analytical calculation of the A_8 or A_{10} terms is not currently available [18].

The $a_{\mu,\tau}$ term encompasses QED terms involving μ and τ leptons. These come in at 4th order and higher in the QED expansion given in Eq. 1.2. The 4th and 6th order terms have been calculated analytically [19], with uncertainty due only to the measured mass ratios, m_e/m_μ and m_e/m_τ. The 8th order terms and the muon

contribution to the 10th order term have been calculated numerically [17]. Combining all of the terms and using the latest mass-ratios [20] yields

$$a_{\mu,\tau} = 2.747\,8\,(3) \times 10^{-12}. \tag{1.5}$$

The hadronic term is calculated using experimentally measured scattering cross-sections because the QCD calculations are too difficult. The combined vacuum polarization and light-by-light scattering effects give a hadronic term

$$a_{\text{hadronic}} = 1.678\,(15) \times 10^{-12}. \tag{1.6}$$

This contribution is important at the current level of precision, although the uncertainty currently remains negligible. The weak contribution, found by calculating the effect of the weak force on the muon $g-2$ and then scaling it down for the electron $g-2$, is given by

$$a_{\text{weak}} = 0.029\,7\,(5) \times 10^{-12}. \tag{1.7}$$

The weak contribution is currently smaller than the experimental precision, but an order of magnitude improvement in the precision of the electron g-value measurement — which may be possible in our new apparatus using some new techniques — will begin to probe the weak contribution. The relative contributions and uncertainties of all the various terms in Eq. 1.2 can be seen in Figure 1.2.

Our 2008 measurement of the electron g-value yielded [1, 2]

$$\frac{g}{2} = 1.001\,159\,652\,180\,73\,(28)\ [0.28\,\text{ppt}] \tag{1.8}$$

which at the time gave

$$\alpha^{-1} = 137.035\,999\,084\,(51)\ [0.37\,\text{ppb}]. \tag{1.9}$$

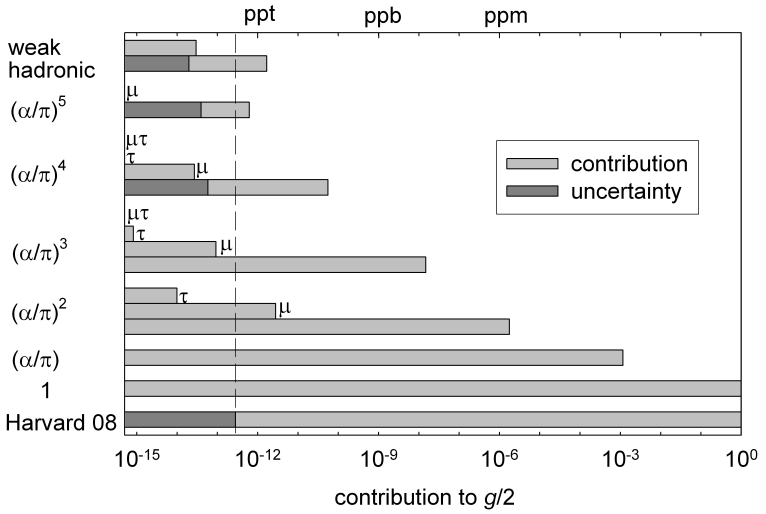

Figure 1.2: Contributions and uncertainties of the various terms to $g/2$.

The new improvements in the theoretical calculations as described above shift our value of α and decrease the error bar, with the new result of

$$\alpha^{-1} = 137.035\,999\,173\,(33)\,(8)\ [0.24\,\text{ppb, exp.}]\,[0.06\,\text{ppb, th.}] \tag{1.10}$$

$$= 137.035\,999\,173\,(34)\ [0.25\,\text{ppb}] \tag{1.11}$$

where most of the uncertainty now comes from our measurement of the g-value. (Prior to the 2012 theoretical advances, the largest uncertainty came from the theory). The relative contributions of experiment and theory can be seen in Fig. 1.3.

The best test of QED comes from combining the theoretical calculations with an independent measurement of α and comparing to the experimentally measured electron g-value. This will be discussed in Section 1.3. Comparing the value of α from our measurement plus QED theory to an independent measurement also sets limits on new physics such as possible electron sub-structure or physics beyond the standard model.

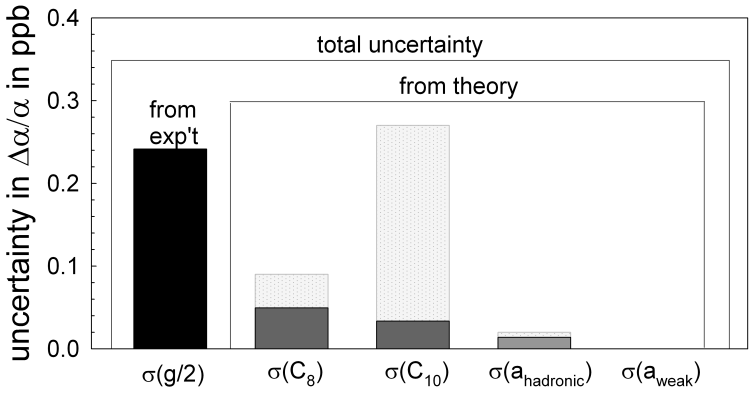

Figure 1.3: Experimental and theoretical contributions to the current best determination of α. The light gray bars show the uncertainty in the theory terms prior to the 2012 theoretical advance.

1.3 Other Measurements of α

As mentioned above, an independent determination of α is needed to fully test the predictions of QED using the electron g-value measurement. There are a number of different methods for measuring the fine structure constant, the most precise of which are discussed below.

1.3.1 Atom-recoil Experiments

The most precise determinations of the fine structure constant, apart from the electron g-value measurement, currently come from the so-called atom-recoil experiments. In particular, the current best independent measurement of α comes from the rubidium atom-recoil experiments [21].

In the atom-recoil experiments, a measurement of h/m_X, where m_X is the mass of the atom used in the experiments, is used to determine the fine structure constant

by the relation

$$\alpha^2 = \frac{2R_\infty}{c}\frac{m_X}{m_e}\frac{h}{m_X}. \tag{1.12}$$

The Rydberg constant, R_∞, and the mass ratio m_X/m_e are known with a high degree of precision from other experiments [20, 22, 23]. The limiting factor in using this equation to determine α is the ratio h/m_X.

These types of experiments have been performed using both cesium and rubidium. The cesium experiments involve precise optical measurements of two D_1 transitions in cesium [24] and a measurement of the recoil velocity of the atom when it absorbs a photon resonant with one transition and emits a photon resonant with the other transition. This recoil velocity is given by a frequency shift in an atom interferometer [25]. The most accurate measurement to date gives α to 8.0 ppb [24, 25], with plans for an improved measurement [26].

A series of rubidium experiments have been performed, the most recent of which use rubidium atoms confined in an optical lattice. Bloch oscillations are used to impart a large number of momentum kicks to the atoms. A Ramsey-Bordé interferometer is used to measure the resulting velocity distribution of the atoms. The result of the most recent 2011 measurement [21], when updated to use the 2010 CODATA values of R_∞ and m_{Rb}/m_e [20] is

$$\alpha^{-1}(\mathrm{Rb}) = 137.035\,999\,041\,(90)\,[0.65\,\mathrm{ppb}], \tag{1.13}$$

which is currently the best independent measurement of the fine structure constant and 2.6 times less precise than our measurement as can be seen in Fig. 1.4.

Because these atom-recoil measurements depend on the value of the Rydberg constant, the ultimate resolution of the current proton-radius puzzle [27, 28] has the

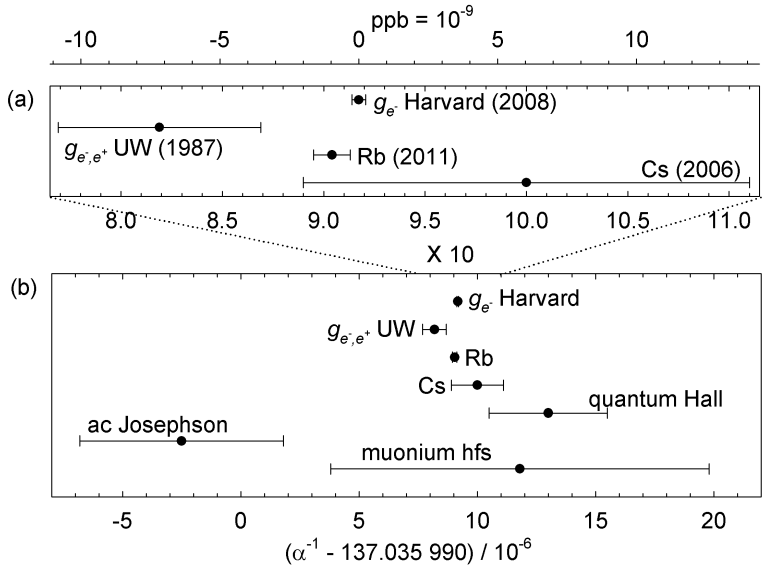

Figure 1.4: A comparison of various determinations of the fine structure constant. (a) shows the most precise determinations as discussed in the text. (b) is a zoomed-out view to include other determinations of α.

potential to slightly alter the value of α extracted from these measurements. For example, the most recent measurements in muonic hydrogen [27, 28] suggest a proton charge radius that is 7σ away from the 2010 CODATA value [20] which comes mainly from hydrogen spectroscopy. If this is correct, it would give a value of the Rydberg constant that is also shifted from the 2010 CODATA value by nearly 7σ. However, given the current precision of the h/m_{Rb} measurement, this would only change the last digit in $\alpha^{-1}(\mathrm{Rb})$ by 3 and would not change the uncertainty since the uncertainty in the measurement of h/m_{Rb} is much higher than the discrepancy in the value of R_∞. As the precision of h/m_{Rb} increases, this discrepancy in R_∞, if still unresolved, may become more significant.

1.3.2 Other Determinations of α

Other less precise methods determine a value of the fine structure constant as tabulated in [20, Sec. XIII] and plotted in Fig. 1.4. These values of α are determined from measurements involving the quantum Hall effect and the AC Josephson effect as well as measurements of transition frequencies in muonium. Where multiple values are given in [20, Table XXV], the weighted average is given in Fig. 1.4.

One additional way to extract a value of the fine structure constant is to use the measured values of the various 1S-2S transition frequencies in hydrogen. This is done in the CODATA analysis [20] with the result $\alpha^{-1} = 137.036\,003\,(41)\,[300\,\text{ppb}]$ in good agreement with our value, although much less precise than any of the values included in Fig. 1.4. Including the recent proton radius value as determined from muonic hydrogen spectroscopy gives $\alpha^{-1} = 137.035\,881\,(35)\,[260\,\text{ppb}]$ which differs from our value by several σ.

1.4 Testing QED and Physics Beyond the Standard Model

A measurement of the electron g-value combined with an independent determination of α provides the most precise test of QED. The excellent agreement between the measurements and theory is arguably the greatest triumph of the Standard Model. This comparison also places limits on new physics beyond the standard model, including possible electron substructure.

1.4.1 Testing QED

The most stringent test of QED comes from a comparison of our measurement of the electron g-value with an independent determination of the fine structure constant through Eq. 1.2. This comparison tests QED insofar as it tests the QED calculations that go into the determination of the coefficients in the expansion. Typically this comparison is done by computing a theoretical g-value (or anomaly, a_e) using the QED expansion plus the independent measurement of α and comparing this to the measured electron g-value. Combining the 2011 Rb value of the fine structure constant with the theoretical calculations of the terms in Eq. 1.2 yields a theoretical value for the electron g-value,

$$\frac{g}{2}(\text{theory}) = 1.001\,159\,652\,181\,84\,(76)\,[0.76\,\text{ppt}]. \tag{1.14}$$

The uncertainty in this theoretical value of $g/2$ is almost entirely due to the error in the measurement of α. The comparison to our 2008 measurement of the g-value, given in Eq. 1.8, yields

$$\frac{g}{2} - \frac{g}{2}(\text{theory}) = (-1.11 \pm 0.81) \times 10^{-12}, \tag{1.15}$$

with a difference bounded by

$$|\delta g/2| < 2.0 \times 10^{-12}. \tag{1.16}$$

The uncertainty in the comparison (and thus the size of the bound) is mostly due to the uncertainty in the rubidium atom-recoil measurement of α so further improvement there will enable a more stringent test. We can also compare the measured α from the rubidium experiment to the calculated value of α from our g-value measurement

and the QED expansion. This yields

$$\frac{\alpha^{-1} - \alpha^{-1}(\mathrm{Rb})}{\alpha^{-1}} = (9.6 \pm 6.9) \times 10^{-10}. \tag{1.17}$$

It will be interesting to see what happens to these comparisons with the new g-value measurements we hope to perform and as the precision in other measurements of α also increase.

1.4.2 Electron Substructure

The bound on $\delta g/2$ also sets the limit on any additional terms a_{new} in Eq. 1.2. As such, the bound on $\delta g/2$ sets a limit on any possible electron substructure. A naive first assumption about a composite electron would be to assume that the electron has such a small spatial extent because it is tightly bound to a very massive internal particle with mass m^*. This would give a contribution to the electron g-value [29],

$$\delta g/2 \sim \mathcal{O}\left(\frac{m_e}{m^*}\right). \tag{1.18}$$

If we define this contribution to be

$$|\delta g/2| = \frac{m_e}{m^*} \tag{1.19}$$

with the electron radius defined as

$$R_e = \hbar/\left(m^* c\right), \tag{1.20}$$

we get a limit on the mass of the composite particle to be

$$m^* > 260,000\mathrm{TeV/c^2} \tag{1.21}$$

and the radius to be

$$R_e < 8 \times 10^{-25}\text{m}. \tag{1.22}$$

The problem with this assumption that the contribution to the g-value is linear in mass is that in order to get the very small observed mass of the electron with such a large constituent particle you have to have a very fortuitous cancellation. A more natural choice might be a chirally invariant model that would give [29]

$$\delta g/2 \sim \frac{m_e^2}{m^{*2}}. \tag{1.23}$$

This yields limits of

$$m^* = \frac{m_e}{\sqrt{\delta g/2}} > 360\,\text{GeV/c}^2 \tag{1.24}$$

and

$$R_e = \frac{\hbar}{m^* c} < 5 \times 10^{-19}\,\text{m}. \tag{1.25}$$

If the bound on $\delta g/2$ was set entirely by the uncertainty in our g-value measurement, then we could set a limit of $m^* > 1\,\text{TeV/c}^2$ and $R_e < 2 \times 10^{-19}\,\text{m}$. The Large Electron-Positron collider (LEP) probed for contact interactions at $E = 10.3$ TeV [30], [31, pp. 1347-1354], giving $R_e < (\hbar c)/E = 2 \times 10^{-20}$ m. The bound set by our experiment is surprisingly close to the limits set by LEP given that our measurement is done on a single trapped electron at 100 mK.

1.5 CPT Symmetry

There are three types of discreet symmetries in physics, parity (inversion of all three spatial coordinates, $\vec{r} \rightarrow -\vec{r}$), charge conjugation (converting particles to antiparticles, flipping the sign of all internal quantum numbers), and time reversal

(taking $t \to -t$). For a long time, physics was thought to be invariant under each of these three types of symmetries. In 1957, it was demonstrated in the famous cobalt-60 decay experiment [32] that parity is not conserved in weak force interactions. Parity is conserved in electromagnetic and strong force interactions. Like parity, charge conjugation is conserved in electromagnetic and strong force interactions and violated in weak force interactions. One might suppose that you can simply combine P and C to get a valid symmetry, CP, and for some time after the discovery of P-violation, this was held to be a valid symmetry. In 1964, it was discovered that the K_2^0 meson, which normally decays into 3 pions (preserving CP), can also decay into 2 pions, violating CP, with a 0.2% probability [33]. Additional evidence of CP violation was found in the decay of neutral K mesons [34, 35] and neutral B mesons [36, 37] in the 1990s and later. In the past two years, experiments at the Large Hadron Collider have also seen evidence of CP violation in the decay of D mesons [38] and B_s mesons [39].

The final symmetry, T, is more difficult to measure. In practice, tests of T invariance involve measurements of quantities that should be zero if T is a good symmetry, such as the electron electric dipole moment, where the standard model prediction is that $|d_e| < 10^{-38}\, e \cdot \text{cm}$. A non-zero electron electric dipole moment would imply T violation. The current limit is $|d_e| < 10.5 \times 10^{-28}\, e \cdot \text{cm}$ [40]. To date, no direct evidence of T violation has ever been observed in any experiment.

The CPT theorem underlies current theories including QED and the Standard Model, with the exception of gravity. The CPT theorem states that for any quantum field theory which is Lorentz invariant, which obeys the laws of quantum mechanics, and where interactions are represented by fields, the combined operations of charge

conjugation, parity, and time reversal (in any order) must be an exact symmetry for any interaction [41]. This has several consequences, one of which is that since we observe CP violation, there must also be T violation, if the CPT theorem holds. Additionally, every particle must have the same mass and lifetime as its antiparticle, and every particle and antiparticle must have the same magnitude but opposite sign of magnetic moment. It is this latter consequence that is most easily tested in our experiments with a single electron and single positron.

1.5.1 Tests of CPT Symmetry

Experimental tests of CPT symmetry involve tests of the CPT theorem, namely comparisons of the charge, mass, lifetime, or magnetic moment of a particle and its antiparticle. Because it is not known where a violation of CPT symmetry is likely to show up, it is important to perform tests of CPT in a variety of systems and experiments. Some of the best tests so far are listed below and in Fig. 1.5.

The tightest bound on CPT violation measured so far in any system comes from a comparison of the masses of a neutral kaon and anti-kaon [44] and [42, p. 95], which is

$$r_K \equiv |(m_K - m_{\bar{K}})/m_K| \lesssim 6 \times 10^{-19}. \tag{1.26}$$

The best limit on CPT violation in lepton systems comes from the 1987 UW measurements of the electron and positron g-values [11],

$$r_g \equiv |(g_- - g_+)/g_{av}| \lesssim 2.1 \times 10^{-12}. \tag{1.27}$$

When we measure the positron g-value at or better than the 0.28 ppt precision with

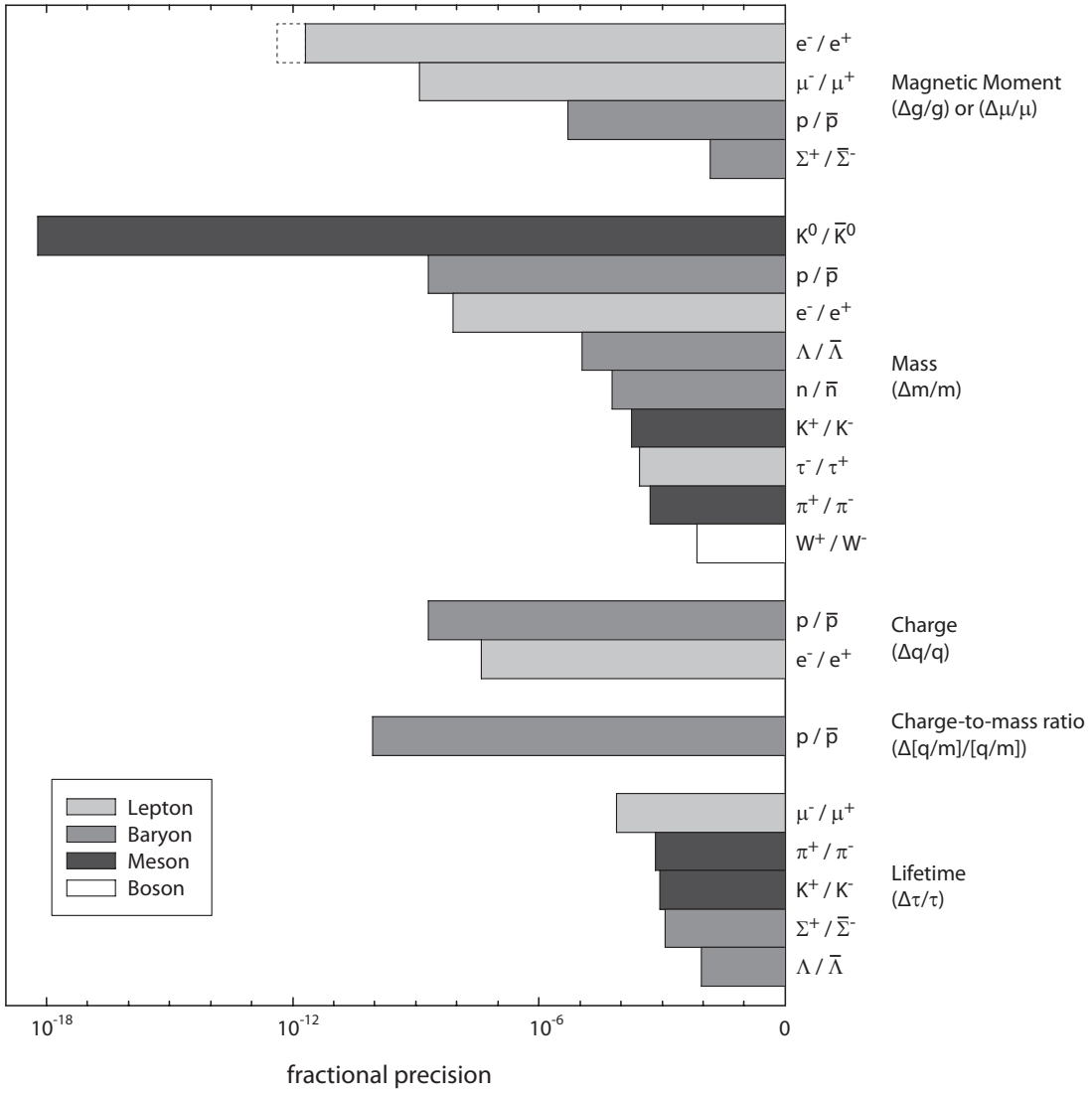

Figure 1.5: Comparison of CPT tests in different systems. All data are from tables compiled by the Particle Data Group [42, pp.100-101] except for the proton/antiproton magnetic moment test which comes from [43]. The dashed line for the e^-/e^+ $\Delta g/g$ indicates the anticpated precision of our upcoming measurement.

which we measured the electron g-value [1], we will improve this limit to better than $r_g < 2 \times 10^{-13}$.

The current best limit on CPT violation in a baryon system comes from a measurement by our group of the proton-antiproton charge-to-mass ratio [45]:

$$r^p_{q/m} \equiv |[(q_p/m_p) - (q_{\bar{p}}/m_{\bar{p}})]/(q/m)_{av}| \lesssim 9 \times 10^{-11}. \tag{1.28}$$

Recent measurements of the magnetic moment of the proton[46] and anti-proton[43] provide an additional limit on CPT violation in baryon systems. Improvements in these measurements, which are in progress [47], could set a much tighter bound on CPT violation in baryon systems.

1.6 Standard Model Extensions

When considering possible violations of CPT symmetry in nature, it can be useful to write down a theoretical framework to describe these possible sources of CPT violation. One such framework includes a generalized CPT- and Lorentz-violating extension to the Standard Model [48]. Within this standard model extension (SME), possible CPT or Lorentz violations are given by parameters which can be explored through experiment. Additionally, it is meant to allow easier comparison between CPT violation bounds set in different systems by different types of experimental measurements. These extensions can be written as a modification to the Dirac equation,

such as

$$\Big(\imath\gamma^\mu\partial_\mu - eA_\mu\gamma^\mu - a_\mu\gamma^\mu - b_\mu\gamma_5\gamma^\mu - \frac{1}{2}H_{\mu\nu}\sigma^{\mu\nu} + \imath c_{\mu\nu}\gamma^\mu\partial^\nu - eA^\nu c_{\mu\nu}\gamma^\mu + \imath d_{\mu\nu}\gamma_5\gamma^\mu\partial^\nu - qA^\nu d_{\mu\nu}\gamma_5\gamma^\mu - m\Big)\psi = 0 \quad (1.29)$$

where a_μ and b_μ are CPT- and Lorentz-violating terms and $H_{\mu\nu}$, $c_{\mu\nu}$, and $d_{\mu\nu}$ preserve CPT but violate Lorentz invariance [48, 49, 50]. Many more terms are included in the full SME, but we will ignore the remainder as they are not relevant to our g-value measurements. The a_μ and b_μ terms serve to modify the electron eigen-energies. The a_μ term redefines the zero of the energy and momentum and so is not directly observable as we only measure the splitting between energy levels. The b_μ term adjusts the relative energy level spacings and thus can be observed in our measurements. Within this framework, a figure of merit for CPT violation in the electron/positron magnetic moment comparison is defined to be the ratio of a CPT-violating electron/positron energy-level difference to the basic energy scale:

$$r_e \equiv \left|\left(E^-_{n,s} - E^+_{n,-s}\right)/E^-_{n,s}\right|. \quad (1.30)$$

This ratio can be rewritten in terms of the difference in measured anomaly frequencies:

$$r_e = \left|\hbar\left(\omega_a^- - \omega_a^+\right)\right|/2mc^2. \quad (1.31)$$

In the proposed framework, this difference in anomaly frequency between the electron and positron is proportional to the component of b that lies along the magnetic field axis:

$$\left(\omega_a^- - \omega_a^+\right) = -4\vec{b}\cdot\hat{B} = -4b_3. \quad (1.32)$$

This implies that the anomaly frequency splitting varies with sidereal time, and that by taking data over the full range of sidereal time, one can set better constraints on CPT violation. Finally, we can rewrite the figure of merit in terms of the CPT violating b_3 term as [49, 50]

$$r_e \equiv \left|\hbar\left(\omega_a^- - \omega_a^+\right)\right| / 2mc^2 = \left|2\hbar b_3\right| / mc^2. \tag{1.33}$$

In this framework, the University of Washington measurements of the electron and positron anomaly frequencies set a limit of $r_e \lesssim 12 \times 10^{-22}$, although their experiment only had data from a very limited range of sidereal time and thus they were only able to set a limit of $b \lesssim 50$ rad/sec [11, 51]. For comparison, if their measurement had been taken when b was perfectly aligned with the magnetic field, they could have set a limit of $b \lesssim 0.7$ rad/sec. By measuring the positron g-value at a precision equal to or greater than the 0.28 ppt precision of our electron g-value measurement we can improve on this r_e limit. If we are careful to take data over a larger range of sidereal time we could also greatly improve the limit on the CPT-violating b term.

1.7 Positrons in a High-Stability Apparatus

A central objective of this thesis was to develop a positron loading scheme using an extremely small positron source that would be compatible with our high precision environment. Such a loading scheme, requiring a new apparatus, will allow for an improved measurement of the positron g-value, using the techniques developed in our recent electron g-value measurement [1, 2]. This will enable a more precise test of CPT violation in lepton systems. The new apparatus, along with some new techniques

such as cavity-assisted axial sideband cooling, should also allow an improvement in the measurement of the electron g-value and an improved determination of the fine structure constant.

This thesis describes the development and characterization of this positron loading scheme and the apparatus and quantum methods required for future g-value measurements. The use of Penning traps for g-value measurements is summarized (chapter 2). The design and construction of the new cryogenic apparatus, including improvements over the previous apparatus (chapter 3) and the development of the small-source positron loading scheme (chapter 4) are described in detail. Trapping electrons in the precision trap and exciting the various resonances that are used in the g-value measurement is the focus of chapter 5. Chapter 6 describes the successful loading of positrons and electrons from our 6.5 μCi ^{22}Na positron source at a rate of 1-2 e^+/min. The characterization of the loading mechanism is also presented. These results clear the way for an improved measurement of the positron g-value, and some steps forward and possible future directions are mentioned (chapter 7), followed by a conclusion (chapter 8) summarizing the work.

Chapter 2

Measuring the g-Value in a Penning Trap

The heart of our apparatus and the heart of our measurement of the electron (and soon, positron) g-value is the Penning trap. This chapter gives an overview of the features of a Penning trap, particularly as they relate to our experiment. The parameters that go into the design of different types of Penning traps will be discussed, focusing on the two different traps used in our apparatus. An introduction to the g-value measurement will be given.

2.1 The Penning Trap

A Penning trap consists of a combination of static magnetic and static electric fields used to confine charged particles. In our Penning trap, a large, uniform magnetic field, $B\hat{\mathbf{z}}$, created by a superconducting solenoid, fixes the cyclotron motion of a

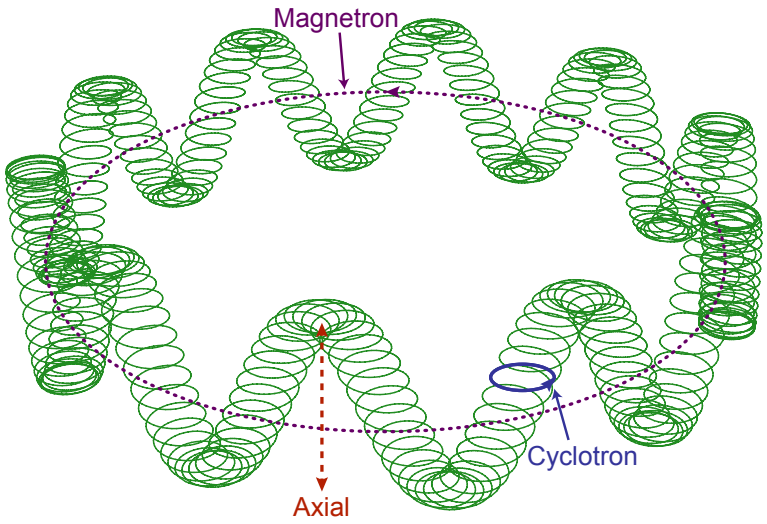

Figure 2.1: Cartoon of an electron orbit in a Penning trap. The relative amplitudes and frequencies of the motions are not to scale.

particle or particles to a field line, providing radial confinement. An electrostatic quadrupole potential, $V \sim 2z^2 - \rho^2$, created by the trap electrodes, provides axial confinement. The radial component of the quadrupole potential is anti-trapping. This has two effects: it causes a slight shift to the free-space cyclotron motion of the particle and it introduces a third motion called the magnetron motion. The magnetron motion is intrinsically unstable but, due to its extremely long damping time, it is effectively stable for our purposes, as will be discussed in Section 5.5. Figure 2.1 shows the three Penning trap motions. A dilution refrigerator is used to cool the cyclotron motion to its quantum mechanical ground state.

2.1.1 Electrode Geometry

An ideal Penning trap can be made by placing electrodes along the equipotential lines of an electric quadrupole, and can be defined by a characteristic trap radius

ρ_0 and height z_0. However, a real trap is never a perfect quadrupole - machining tolerances and imperfections, holes and slits for biasing the electrodes and injecting particles and microwaves, and the finite extent of the electrodes all cause the electric potential to deviate from the ideal. The introduction of two additional electrodes between the ring and each endcap, called compensation electrodes, allows for tuning of the potential to better approximate an ideal quadrupole. Such compensated hyperbolic traps were used in early measurements of the g-value at the University of Washington [52] and similar traps are still commonly used in precision mass spectrometry experiments (see, e.g. [53, 22, 54, 55]). These traps can provide a very good approximation to a perfect quadruploe potential with a large harmonic region.

For some experiments it is desirable to have trap electrodes that have some shape other than hyperbolic. For example, a cylindrical trap with flat endcaps [56] allows for precise calculation of cavity modes and their effects on charged particles confined within the trap. This feature was crucial to the increased precision of our recent electron g-value measurements [12, 1, 2]. Alternatively, cylindrical traps with endcaps which are long, open cylinders allow better access into the trap [57]. This is important for loading positrons at a reasonable rate as discussed in Chapter 4 or for loading antiprotons and positrons for antihydrogen studes such as those done by ATRAP (e.g. [58, 59, 60]) or for measurements on a single proton or antiproton [61, 62, 46, 43]. A planar Penning trap, with electrodes all in one plane, could provide a scalable architecture that may prove useful for quantum computation [63, 64]. Such a trap has been constructed, with electrons loaded and tuning demonstrated [65]. In our experiment, we utilize two of these four different trap configurations, a closed-endcap

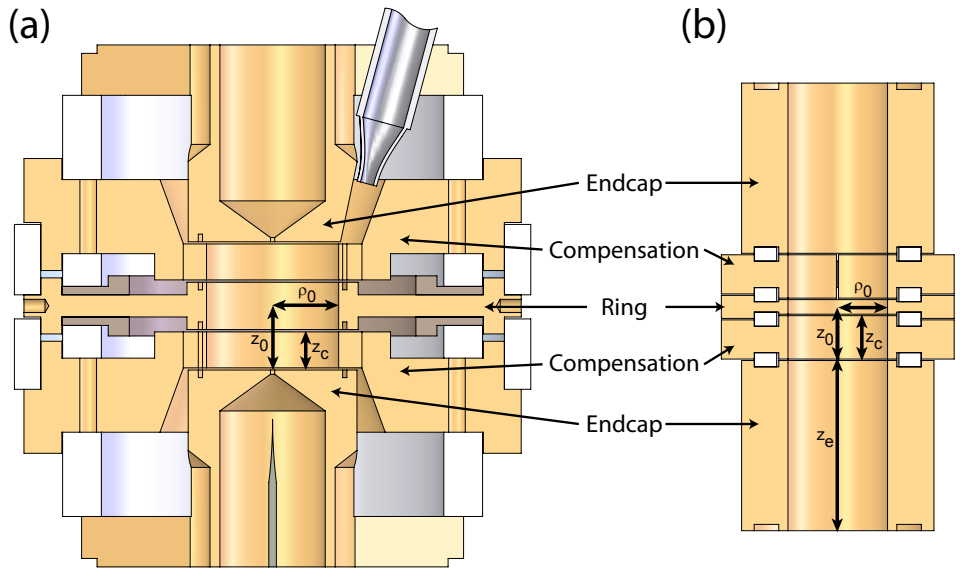

Figure 2.2: Precision trap electrodes (a) and loading trap electrodes (b) with electrodes and trap dimensions labeled for each.

trap for the precision measurement of a single particle g-value and an open endcap trap for positron loading and accumulation. These two traps can be seen in Fig. 2.2. While not related to our experiment, the planar Penning trap mentioned above is also installed inside our apparatus at the bottom of the trap can, below the precision and loading traps.

Regardless of the Penning trap geometry used, careful consideration must go into the choice of dimensions in order to make an optimal trap. In general, the axial frequency of a particle in a compensated Penning trap depends on both the trapping voltage as well as the voltage applied to the compensation electrodes. However, careful choice of trap dimensions can eliminate the dependence of the axial frequency on the compensation voltage. Such a trap is said to be "orthogonalized". An orthogonalized trap allows the compensation voltage to be tuned to minimize the leading order anharmonicities in the trap without changing the axial frequency. Hyperbolic

Table 2.1: Trap dimensions and coefficients.

Precision Trap				Loading Trap			
ρ_0	0.3965 cm	$C_2^{(0)}$	0.077	ρ_0	0.2989 cm	$\bar{C}_2^{(0)}$	0.565
z_0	0.3879 cm	D_2	-3.73 $\times 10^{-4}$	z_0	0.3179 cm	$\bar{D}_2$	0.0987[1]
z_c	0.2385 cm	$C_4^{(0)}$	-0.207	z_c	0.2695 cm	$\bar{C}_4^{(0)}$	-0.260
		D_4	-0.674	z_e	1.0306 cm	$\bar{D}_4$	-0.719
V_R	96.98 V	$C_6^{(0)}$	0.060	V_R	-8.537 V	$\bar{C}_6^{(0)}$	0.245
V_{comp}	79.19 V	D_6	0.326	V_{comp}	-7.567 V	$\bar{D}_6$	0.584

[66], closed-endcap cylindrical [56], and open-endcap cylindrical traps [57] can all be orthogonalized and planar traps can also be optimized to minimize the dependence of the axial frequency on the applied voltages [63, 65].

The details of orthogonalizing and tuning a trap are covered in a number of locations including [67, 56, 57, 68]. The basics are discussed here as they relate to the design of both traps.

2.1.2 Designing the Precision Trap

Our precision trap approximates a closed cylinder and typically has potentials of V_R on the ring electrode and V_{comp} on the compensation electrodes with the endcaps grounded[2]. Typical values of V_R and V_{comp} are given in Table 2.1. Near the center of

[1] A mistake was made in constructing the compensation electrodes for the loading trap. The result is that the trap is not very well orthogonalized. Replacement compensation electrodes with the correct height, $z_c = 0.2782$ cm — yielding $D_2 = 2.20 \times 10^{-4}$ — were designed but never completed.

[2] Penning trap literature often refers to a voltage of $-V_0/2$ on the ring, $V_0/2$ on the endcaps and V_c on the compensation electrodes. The relation between these is given by $V_0 = -V_R$ and $V_c = V_{\text{comp}} - V_R/2$

the trap, at position (r, θ, ϕ) in spherical coordinates with $r \ll d$, the potential can be written as

$$V(\vec{r}) = \frac{-V_R}{2d^2}\left(z^2 - \rho^2/2\right) - \frac{V_R}{2}\sum_{\substack{k=2\\even}}^{\infty} C_k \left(\frac{r}{d}\right)^k P_k(\cos\theta) \tag{2.1}$$

where $P_k(\cos\theta)$ are the Legendre polynomials and d is a characteristic trap dimension defined by

$$d^2 = \frac{1}{2}\left(z_0^2 + \rho_0^2/2\right), \tag{2.2}$$

where the trap radius ρ_0 and height z_0 are defined in Figure 2.2 for both traps used in this experiment. Note that the expansion uses both cylindrical (ρ) and spherical (r) radii. The expansion coefficient C_k is given by

$$C_k = C_k^{(0)} + D_k\left(\frac{1}{2} - \frac{V_{\text{comp}}}{V_R}\right). \tag{2.3}$$

The coefficients can be found from standard boundary-value techniques (see, e.g. [69, ch. 3]) and can be expressed as [56]

$$C_k^{(0)} = -\delta_{k2} + \frac{(-1)^{k/2}}{k!}\frac{\pi^{k-1}}{2^{k-3}}\left(\frac{d}{z_0}\right)^k \sum_{n=0}^{\infty} \frac{(-1)^{n+1}(2n+1)^{k-1}\cos^2[\frac{1}{2}(n+\frac{1}{2})\pi z_c/z_0]}{J_0[\imath(n+\frac{1}{2})\pi\rho_0/z_0]} \tag{2.4}$$

and

$$D_k = \frac{(-1)^{k/2}}{k!}\frac{\pi^{k-1}}{2^{k-3}}\left(\frac{d}{z_0}\right)^k \sum_{n=0}^{\infty} \frac{(-1)^{n}(2n+1)^{k-1}2\sin^2[\frac{1}{2}(n+\frac{1}{2})\pi z_c/z_0]}{J_0[\imath(n+\frac{1}{2})\pi\rho_0/z_0]}, \tag{2.5}$$

where $J_m(x)$ is a Bessel function of the first kind. The C_2 coefficient sets the axial frequency which is given by

$$\omega_z = \sqrt{\frac{-qV_R}{md^2}\left(1 + C_2\right)} \tag{2.6}$$

for a particle of charge q and mass m where d is the characteristic trap dimension defined above. The trap is orthogonalized by choosing the trap dimensions, z_0, ρ_0 and z_c such that D_2 is zero, thus eliminating the dependence of ω_z on V_{comp}.

The higher order C_k terms serve to quantify the trap anharmonicities, and near the trap center ($r \ll d$), only the first few terms are important. For a particle with well-cooled magnetron motion we can take $\rho \approx 0$. Then the first few higher-order terms contribute an amplitude-dependent shift to the axial frequency which can be written as [56]

$$\frac{\Delta\omega_z}{\omega_z} = \frac{3}{2}\frac{C_4}{1+C_2}\frac{E_z}{m\omega_z^2 d^2} + \frac{15}{4}\frac{C_6}{1+C_2}\left(\frac{E_z}{m\omega_z^2 d^2}\right)^2. \tag{2.7}$$

where E_z is the energy of the axial motion with amplitude A, given by $E_z = \frac{1}{2}m\omega_z^2 A^2$. With trap dimensions chosen such that D_2 is zero it is then possible to make C_4 zero by tuning the compensation voltage such that

$$\frac{V_{\text{comp}}}{V_R} = \frac{C_4^{(0)}}{D_4} + \frac{1}{2}. \tag{2.8}$$

This minimizes the amplitude dependent shift to the axial frequency.

Cavity Modes

Our closed-endcap cylindrical trap has a second design criterion that must be accounted for — the relative frequencies of the cavity modes needed for g-value measurements. The closed-endcap precision trap serves as a microwave cavity with resonance modes near the cyclotron frequency. This has two important effects for our measurement. First, the cavity serves to inhibit spontaneous emission of the cyclotron motion when the cyclotron frequency is far away from the relevant cavity modes. This

is very beneficial as it allows enough time to perform the measurement. Second, the cavity modes also interact with the cyclotron frequency, forming a coupled-oscillator system, and thus shifting the cyclotron frequency. With the hyperbolic electrodes that were used in earlier versions of the g-value measurement [11], calculating the structure of the cavity modes and their interaction with a particle in the trap was difficult. Cylindrical Penning traps were invented [56] so that the cavity mode locations could be calculated analytically and their effects accounted for. Since the cavity modes have a non-negligible effect on the cyclotron frequency and thus the g-value, this ability is of great importance. Properly accounting for this effect was one of the major improvements between the 1987 UW measurement [11] and the 2006 and 2008 Harvard measurements [12, 1, 2].

An ideal right circular cylindrical cavity has resonant TM and TE modes (see, e.g. [69]) with frequencies given by

$$\omega_{mnp}^{\mathrm{TM}} = \frac{1}{\sqrt{\mu\epsilon}}\sqrt{\frac{x_{mn}^2}{\rho_0^2} + \frac{p^2\pi^2}{(2z_0)^2}} \tag{2.9}$$

for TM modes where x_{mn} is the nth root of the Bessel function equation $J_m = 0$ and the integers m, n, and p take the values $m = 0, 1, 2, ...$, $n = 1, 2, 3, ...$, and $p = 0, 1, 2, ...$ and

$$\omega_{mnp}^{\mathrm{TE}} = \frac{1}{\sqrt{\mu\epsilon}}\sqrt{\frac{x_{mn}'^2}{\rho_0^2} + \frac{p^2\pi^2}{(2z_0)^2}} \tag{2.10}$$

for TE modes where x'_{mn} is the nth root of the derivative of the Bessel function, $J'_m = 0$ and the integers m, n, and p take the values $m = 0, 1, 2, ...$, $n = 1, 2, 3, ...$, and $p = 1, 2, 3, ...$ In the closed-endcap Penning trap, these modes are modified and shifted slightly due to gaps and splits in the walls of the electrodes.

For the g-value measurement, with a single particle centered in the trap, two types

of modes are the most important. Modes with a non-zero transverse electric field at the trap center, i.e. $\mathrm{TE}_{1n(\mathrm{odd})}$ and $\mathrm{TM}_{1n(\mathrm{odd})}$, couple to the cyclotron motion of a single particle, causing a frequency shift that must be accounted for in the measurement. This frequency shift is discussed in detail in [2] and [70, ch. 5]. Far from these modes, the cyclotron state lifetime is increased due to inhibition of spontaneous emission. As will be mentioned below, the free-space lifetime for our typical cyclotron frequencies is $\gamma_c^{-1} \approx 90\,\mathrm{ms}$. When the cyclotron frequency is tuned far from the cyclotron coupling modes, the inhibited spontaneous emission due to the cavity can produce cyclotron lifetimes of order 10 s. For the trap design used in the 2006 and 2008 measurements, the only consideration was finding a geometry that gave widely-spaced cyclotron coupling modes with no other modes in between.

The second type of modes that are important for a g-value measurement are those with a $z\hat{\rho}$ or $\rho\hat{z}$ gradient in the electric field at the trap center. These modes, which are $\mathrm{TE}_{1n(\mathrm{even})}$ and $\mathrm{TM}_{1n(\mathrm{even})}$, can be used to couple the cyclotron and axial motions for cavity-assisted axial sideband cooling which will be discussed in Section 7.2.1.

Given the geometry of our trap, we can calculate the ideal frequencies of these cavity modes. This calculation was done in order to choose the trap dimensions for the new precision trap. We wish to perform a measurement far from the cyclotron coupling modes but with several cooling modes available. As shown in Figure 2.3, the previous generation trap, used in the 2006 and 2008 measurements, was well designed for performing a g-value measurement, with two widely-spaced cyclotron coupling modes, but was not designed to implement cavity-assisted axial sideband cooling, and the only accessible cooling modes were very near cyclotron coupling

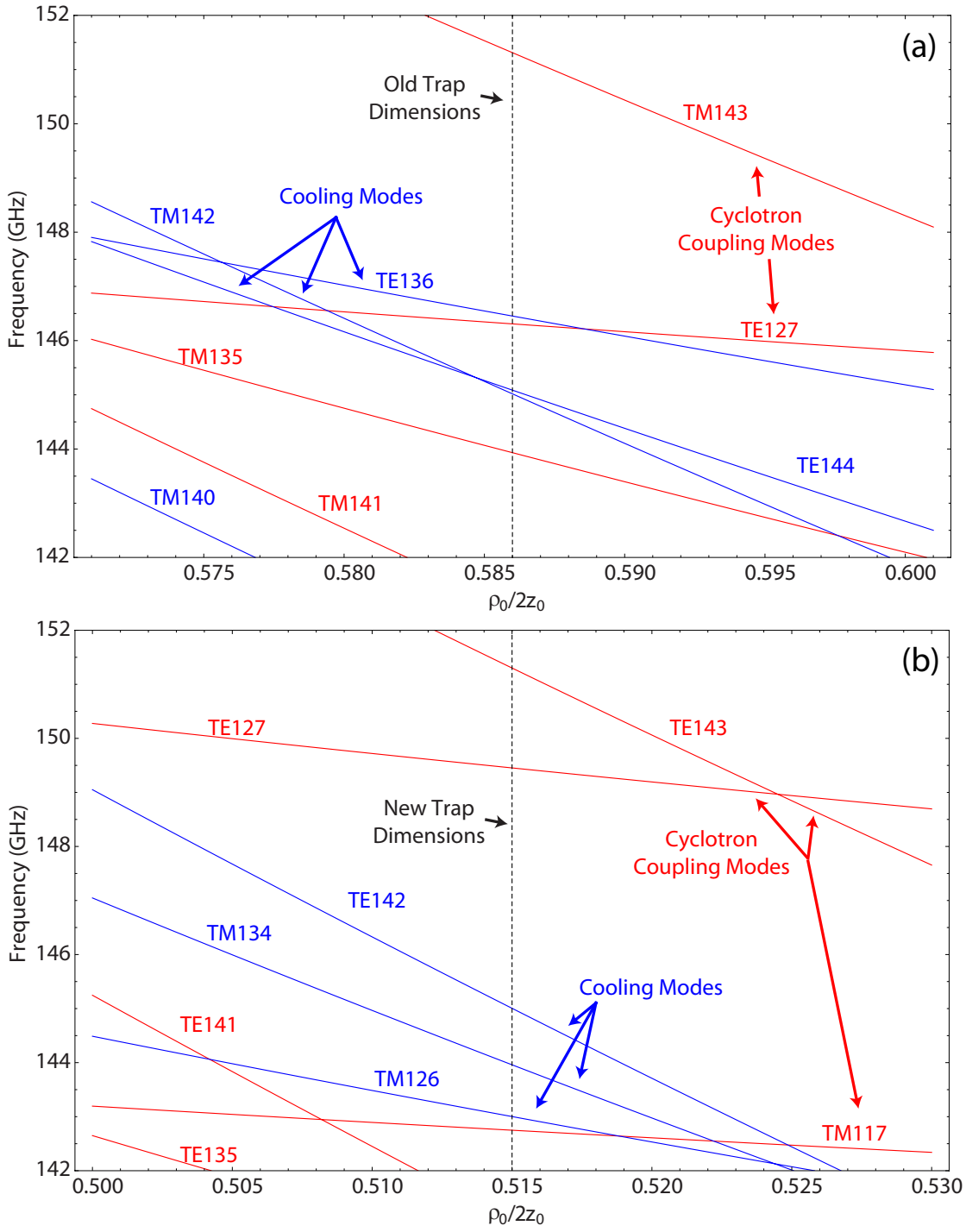

Figure 2.3: A comparison of the approximate cavity mode locations for different ratios of trap radius ρ_0 to height $2z_0$. The modes in the trap used in the 2008 measurement are shown in (a) and those in the new precision trap are shown in (b).

modes. The new trap was designed with slightly modified dimensions to provide two widely spaced cyclotron coupling modes with several cooling modes between them. The overall trap height, z_0, was kept constant, while the trap radius to height ratio, ρ_0/z_0, was chosen to change the locations of the cavity modes. Calculating the ideal cavity mode frequencies is also used to identify the modes when performing cavity mode maps, which will be discussed in Section 7.1.2.

Thermal Contraction

The thermal contraction of the silver electrodes is significant from 300 K to 100 mK and must be accounted for. The electrode dimensions that orthogonalize the trap and give the appropriate cavity mode structure are computed and those dimensions are then taken to be the cold dimensions. The thermal expansion is calculated for the electrodes and spacers (typically using available data from 300 K to 4 K — the additional change between 4 K and 100 mK is negligible) to solve for the room temperature geometry neccessary to yield the appropriate cold dimensions. Additionally, the electrode and spacer geometry is designed to take advantage of the relative thermal contraction between the silver electrodes and the fused quartz spacers such that the electrodes contract onto the spacers to fix the trap stack tightly together as everything cools. This is also the case for the loading trap discussed below.

2.1.3 Designing the Loading Trap

The loading trap approximates an open-ended cylinder [57]. As in the precision trap, we typically apply potentials of V_R on the ring and V_{comp} on the compensation

electrodes with the endcaps grounded. Typical values are shown in Table 2.1. Note that the values of V_R and V_{comp} differ between the two traps.

Again, near the center of the trap the potential can be written as

$$V(\vec{r}) = -\frac{V_R}{2}\sum_{\substack{k=2\\even}}^{\infty}\bar{C}_k\left(\frac{r}{d}\right)^k P_k(\cos\theta) \tag{2.11}$$

where $P_k(\cos\theta)$ are the Legendre polynomials. The expansion coefficient $\bar{C}_k$ is given by

$$\bar{C}_k = \bar{C}_k^{(0)} + \bar{D}_k\left(\frac{1}{2} - \frac{V_{\text{comp}}}{V_R}\right) \tag{2.12}$$

where the bar is used to indicate that the expansion coefficients for an open-endcap trap are different than those for a closed-endcap trap. For the open-endcap trap, the coefficients are given by [57]

$$\bar{C}_k^{(0)} = \frac{(-1)^{k/2}}{k!}\frac{\pi^{k-1}}{2^{k-3}}\left(\frac{d}{z_0+z_e}\right)^k\sum_{n=0}^{\infty}(2n+1)^{k-1}\frac{A_n^{(c)}}{J_0[\imath(n+\frac{1}{2})\pi\rho_0/(z_0+z_e)]} \tag{2.13}$$

and

$$\bar{D}_k = \frac{(-1)^{k/2}}{k!}\frac{\pi^{k-1}}{2^{k-3}}\left(\frac{d}{z_0+z_e}\right)^k\sum_{n=0}^{\infty}(2n+1)^{k-1}\frac{A_n^{(d)}}{J_0[\imath(n+\frac{1}{2})\pi\rho_0/(z_0+z_e)]} \tag{2.14}$$

where

$$A_n^{(c)} = \frac{1}{2}\left((-1)^n - \sin\left[\frac{(n+\frac{1}{2})\pi z_0}{z_0+z_e}\right] - \sin\left[\frac{(n+\frac{1}{2})\pi(z_0-z_c)}{z_0+z_e}\right]\right) \tag{2.15}$$

and

$$A_n^{(d)} = \sin\left[\frac{(n+\frac{1}{2})\pi z_0}{z_0+z_e}\right] - \sin\left[\frac{(n+\frac{1}{2})\pi(z_0-z_c)}{z_0+z_e}\right] \tag{2.16}$$

As in the precision trap, the first coefficient, $\bar{C}_2$ sets the axial frequency, which in the loading trap is given by

$$\omega_z = \sqrt{\frac{-qV_R}{md^2}\left(\bar{C}_2\right)} \tag{2.17}$$

where d is the characteristic trap dimension defined above. The trap can be orthogonalized by the appropriate choice of ρ_0 and z_0 to yield $\bar{D}_2 = 0$.

Again, the higher-order $\bar{C}_k$ quantify the anharmonicities of the trap, with only the first few being important near the trap center. As in the precision trap, the compensation voltage can be adjusted to give $\bar{C}_4 \approx 0$. Furthermore, for an open-endcap trap, which can be orthogonalized for any compensation electrode height, one can choose the height of the compensation electrodes, z_c, to yield $\bar{C}_6 = 0$. Then tuning V_{comp} to make $\bar{C}_4$ zero also tunes out $\bar{C}_6$.

2.1.4 Trap Motions and Frequencies

We have already discussed the axial frequency of a charged particle in a Penning trap. The expression for the axial frequency in the precision trap can be seen in Eq. 2.6 and the expression in the loading trap is given in Eq. 2.17. We turn now to a discussion of the other Penning trap motions.

A charged particle in free space in a spatially uniform magnetic field will undergo cyclotron motion about the magnetic field lines with a frequency given by

$$\nu_c = \frac{eB}{2\pi m}. \tag{2.18}$$

Additionally, for a spin-1/2 particle, the spin frequency is given by

$$\nu_s = \frac{g}{2}\nu_c. \tag{2.19}$$

where g is the particle's g-value.

As can be seen from Eq. 2.19, the g-value of a particle can be determined from a measurement of the cyclotron and spin frequencies. For an electron or positron

where g is very nearly equal to 2, the spin frequency and cyclotron frequency differ by approximately one part in 10^3. In this case, the measurement uncertainty is reduced by measuring the cyclotron frequency and the difference between the spin and cyclotron frequencies (the so-called anomaly frequency). In other words,

$$\frac{g}{2} = \frac{\nu_s}{\nu_c} = 1 + \frac{\nu_s - \nu_c}{\nu_c} = 1 + \frac{\nu_a}{\nu_c} \tag{2.20}$$

where ν_a is the anomaly frequency.

The presence of the electrostatic quadrupole modifies the cyclotron frequency, yielding, for an ideal trap,

$$\omega_\pm = \frac{1}{2}\left[\omega_c \pm (\omega_c^2 - 2\omega_z^2)^{1/2}\right] \tag{2.21}$$

(see [67, Sec.II]) where $\omega_+ + \omega_- = \omega_c$, the free-space cyclotron frequency. We define the trap-modified cyclotron frequency to be

$$\omega_c' \equiv \omega_+ = \omega_c - \omega_m \tag{2.22}$$

where ω_m is the magnetron frequency, defined to be

$$\omega_m \equiv \omega_- = \omega_z^2/2\omega_c', \tag{2.23}$$

where these relationships apply only for an ideal Penning trap.

Of the four Penning trap motions for an electron or positron, only the cyclotron motion has an appreciable radiative damping rate. The cyclotron motion decays radiatively via synchrotron radiation with a damping rate in free space given by

$$\gamma_c = \frac{1}{4\pi\epsilon_0}\frac{4e^2\omega_z^2}{3mc^3}. \tag{2.24}$$

For our typical cyclotron frequencies, this gives an excited state lifetime of approximately 90 ms. As discussed in Section 2.1.2, the presence of the microwave cavity modifies the free space damping rate depending on the proximity of the cyclotron frequency to certain cavity modes. When far from the relevant cavity modes, we can observe cyclotron lifetimes of many seconds. We also modify the free space damping rate of the axial motion by coupling to an external circuit as described in Section 5.3 and Section 6.4.1. The frequencies and damping rates for all the motions are given in Table 2.2.

The Brown-Gabrielse Invariance Theorem

A real Penning trap has imperfections due to machining tolerances and misalignments. To leading order these imperfections can be quantified by an elliptical distortion of the trap electrodes and a misalignment of the electrodes with respect to the magnetic field. In this case, the trap eigenfrequencies are given by $\bar{\nu}_z$, $\bar{\nu}_c$, and $\bar{\nu}_m$. But as can be seen from Eq. 2.20, the g-value is defined in terms of the free-space cyclotron frequency. The Brown-Gabrielse invariance theorem states that, for the leading order imperfections mentioned above, the free space cyclotron frequency, ν_c, can be obtained from a measurement of the actual trap eigenfrequencies, regardless of the degree of distortion or misalignment [71],

$$\nu_c = \sqrt{(\bar{\nu}_c)^2 + (\bar{\nu}_z)^2 + (\bar{\nu}_m)^2}. \tag{2.25}$$

For an appropriately ordered hierarchy of frequencies, $\bar{\nu}_c \gg \bar{\nu}_z \gg \bar{\nu}_m \gg \delta$, such as we have for an electron or positron in our Penning trap (see Table 2.2), Eq. 2.25

Table 2.2: Precision trap motions, frequencies and damping rates. The magnetron and spin damping rates are from radiative decay and are negligible in our experiment. The cyclotron damping rate is typical of the cavity-modified rate when far from modes that couple to the cyclotron motion, modified from the 90 ms free-space lifetime. The axial damping rate is from coupling to an external circuit (the radiative damping rate is longer than a day and thus also negligible).

Motion	Frequency	Damping Rate
axial	$\bar{\nu}_z \approx 200\,\mathrm{MHz}$	$\gamma_z^{-1} \approx 0.2\,\mathrm{s}$
cyclotron	$\bar{\nu}_c \approx 150.0\,\mathrm{GHz}$	$\gamma_c^{-1} \approx 5\,\mathrm{s}$
spin	$\nu_s \approx 150.2\,\mathrm{GHz}$	$\gamma_s^{-1} \approx 5\,\mathrm{yr}$
magnetron	$\bar{\nu}_m \approx 133\,\mathrm{kHz}$	$\gamma_m^{-1} \approx 4\,\mathrm{Gyr}$

can be approximated by

$$\nu_c \simeq \bar{\nu}_c + \frac{\bar{\nu}_z^2}{2\bar{\nu}_c}, \tag{2.26}$$

with relative corrections of order $(\bar{\nu}_z/\bar{\nu}_c)^4 \approx 10^{-12}$ times the square of the degree of misalignment or ellipticity ($\approx (10^{-2})^2$) [71]. This eliminates the requirement to measure the magnetron frequency in the g-value measurement at our current level of precision.

Relativistic Corrections and an Expression for the g-Value

The cyclotron frequency also has a small relativistic shift. This relativistic shift is given by

$$\Delta\nu_c = -\delta\,(n + 1 + m_s) \tag{2.27}$$

with

$$\frac{\delta}{\nu_c} = \frac{h\nu_c}{mc^2} \approx 10^{-9} \tag{2.28}$$

which is non-negligible at our experimental precision. The ability to cool the cyclotron motion to its ground state and to perform single quantum transitions means that we can carefully control the relativistic shifts, thus adding no additional error to the measurement. The quantum nature of the measurements was the critical central feature of the 2006 and 2008 measurements, compared to previous measurements of the g-value. By always measuring the cyclotron frequency of the same transition, we can calculate the relativistic effects and account for them with essentially no uncertainty added. We choose to always start any measurement in the spin-up cyclotron ground state for consistency (for an electron — for a positron the spin ladders are flipped and so we start in the spin down cyclotron ground state). Therefore we always measure the spin-up cyclotron transition for an electron and the spin-down cyclotron transition for a positron. That is, we choose to always measure

$$\bar{f}_c = \bar{\nu}_c - 3\delta/2 \tag{2.29}$$

and

$$\bar{\nu}_a = \nu_s - \bar{\nu}_c = \frac{g}{2}\nu_c - \bar{\nu}_c \tag{2.30}$$

as defined in Fig. 2.4.

Taking all of these considerations into account, we can now write down an equation for $g/2$ in terms of the actual measured trap eigenfrequencies,

$$\frac{g}{2} = \frac{\bar{\nu}_c + \bar{\nu}_a}{\nu_c} \simeq 1 + \frac{\bar{\nu}_a - \frac{\bar{\nu}_z^2}{2\bar{f}_c}}{\bar{f}_c + 3\delta/2 + \frac{\bar{\nu}_z^2}{2\bar{f}_c}} + \frac{\Delta\omega_{\mathrm{cav}}}{\omega} \tag{2.31}$$

where $\Delta\omega_{\mathrm{cav}}/\omega$ is the shift due to the interaction of the cyclotron frequency with the modes in the trap cavity as was mentioned earlier.

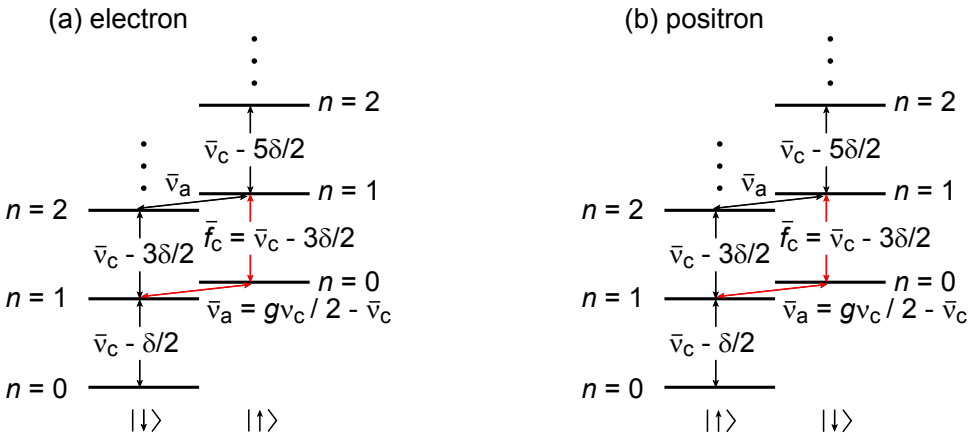

Figure 2.4: The energy levels of an electron (a) and a positron (b) in a Penning trap. The red arrows indicate the transitions that are measured in order to determine the g-value.

2.2 Magnetic Bottle

The magnetic bottle [72], the simplest magnetic field gradient with both axial symmetry about $\hat{z}$ and reflection symmetry under $z \to -z$, provides a way to monitor the cyclotron and spin-flip states of an electron or positron for a g-value measurement. It has been used in every measurement of the electron or positron g-value performed in a Penning trap to date, and, more recently, direct measurements of the proton and anti-proton magnetic moments [46, 43]. The so-called magnetic bottle is a quadratic distortion added to the uniform magnetic field at the center of the trap whose purpose is to couple the cyclotron and spin motions to the axial motion, which is easier to detect. In our case, the magnetic bottle is generated by two small nickel rings placed symmetrically to either side of the trap center as shown in Fig. 2.5. These nickel rings saturate in the 6 T magnetic field with a saturation magnetization of M = 485 emu/cm^3.

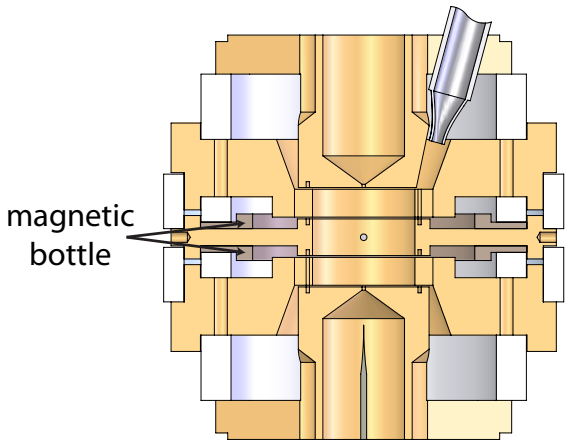

Figure 2.5: Precision trap electrodes with the magnetic bottle labeled

The formula for the magnetic distortion due to magnetic materials placed near the trap (in Gaussian units) is [67, Sec. VI.B.]

$$\Delta\vec{B}(\vec{r}) = \sum_{l=0}^{\infty} B_l r^l \left[P_l(\cos\theta)\hat{z} - (l+1)^{-1} P_l^1(\cos\theta)\,\hat{\rho}\right], \tag{2.32}$$

where $P_l^1(\cos\theta) = \sin\theta\, dP_l(\cos\theta)/d\cos\theta$ is an associated Legendre polynomial. The coefficients B_l are given by

$$B_l = (l+1)(l+2)\,2\pi \int \rho'\, d\rho'\, dz'\, M(\rho', z')(r')^{-l-3} P_{l+2}(\cos\theta'), \tag{2.33}$$

again in Gaussian units. For the magnetic bottle, the sum in Eq. 2.32 is just over even l because the magnetic bottle is symmetric under $z \to -z$. Keeping the first two terms in the sum we get

$$\Delta\vec{B}(\vec{r}) = B_0\hat{z} + B_2\left[\left(z^2 - \rho^2/2\right)\hat{z} - z\rho\hat{\rho}\right] \tag{2.34}$$

where B_0 provides a constant offset to the central field value and B_2 gives the strength of the magnetic bottle coupling. The value of B_2 can be measured by moving an electron (or positron) axially in the trap and measuring the cyclotron frequency at several different points above and below the electrostatic center of the trap.

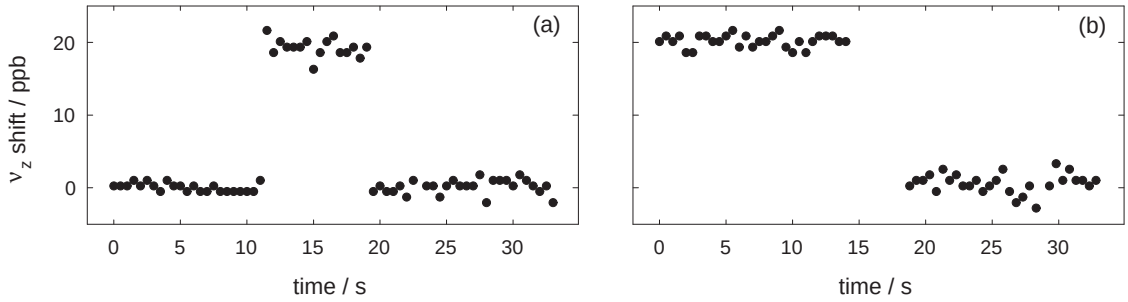

Figure 2.6: The axial frequency shift from a cyclotron jump (a) and a spin flip (b) in the 2008 measurement trap.

The 2008 measurement utilized a magnetic bottle with a B_0 offset of about -0.7% and a B_2 calculated to be $1474(31)\,\mathrm{T/m^2}$ and measured to be $1540(20)\,\mathrm{T/m^2}$ [70]. For our new apparatus, we chose to install a smaller magnetic bottle for reasons discussed below. This new bottle has a B_0 that changes the central field value by about -0.3% and B_2 is calculated to be $658(84)\,\mathrm{T/m^2}$. B_2 has not yet been experimentally measured in this trap, although agreement between the measured and calculated axial frequency shift due to a cyclotron transition indicates that the value of B_2 must be close to the calculated value.

The coupling of the cyclotron and spin states to the axial frequency by the magnetic bottle will be discussed in detail in Section 5.4 but the result is an axial frequency shift that is given by

$$\frac{\Delta\omega_z}{\omega_z} = \frac{2\mu_B B_2(n + \frac{1}{2} + \frac{g}{2}m_s)}{m\omega_{z0}^2}. \tag{2.35}$$

For the 2008 measurement the axial frequency shift for a single cyclotron jump ($\Delta n = 1$) or a spin flip ($\Delta m_s = 1$) was 20 ppb, or 4 Hz. This shift can be seen in Fig. 2.6. For the smaller magnetic bottle used in the current precision trap, the axial frequency shift is 8.5 ppb, or 1.7 Hz. This will be discussed further in Section 5.4.

Although the smaller magnetic bottle chosen for this new apparatus makes it more difficult to resolve the axial frequency shift from a single cyclotron transition or spin flip, the advantages outweigh this minor difficulty. The drawback to using a magnetic bottle to detect the cyclotron and spin states is that it also limits the accuracy of the g-value measurement by broadening the resonance linewidths of the cyclotron, spin, and anomaly transitions. In the same way that the magnetic bottle couples the cyclotron and spin energies to the axial frequency, the bottle also couples the axial energy to the cyclotron and anomaly frequencies.

The expected cyclotron and anomaly lineshapes, covered in detail in [73, 74, 70], are two different limits of the same general lineshape. For this lineshape, one can define a linewidth parameter,

$$\Delta\omega \equiv \omega_0 \frac{B_2}{B}\langle z^2\rangle = \omega_0 \frac{B_2}{B}\frac{kT_z}{m\omega_z^2}, \tag{2.36}$$

where ω_0 can refer to the cyclotron, spin, or anomaly frequency. The width of the cyclotron line is given by $\Delta\omega$ and so is proportional to B_2. Thus a decrease in the magnetic bottle size will result in a similar decrease in the width of the cyclotron line. The width of the anomaly line is given by $\gamma_c + 2\Delta\omega^2/\gamma_z$ which is proportional to $(B_2)^2$. Until the natural linewidth is reached, a decrease in the magnetic bottle size will greatly decrease the width of the anomaly line. Decreasing these lines allows for a more precise determination of the cyclotron and anomaly frequencies which in turn will allow for a more precise determination of the g-value. We chose a 2.3 times smaller magnetic bottle for the new precision trap as a trade-off between narrower resonance lines and decreased transition detection efficiency.

Other potential options to get around this unwanted resonance line broadening

include using a superconducting loop as a variable magnetic bottle [75] or utilizing the relativistic couplings between the motions in place of a bottle [76]. Both of these have been investigated but initial tests with the variable bottle had 10 ppb variation in the magnetic field [77], making this option undesirable unless this variation could be eliminated or greatly reduced. With the advent of the quantum cyclotron, the relativistic bottle is no longer as appealing. The axial frequency shift of a single quantum transition from the relativistic couplings is not currently observable and the other benefits of the quantum cyclotron outweigh other possibilities for detecting the relativistic shifts. The proton magnetic moment experiment, which must use a much larger magnetic bottle, gets around this problem by using two traps, one with a magnetic bottle for detecting the axial frequency shifts and one without a bottle for performing the measurement [62].

Chapter 3

The Cryogenic Apparatus

The Penning trap electrodes (see Fig. 3.1) make up a fairly small portion of the entire experimental apparatus, which includes a dilution refrigerator used to cool the Penning trap electrodes to 100 mK, a 6 tesla superconducting magnet to provide the magnetic field of the Penning trap, and a large nitrogen-cooled liquid helium dewar to cool the magnet and dilution refrigerator to 4 K, along with all the necessary wiring and support structure for these components. An overview of the cryogenic portions of the apparatus and details of each major component will be discussed below.

3.1 Trap Construction

3.1.1 The Trap and Trap Vacuum Enclosure

The Penning trap electrodes are housed in a special ultra-high vacuum (UHV) enclosure, commonly referred to as the "trap can". The trap can itself is inside the inner vacuum chamber (IVC) of the dilution refrigerator (see Section 3.2.3). The trap

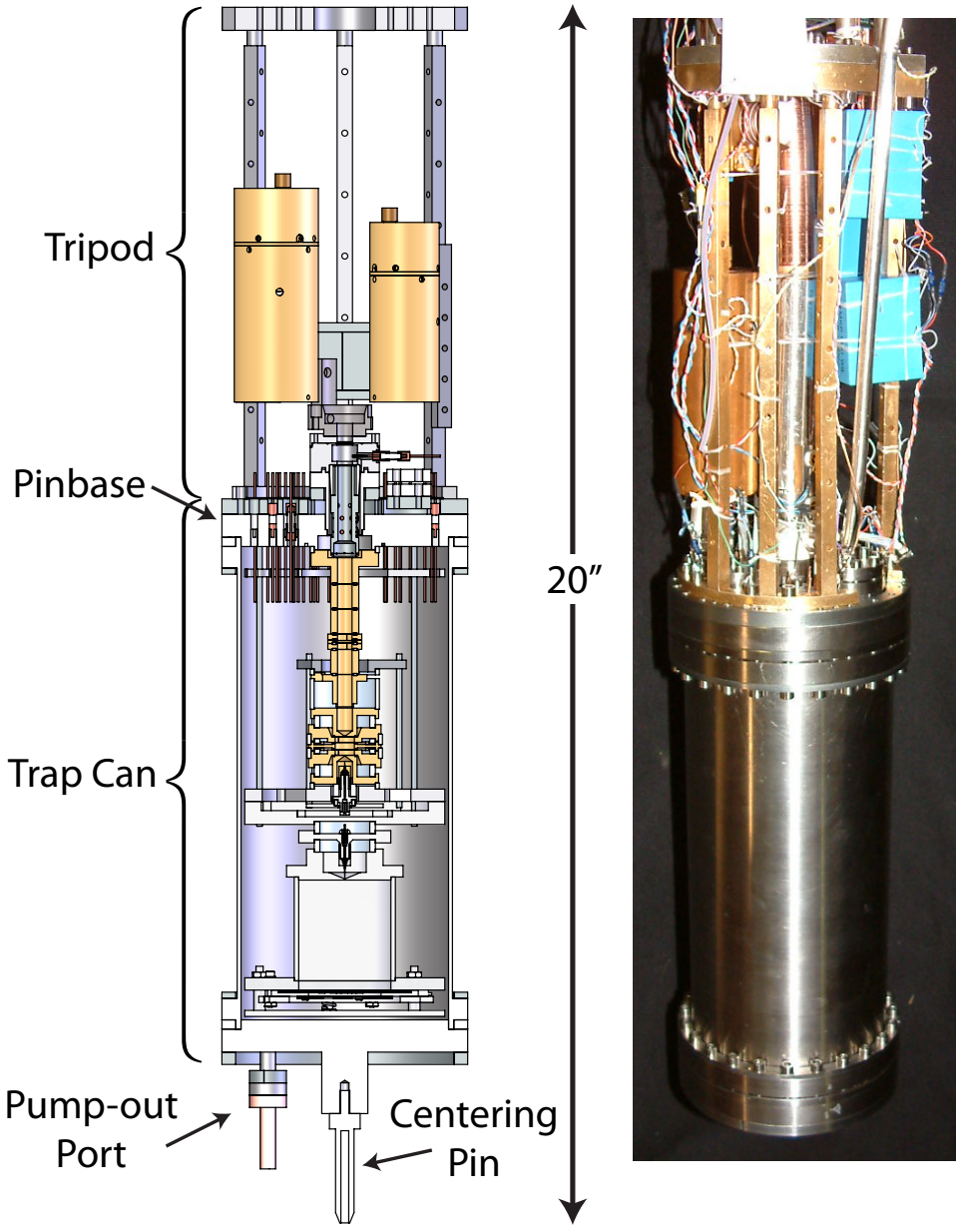

Figure 3.1: Cutaway diagram (left) and photograph (right) of the tripod region and the trap assemblies in the trap can.

can is made out of titanium[1] for reasons discussed below. The top flange of the trap can, known as the "pinbase", contains the electrical feedthroughs and indium-sealed flanges necessary for access into the trap can. The bottom flange of the trap can contains a port for pumping out the trap can and a centering pin that aligns the trap can with respect to the IVC. The top and bottom flanges are sealed to the trap can body with indium seals. The trap can is thermally anchored to the mixing chamber of the dilution refrigerator through two silver tripod regions. The upper silver tripod region, connected to the bottom of the mixing chamber, was provided by Janis (with a few later modifications performed at Harvard) and is known as the silver extension. The posts of the silver extension are bolted to the top and bottom plates, allowing them to be removed if necessary. The lower tripod region was brazed together at Harvard and is known as the tripod (despite having 6 legs) for historic reasons. The tripod connects the trap can to the silver extension. The tripod had a layer of gold electroplated after brazing. The tripod and trap can are shown in Fig. 3.1.

Care is taken to avoid using magnetic materials in the apparatus, especially in close proximity to the trap electrodes. However, previous work found that when operating at dilution refrigerator temperatures in a high-precision experiment, the nuclear paramagnetism of certain materials used in the construction of the experiment was causing a temperature dependent magnetic field shift that was large enough to adversely affect a measurement of the electron g-value [2, 78]. Thus, for those parts of the apparatus that are closest to the magnetic field center, such as the trap electrodes themselves as well as other parts inside the trap can and the trap can itself, materials

[1]Commercially pure (CP) titanium, grade 2. CP titanium is pure, unalloyed titanium. There are 4 grades, each with slightly different levels of impurities and slightly different yield strengths. For our purposes, the 4 grades are equivalent and grade 2 is the most readily available.

must be chosen that have a low nuclear Curie constant in addition to any other properties that might be desired. The list of acceptable materials we used includes silver, titanium, tungsten, molybdenum, fused quartz, and small amounts of OFE copper near the edges of the trap can (such as the feedthrough pins on the pinbase or the planar trap surface near the bottom of the trap can).

Electrode Preparation

The precision trap electrodes are machined from high purity[2] silver. The inner surfaces are carefully polished to a mirror finish after machining. To accomplish the polishing, cylindrical electrodes, such as the ring, are held in a custom teflon sleeve, which is then clamped in a lathe — the teflon deforms just enough under the clamping pressure to hold the electrode securely but not so much that it distorts or damages the electrode. The lathe is spun at full speed and the electrode inner surface is polished by hand using polishing paper mounted on wooden sticks. Typically the electrodes are polished for 5 minutes each using 9 μm, 3 μm, 2 μm, and 1 μm polishing papers[3]. The positron loading trap electrodes (see Section 4.3), all of which are cylindrical, were polished using the same procedure. After polishing, the cylindrical electrodes were cleaned with isopropanol in an ultrasonic bath to remove any remaining dust or debris from polishing.

The flat endcaps of the precision trap require a different method for polishing. They are mounted in a heavy brass block, with a custom pocket machined to hold them, using CrystalBond 509. They are polished by hand on a granite table using

[2] 99.999%, from ESPI Metals
[3] 3M Wetordry 281Q with alumina grit

the same set of polishing papers, followed by a 5 minute polish using a 1 μm diamond slurry on a stiff cloth pad[4], a 30 second polish using a 0.05 μm alumina slurry on a soft cloth pad[5], and a 15 second rinse-polish in a steady stream of DI water on the same soft pad. The surface was then gently cleaned using a q-tip soaked in Alconox and water followed by a DI water rinse. The bulk of the CrystalBond was removed by using q-tips soaked in acetone. The electrode plus holder was then cleaned with acetone in an ultrasonic bath to remove all remaining CrystalBond. Finally, the electrode was removed from the holder and cleaned with isopropanol in an ultrasonic bath.

After polishing, the precision electrodes have silver wire leads brazed in. The brazing is done in a hydrogen environment using a copper-silver braze alloy[6]. Finally, they have a layer of gold thermally evaporated onto the inner surface. Thermal evaporation was chosen for the precision electrodes rather than the usual electroplating because thermal evaporation is thought to be better at minimizing patch potentials and because our lab's proton experiment had good success producing qualitatively better surface finishes using thermal evaporation [62]. For the flat endcap electrodes, the usual thermal evaporation procedure of gold pellets held in a tungsten boat needed only a small modification — a special jig to hold the electrodes rather than the usual wafer. For the other electrodes, the basic procedure developed for the proton experiment was used. This procedure involves electroplating a layer of gold onto a tungsten rod, mounting this rod through the center of the electrodes, and then heating this rod to evaporate the electroplated gold layer onto the inner surface of the electrodes.

[4]PACE Technologies, slurry is PC-1001-250, pad is DC-3008
[5]PACE Technologies, slurry is NA-1005-16, pad is NP-7008
[6]BVAg-8, a 72% Ag, 28% Cu eutectic

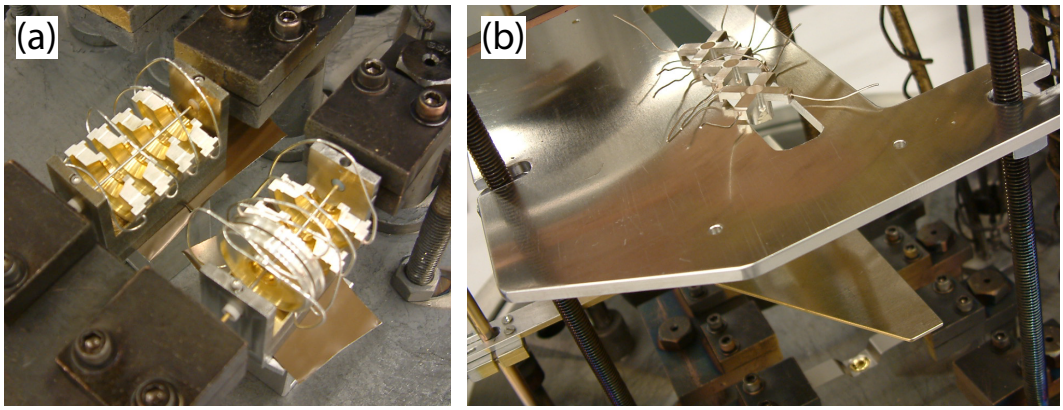

Figure 3.2: Pictures of the thermal evaporation set-up for (a) cylindrical electrodes and (b) the precision endcap electrodes.

A picture of the set-up for both types of electrodes can be seen in Fig. 3.2 and additional details of the procedure can be found in [62, Ch. 3]. The evaporation for all electrodes used a Sharon Thermal Evaporator in the Harvard CNS Cleanroom.

Initial attempts yielded only limited success — the majority of the evaporated gold tended to rub off easily when wiped with isopropanol on a q-tip. While this failure mode did occasionally occur with the copper proton electrodes, the failure rate was much higher with the silver electrodes. Due to concerns that impurities were coating the electrodes and preventing the adhesion of the gold layer, two changes were made. First, we switched from using TG-25 ES gold plating solution, which has added stabilizers that we thought might be affecting the adhesion, back to plain TG-25[7] (used for the proton electrodes) for electroplating gold onto the tungsten rods. Second, we performed a pre-heat of the gold-plated tungsten filament in the evaporator before mounting it with the electrodes. The purpose of this pre-heat was to attempt to boil off any impurities that might come off the rod and coat the electrode surface before the gold itself evaporated and coated the surface. To do this,

[7]Both from Technic, Inc

we put the tungsten filament in the evaporator by itself and applied current to heat it close to but less than the point at which the gold starts to boil off. We then opened the evaporator, installed the pre-heated rod into the electrode jig, and then proceeded with the actual evaporation. We performed both of these changes on the same run and had complete success. It is not known whether both of these steps are necessary for successful evaporation, but the additional time required to perform the reheat is small compared to having to re-do electrodes so it is recommended to take advantage of both.

Pinbase construction

The pinbase is made of titanium and contains 41 electrical vacuum feedthrough pins. These pins from Insulator Seal are composed of an OFHC copper center conductor, a 70-30 copper-nickel alloy[8] cap and outer sheath, and a ceramic (94% alumina) insulator. These pins are first brazed into silver plugs in a hydrogen atmosphere using a copper-silver braze alloy[9]. The silver plugs are then e-beam welded into the titanium pinbase by Joining Technologies. The exact geometry and weld parameters for this silver to titanium e-beam weld are very important to ensure a good, leak-tight weld that is robust to thermal cycling. Our first attempt had the silver plugs flush with or even slightly below the titanium surface to which they were being welded. This produced a pinbase that, while initially leak-tight, opened up a number of small leaks in the silver to titanium e-beam joints upon repeated thermal cycling. A second pinbase, designed so that the silver plugs protruded 0.01" above the titanium surface

[8]non-magnetic

[9]BVAg-8, a 72% Ag, 28% Cu eutectic

where the e-beam weld occurs, has proven to be quite robust. The pinbase also contains 4 titanium flanges — one each for the microwaves, positrons, and the 200 MHz amplifier feedthrough, and one extra. These titanium flanges are also e-beam welded to the titanium pinbase. Titanium to titanium e-beam welding is much simpler than silver to titanium and requires no special design considerations other than the tight fit necessary for e-beam welding in general.

3.2 Apparatus

The largest portion of the experimental apparatus is the commercial dilution refrigerator, superconducting magnet and helium dewar. The entire apparatus is shown in Fig. 3.3.

3.2.1 The Magnet

Magnetic stability is crucial for a sub-ppt measurement of the electron or positron g-value, since any changes in magnetic field correspond directly to changes in the cyclotron (and anomaly) frequencies. The effect of small external fluctuations in the magnetic field is small when compared to the 6 tesla magnetic field of our magnet. External fluctuations are further reduced through the use of a passive, self-shielding coil that forms part of the solenoid system. This shield coil utilizes the principal of flux conservation to cancel fluctuations in the ambient field [79]. In principle, this method of shielding applies to arbitrarily fast external fluctuations, although in practice, high-frequency fluctuations are already well shielded by eddy currents in the aluminum and copper cylinders of the magnet form, dewar, and fridge.

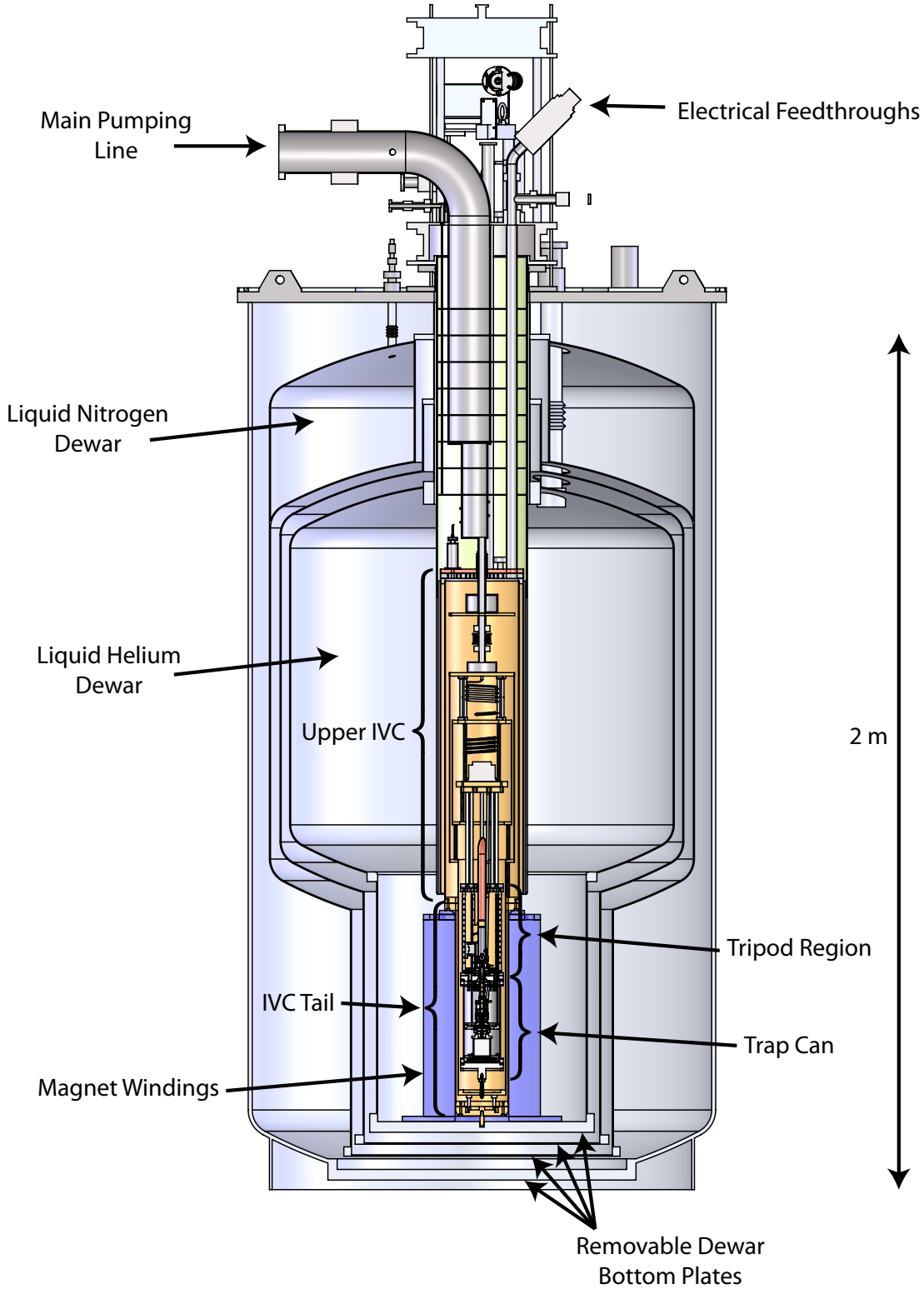

Figure 3.3: A cut-away figure of the entire apparatus

Our superconducting magnet was constructed by Cryomagnetics, Inc. It uses single-filament superconducting wire (a single strand of niobium-titanium encased in copper) for maximum long-term stability. While multi-filament wire is more commonly used in superconducting magnets because it is less susceptible to flux jumping and can be charged and discharged much more rapidly, single-filament wire is preferred for very high-precision systems where maximum stability over long time periods is the most important feature. The inherent difficulty in making a perfect superconduting joint with multi-filament wire leads to lower long-term stability than for single-filament wire which can be more easily joined. The main coil is designed to operate at up to 6 T with a current of 45.3 A. The inductance of the main coil is 210 H. We confirmed the design parameters sent by Cryomagnetics before the various portions of the solenoid were wound. This was done by independently calculating the magnetic field and homogeneity for the coil design and verifying the shield coil calculation. More details of these calculations can be found in Appendix A.

In addition to the main solenoid, the magnet has a smaller "Z0" shim coil, which allows us to modify the magnitude of the magnetic field at field center without changing the current in the main solenoid. This Z0 coil has a central field value of ± 0.5 T with a current of ± 39.7 A. The inductance of this coil is 1.8 H and the mutual inductance to the main coil is -9.4 mH. This means that charging the Z0 coil, even from 0 A to 39.7 A, will only induce a current change of 1.8 mA in the main coil, which corresponds to 2×10^{-4} T.

The magnet also contains a full set of 11 superconducting shim coils, including Z, Z^2, Z^3, X, Y, ZX, ZY, C2, S2, Z^2X, and Z^2Y, to provide a uniform magnetic field at

the magnet center. These shim coils are designed to operate with a maximum current of 1 A. Additionally, the magnet has a passive shield coil [79] as described above. Our main source of magnetic noise is from the subway — 50 nT (10 ppb) fluctuations as measured with a magnetometer. The magnet used in the 2008 measurement, with a shielding factor of 156 [70, 80], reduced these to ∼0.06 ppb fluctuations on the magnetic field experienced by the electron. The new magnet was designed to have a much higher shielding factor. Careful tests were performed at Cryomagnetics to optimize the number of turns in the shield coil to maximize the shielding factor in-situ using a 3-coil "Maxwell" configuration to produce a nearly-uniform external magnetic field across the solenoid. These tests resulted in a shielding factor of $\gg 1000$ (limited by the precision of the NMR probe used for the test) when the number of turns in the shield coil was optimized. This is an order of magnitude better than our previous magnets and should reduce the fluctuations from the subway further, to $<$10 ppt fluctuations experienced by the electron. Since we are looking to measure the cyclotron frequencies to $<$0.1 ppb this improved shielding should be more than sufficient.

The magnet is designed to operate in persistent mode. This means that once the magnet and shim coils are charged, several superconducting switches allow the magnet charging leads to be disconnected and removed from the dewar. This drastically cuts down helium boil-off.

The inner bore of the superconducting magnet has a diameter of 5" and, unlike other magnets in our lab, is always at 4K (while the magnet is charged) and shares the same helium space as the dilution refrigerator. The outer diameter of the dilution

refrigerator tail fits inside the magnet bore with a 0.040" clearance on the radius. The magnet form provides structural support for the dilution refrigerator, which rests on top.

When the superconducting magnet was first tested at Harvard, we discovered that the X and Y shims were not working. After much investigation, we ultimately had to open up the dewar to access the magnet. The problem was traced to a broken wire on the X shim persistent switch heater. As this was not a superconducting joint, we were able to repair the broken connection ourselves.

Charging the magnet from zero, or even changing the magnetic field can induce large mechanical stresses in the magnet windings. As these stresses settle out, the magnetic field value also changes. If the magnet is not charged properly, this settling time can take months. In order to minimize the drift and settling time, we first overshoot the current target by a few percent, then undershoot by half as much, repeating a few times by ever smaller amounts before going to the target value. If charged correctly, the magnet is guaranteed to have a stability of <10 ppb/hour and should eventually have a stability of better than 1 ppb/hour. A preliminary measurement suggests the magnet has a stability of ~ 0.2 ppb/hour.

3.2.2 The Dewar

Our magnet and dilution refrigerator insert both go into a specially designed, large-capacity dewar manufactured by Precision Cryogenic Systems. The main belly of the dewar has a capacity of more than 500 liters of liquid helium. It is cooled by a 190 liter nitrogen dewar. The average helium boiloff of the dewar is 0.5", or 7.5

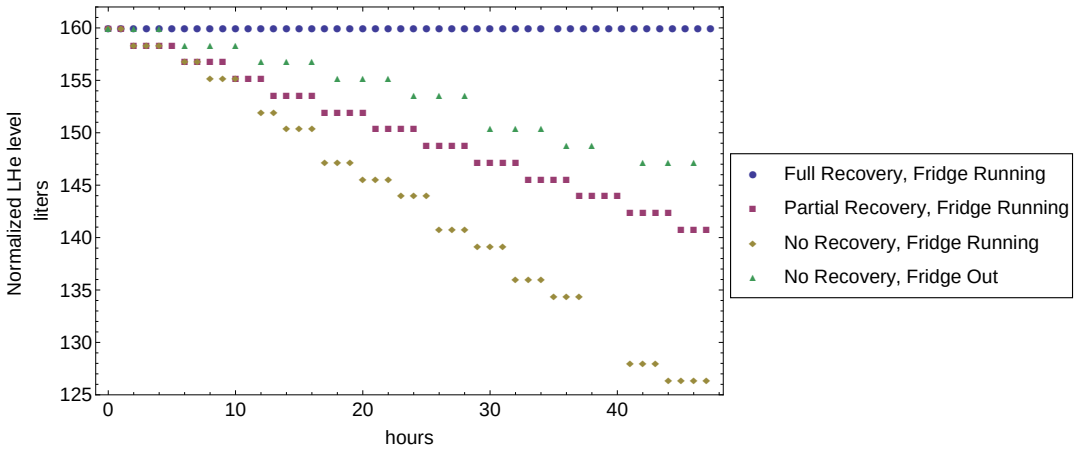

Figure 3.4: Helium boil-off rate in various configurations as described in the text. For clarity, all plots have been normalized to a starting level of 160 liters.

liters, per day. With the dilution refrigerator installed and running the boiloff rate increases to 1.1", or 18.3 liters, per day. Due to cost considerations of using this volume of liquid helium, we chose to install a helium reliquefier[10] into our system. With all of the dewar exhaust (but not the exhaust from the 1K pot pump of the dilution refrigerator) going through the reliquefier, we were able to cut our helium use with the fridge in and running down to 0.6", or 9.8 liters, per day. Installing an oil-free pump for the 1K pot and closing the cycle by running the exhaust through a liquid nitrogen cold trap and then into the reliquefier brings the loss rate to zero with the reliquefier running. Typical helium boil-off rates in these various configurations can be seen in Fig. 3.4.

The biggest downside to using the reliquefier is that it adds extra vibrations into our system, which we are otherwise very careful to eliminate [70]. We use the remote motor option from Cryomech, which allows the cold-head motor to be a few feet

[10]Cryomech PT415-Remote Motor Re-liquefier

away from the cold-head mounted on the dewar top. It is not yet known whether the additional vibrations from the reliquefier will affect the measurement of the cyclotron and anomaly frequencies. Vibration studies are underway and we will likely need to add further vibrational damping along the compressor lines and along the remote motor line to damp out unwanted vibrations.

Unlike many standard dewars which are fully welded together, our custom dewar is able to be opened on either end via large o-ring and indium seals. This has been a crucially important feature. As described above, the magnet arrived with a broken shim persistent switch heater wire, necessitating the removal of the magnet from the bottom of the dewar via the removal of the large o-ring sealed bottom plate, two cold-shield plates, and the indium-sealed bottom plate into the helium space. Additionally, once the dewar was in operation, we found that the liquid nitrogen hold time was much shorter than the expected value ($\sim$4 days instead of the quoted 8 days). This time, we broke the large o-ring seal on the top plate of the dewar and hoisted the "guts" of the dewar up out of the outermost aluminum cylinder. This revealed that the superinsulation had fallen off in several places, leaving two large patches of the nitrogen dewar exposed as shown in Fig. 3.5. We pulled as much of the fallen superinsulation up as possible and then added an additional 80-layer "blanket" sent to us by Precision Cryogenics to the top of the nitrogen dewar. This fix approximately doubled our nitrogen hold time, bringing it up to 7-8 days instead of 3-4.

Figure 3.5: These are the two large gaps in superinsulation on the nitrogen dewar as delivered.

Pressure Regulation

In order to minimize fluctuations of the system due to thermal effects, we carefully regulate the pressure in all cryogen spaces in the dewar. In the old apparatus used in the 2008 measurement, we independently regulated the pressure in two helium and three nitrogen spaces using a set of pressure transducers and regulator valves. The experiment helium space was regulated to 0.5 mpsi, with the magnet helium pressure regulated to 0.2 mpsi. The magnet nitrogen space was regulated to about 0.5 mpsi, and the other two nitrogen spaces were regulated to 2-4 mpsi. In the new apparatus, we use the same system of pressure transducers and regulator valves to regulate the pressure in the nitrogen space to 2 mpsi. The pressure in the helium space is regulated by the reliquefier in our closed-loop system. When it is working well, the reliquefier pressure locking loop can regulate the pressure in the helium space to about 0.3 mpsi.

3.2.3 The Dilution Refrigerator

Our dilution refrigerator is a custom JDR-500 from Janis Research Company. The entire apparatus can be seen in Fig. 3.3. The different stages of the dilution refrigerator along with their typical temperatures can be seen in Fig. 3.6. Before adding all of the traps, amplifiers, and wiring, the dilution refrigerator had $\sim$330 µW of cooling power at 100 mK and a base temperature of $\sim$16 mK. With the traps and all of the wiring installed, the cooling power is somewhat reduced but still more than adequate. The dilution refrigerator has an extended tail section, thermally anchored to the mixing chamber, that allows plenty of room for the trap vacuum enclosure as well as all of the DC and RF wiring and amplifiers and the positron source.

The dilution refrigerator has several non-standard features to provide maximum stability for our measurements. The most important feature is that the fridge is designed to sit on top of the magnet, rather than hanging from the top of the dewar as is the usual design. The IVC tail is inserted into the magnet bore and the upper IVC rests on the magnet top. A series of carbon fiber posts fix the mixing chamber to the IVC. A flexible section between the still and 1K pot allow for thermal contraction. A system of two bellows at room temperature absorbs pressure changes in the dewar helium space or in the room without lifting the IVC from the magnet. This design provides much better mechanical connection between the two halves — electric and magnetic — of the Penning trap. Additionally, the dilution refrigerator is designed with a series of centering pins to provide radial alignment. A pin on the trap can aligns the trap can with respect to the still radiation shield. The still shield is aligned to the IVC tail by three centering pins. The IVC tail also has a pin that mates with

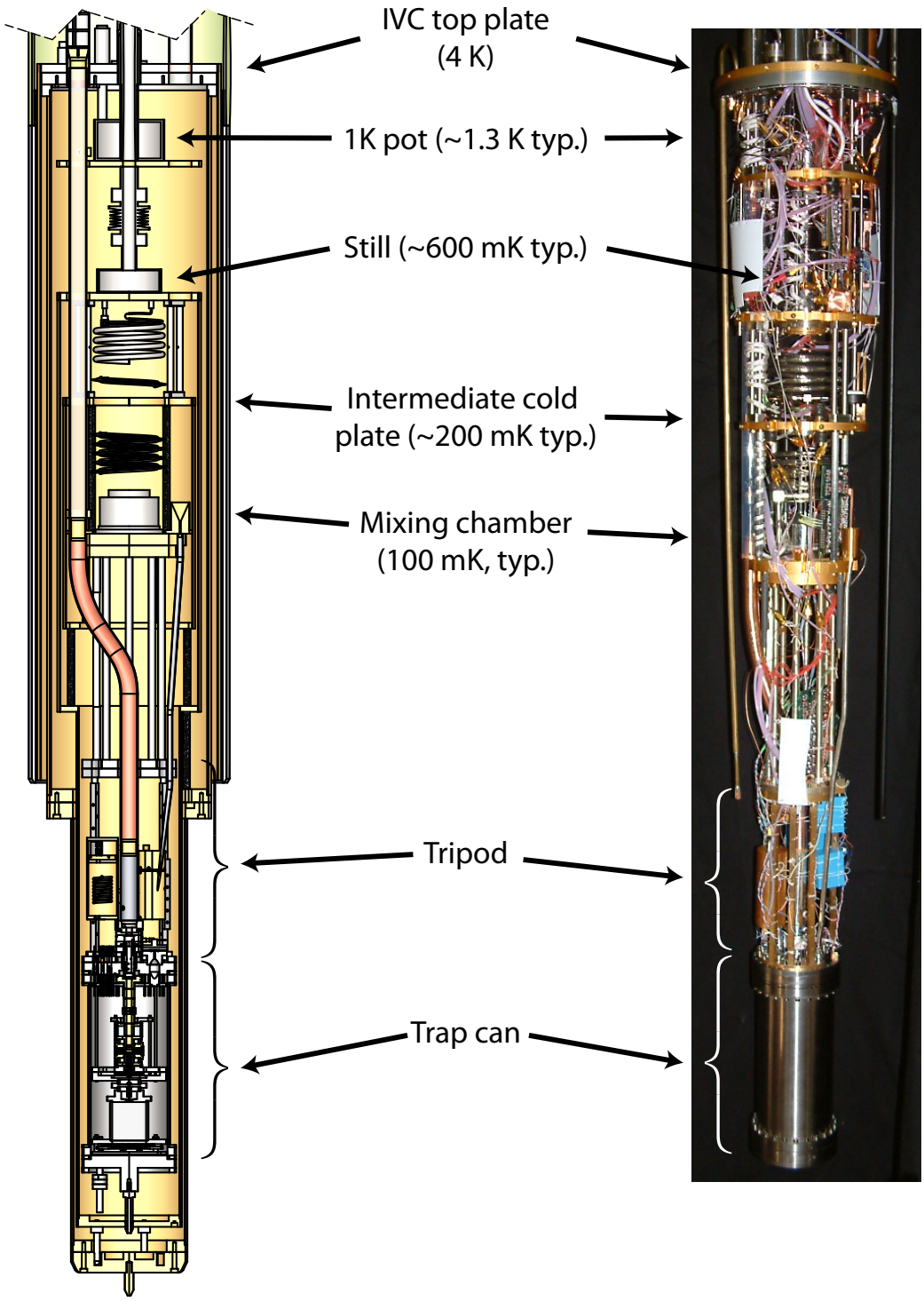

Figure 3.6: A cut-away model of the dilution refrigerator (left) and photo (right) with the stages and typical temperatures labeled.

the bottom plate of the magnet to align the dilution refrigerator tail to the magnet bore. These centering pins align the trap can center with the magnet center to better than 0.04".

3.2.4 Old vs New Apparatus

The apparatus used in the 2006 and 2008 measurements evolved historically and as such was not optimally suited to a high-precision measurement. The new apparatus has several distinct advantages over that previous apparatus. The majority of these improvements are based around increased stability, especially with regards to magnetic and thermal fluctuations.

1. The biggest advantage is the improved mechanical linking of the Penning trap electrodes with the superconducting solenoid. As can be seen in Fig. 3.7, and described above, the support path between the electrodes and the solenoid in the new system is much shorter than in the old system, and is entirely between 4 K and 100 mK, rather than going from 100 mK to 300 K and back to 4 K as in the old system.

2. The tight tolerance between the dilution refrigerator tail, the shorter lever arm and the series of radial centering pins described above should provide greatly enhanced radial alignment of the electrodes with respect to the magnet center.

3. The superconducting magnet has a better shield coil to reduce magnetic fluctuations as mentioned above.

4. The large volume of the helium dewar provides more time for data-taking be-

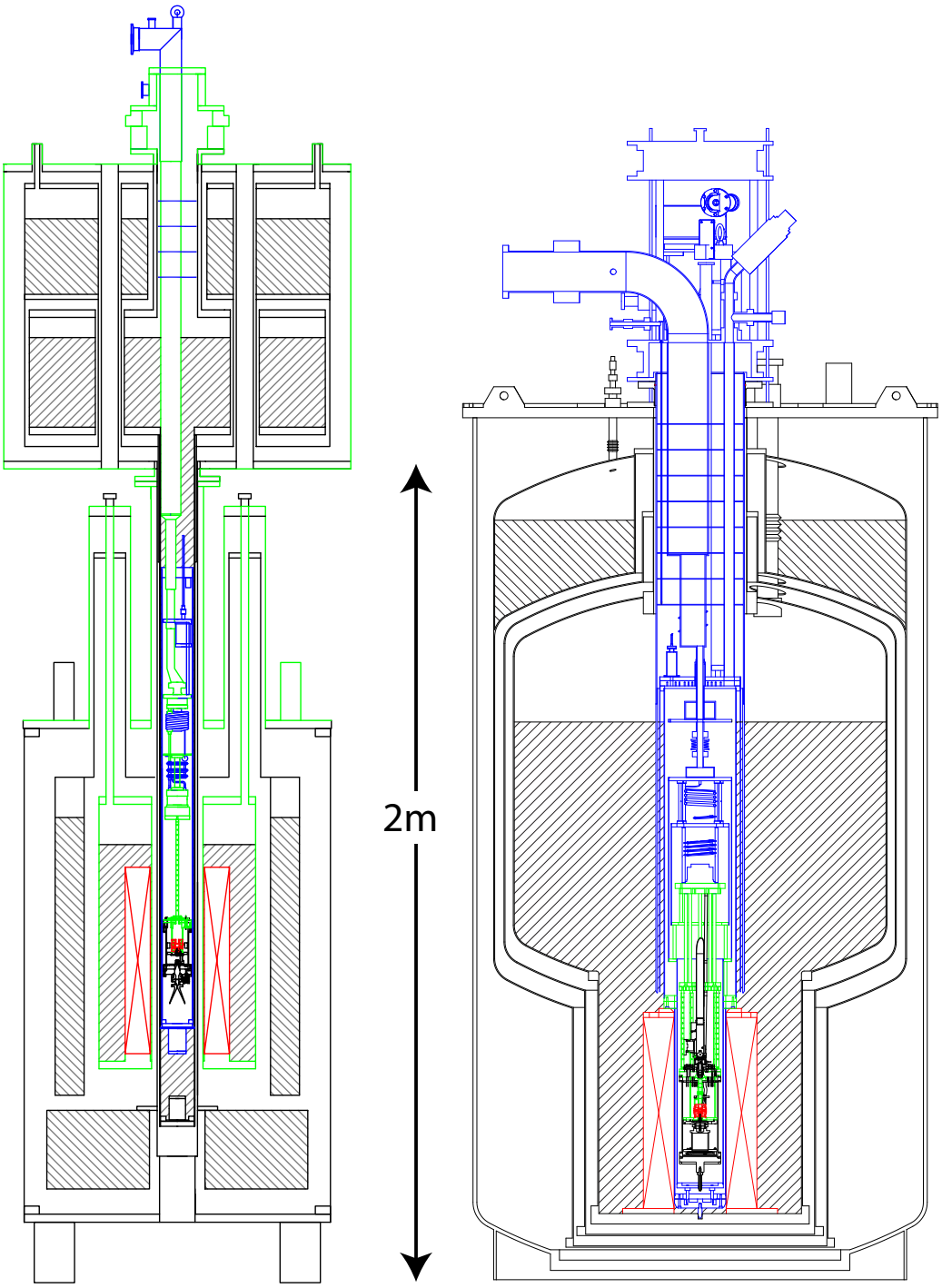

Figure 3.7: A comparison of the old apparatus (left) and the new apparatus (right). The Penning trap components (magnet and electrodes) are shown in red. The structural support between the two components of the Penning trap are shown in green. The dilution refrigerator is shown in blue.

tween disruptive fills. The installation of the helium reliquefier could drop the number of fills to zero, provided it does not add additional vibrations that would reduce our stability.

5. The new dilution refrigerator includes plenty of room for a retractable positron source. This will be described in detail in Chapter 4.

6. The larger diameter of dilution refrigerator provides more room for electronics, allowing us to install multiple traps, each with their own amplifiers.

Taken together, these improved features should provide an ideal platform for performing precision measurements of the g-value of a single electron and positron.

3.3 Inserting and Removing the Dilution Refrigerator

Because the superconducting magnet and the dilution refrigerator share the same liquid helium space in the dewar, cooling down (and warming up) the dilution refrigerator is not a trivial endeavor. The dilution refrigerator is designed with a special aluminum and G-10 outer sleeve that mates with a cryogenic o-ring[11] at the top of the dewar neck to prevent air from entering the helium space (see Fig. 3.8). However, there are two complicating issues. First, the sliding seal sleeve stops short of the dilution refrigerator tail containing the trap so that it can fit into the magnet bore. This means that the fridge has to be lowered over 18 inches before the sliding seal is

[11] Astra Seal by Creavey Seal Company — a stainless steel spring encased in teflon that is designed to remain flexible down to 23 K

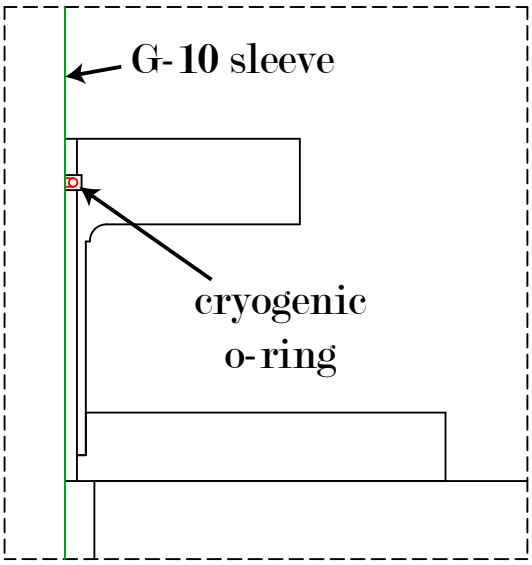

Figure 3.8: Detail view of the dilution refrigerator sliding seal showing the cryogenic o-ring mating to the outer sleeve of the dilution refrigerator.

engaged. Second, the need to cool the fridge slowly enough to not boil off too much helium or quench the magnet results in a lowering time of around 4 hours. The sliding seal does not make a perfect seal (helium gas can occasionally be felt exhausting through it) and the outside of the sliding seal sleeve gets very cold and icy during this time (as cold helium vapor is continually exhausting up through it to vapor cool the fridge). Both of these could result in ice contamination inside the helium space.

During the initial trial phase of using the new dilution refrigerator we had to warm up the entire dewar three times due to ice accumulation in the dewar, particularly within the magnet bore. Oxygen ice in particular is a serious problem. Oxygen ice — which is paramagnetic — preferentially accumulates on the inner surface of the magnet bore (the location of strongest magnetic field). The clearance between the magnet bore and the dilution refrigerator tail is only 0.04" on the radius, and there

is only a 0.54" clearance between the bottom of the dilution refrigerator and the bottom plate of the dewar, so it doesn't take an overly large amount of ice buildup to prevent the dilution refrigerator from seating fully in the magnet. Furthermore, even relatively small amounts of oxygen ice could add a source of magnetic noise to our precision measurements. For these two reasons, it is imperative that we prevent as much air as possible from entering the helium space.

We have developed the following procedure. We use a large, 4-handed plastic glove bag[12] with two large openings, one of which we fasten around the dewar neck with an elastic cord and the other of which we fasten around the outside of the dilution refrigerator with a second elastic cord. This is done while the dewar helium space is closed off with a Plexiglas plate. The bag is purged with helium gas for more than 15 minutes. We then remove the plate covering the opening in the dewar neck (inside the glove bag) and slowly lower in the fridge. We continue to flow helium gas at a low rate into the glove bag while lowering the fridge. When the fridge is almost fully down, we undo the elastic cord at the top holding the glove bag in place, remove the dewar cover, and set the fridge down fully.

This procedure is done in reverse to pull the fridge out of the dewar, with the difference being that we are able to pull the fridge out in about 10 minutes as opposed to the 4 hours it takes to cool. This procedure works remarkably well at keeping air out of the dewar and preventing ice accumulation.

[12]Spilfyter® Hands-in-bag® from NPS Corp., part no. 690341 (VWR part no. 15552-194)

Chapter 4

The Retractable Positron Source

One of the major advances of this thesis, not to mention one of the driving reasons in building the new apparatus, is the inclusion of a positron loading scheme. The old apparatus did not have space to install a radioactive positron source that could either be moved out of the way or blocked to prevent unwanted loading. The new apparatus provides plenty of room for the installation of a retractable positron source. The retractable positron source system and the positron loading method will be described in this chapter.

4.1 Positron Loading Method

Sodium-22[1] preferentially decays radioactively via β^+ (positron) decay into a Neon-22 atom with a 90% probability. The positron is emitted with a maximum energy of 546 keV. These emitted positrons are too energetic to trap, so energy must be removed if the positrons are to be trapped. The previous measurement of the

[1] half-life of 2.6 years

positron g-value, from the University of Washington, required the use of two hyperbolic Penning traps [11, 81, 52]. Positrons were loaded off-axis from a 0.5 mCi ^{22}Na source located above the upper Penning trap. An external damping circuit was used to damp the axial motion of the positrons so that some of them could be trapped. The off-axis loading was done to increase the time available for resistive damping (due to the large magnetron orbit created by the off-axis loading). Once some positrons were trapped, they were then transferred to a second hyperbolic trap for the measurement using a fast ($< 10\,\mu$s) pulse. However, the loading rates from this type of loading were generally quite small, approximately 23 positrons per hour (46 e^+/hour/mCi) for the University of Washington experiment [81], and not well understood [82]. Early work towards antihydrogen improved on this method by using a reflection moderator to de-excite the positrons before they entered the trapping region where an external damping circuit enabled some of them to be trapped [82, 83]. This achieved a loading rate of around 700 positrons per hour from a 10 mCi ^{22}Na source (approximately 70 e^+/hour/mCi).

The positron loading method used in this thesis was developed more recently in the ATRAP antihydrogen collaboration as a means to accumulate very large numbers of positrons [84, 85, 86]. Because the accumulation rate is linear, we are able to adapt the method to load modest numbers of positrons from a very small source. In this method, the energetic positrons emitted from the source are passed through a single crystal tungsten moderator, which slows them down. A small fraction of the slowed positrons pick up an electron from the surface of the moderator, forming a loosely-bound state of Rydberg positronium. The potentials on the electrodes are carefully

tuned to create an ionizing electric field within the trapping potential well which can strip away the electron to carry away the energy and momentum, leaving the positron behind in the trap. By reversing the electrode potentials it is possible to trap electrons in the same way. In fact, this is one of the signatures used to confirm that positrons are in fact being loaded via field-ionization of positronium and not some other method. The loading rate depends on the size of the source, the geometry of the trap, and several other factors, as discussed in the next section.

4.2 Estimating Loading Rate

The goal is to adapt the positronium ionization method of positron loading for use in our precision apparatus. We would like to use the smallest source possible for safety and stability reasons as discussed in Section 4.6. But it is also desirable to have a reasonable positron loading rate. While only one positron is ultimately needed for a g-value measurement, the initial stages of tuning and optimization are much easier with a small cloud of positrons that can more easily be detected. Being able to load such a cloud in a relatively short amount of time is thus advantageous. Given these two competing considerations, a target loading rate of $1\,e^+/\text{min}$ was chosen.

In ^{22}Na, approximately 90% of decays produce positrons. Thus a $10\,\mu$Ci source produces 3.3×10^5 e^+ per second. Of these, 50% will be traveling forward (or in our case, downward) from the source and the other 50% (traveling upward) are lost. Previous work with larger sources suggests that up to 50% of the positrons emitted in the forward direction will be absorbed within the source capsule itself [83]. However, given that our source activity is 1000 times smaller, with a nearly identical active

diameter (0.1" for ours compared to 0.120" in previous sources), we expect this loss to be smaller. Additionally, up to 33% are expected to be absorbed within the source vacuum window [85, 87, 88]. Therefore, as few as 17% of the positrons produced through radioactive decay in the source will ultimately emerge from the source capsule in the forward direction.

Upon leaving the source capsule, up to 33% of the remaining positrons are again expected to be absorbed as they pass through the 10 μm titanium vacuum window into the trap can [85, 87, 88]. As the positrons leave the source, they undergo cyclotron motion due to the presence of the magnetic field. As the positrons travel through the spatially varying magnetic field, the kinetic energy of the cyclotron motion increases by a factor of B_z/B_{source} as they travel from the source to a position z. Due to energy conservation, this increase in kinetic energy has to come from somewhere, and it in fact comes from the positrons' "axial" kinetic energy (their energy parallel to the magnetic field lines). Thus, as they travel from the source to the moderator, their cyclotron energy increases at the expense of their axial kinetic energy. Positrons emitted at an angle (with respect to the field lines) greater than some critical angle, defined to be

$$\sin\theta_c = \sqrt{\frac{B_{\text{source}}}{B_{\text{moderator}}}} = 0.93, \tag{4.1}$$

do not have enough axial kinetic energy to reach the moderator before all of the axial energy is converted into cyclotron energy. This decreases the actual flux reaching the moderator by a factor of $1 - \cos\theta_c$. In the end, we expect 7-14% of the positrons emitted by the source to reach the moderator (depending on the amount of self-absorption in the source capsule). Although some studies have been done on Ps

formation from positrons on metal surfaces [89, 90, 91], the fraction and distribution of Ps from single crystal (W100) tungsten at cryogenic temperatures is not known and is likely to depend on surface contaminants. Nevertheless, previous work on a similar loading system [84, 85, 92] suggests that about 1 out of every 7.5×10^7 positrons incident on the moderator results in a trapped positron from positronium ionization with a transmission moderator. Assuming a similar rate for our system would yield a trapping rate of approximately 1-2 e^+/min from a 10 μCi source. However, if we load directly into the closed-endcap precision trap, we also have to account for the solid angle loss due to the small hole in the top endcap through which the positronium must pass. The hole in the top endcap is an order of magnitude smaller than the active area of the source. Taking into account the distances and the magnetic compression but ignoring the effects of the positronium radius, the trapping rate would be reduced by an additional 98.8%. The result would be a trapping rate of order 1 e^+/hour.

While we ultimately need only one positron to measure the g-value, it is helpful to be able to accumulate small to medium sized clouds of particles, especially during the initial stages of finding particles and tuning the trap. It is much easier to scan for a cloud that can easily be seen as a dip in the amplifier noise resonance than to look for one or a small number of particles when you do not know exactly where to look. With a trapping rate of order 1 e^+/hour, accumulating even one hundred positrons would require over 4 days of continuous loading. Even once the trap is fully tuned, it would still be helpful to be able to load one or a few positrons faster than once every few hours.

4.3 Loading Trap

Two obvious choices exist to increase the loading rate: use a larger source or install a second trap with a larger opening to minimize solid angle losses. For safety reasons, as well as the relative availability of commercial sources of various sizes, we chose not to use a larger source and opted instead to install a second Penning trap to use for positron accumulation, described below.

To maximize access into the positron loading trap, and thereby maximize the positron loading rate, we decided to use an open-endcap cylindrical Penning trap [57]. The design for the trap was based on the precision trap from the proton magnetic moment experiment [62], using silver and fused quartz in place of copper and macor. Adjustments were made to require only a single spacer size and to account for the differential thermal contraction of the silver electrodes and the fused quartz spacers. The procedure used to prepare the loading trap electrodes was similar to that used to prepare the precision trap electrodes as discussed in Section 3.1.1. The silver[2] electrodes are carefully polished by hand on a lathe using the procedure described earlier. Due to intermittent trouble with the hydrogen brazing oven, the bias wires were soft soldered using a hot plate to heat the electrode as well as a wide-tip soldering iron to apply extra heat to the joint. Because the surface finish is less important for these electrodes, we opted to electroplate a thin layer of gold onto the surface using the TG-25 gold plating solution[3], diluted 3:1 with DI water. This yielded an adequate finish in less time than it would have taken to perform the thermal evaporation.

[2] 4N (99.99%) purity was chosen instead of the 5N purity of the precision electrodes for cost considerations as well as the fact that the loading electrodes are further away and thus any magnetic impurities will matter less in the final measurement

[3] from Technic, Inc

As in the precision trap, the compensation electrodes of the loading trap are split to allow the magnetron sideband cooling drive to be applied to one half of the bottom compensation electrode. The compensation electrode halves are kept isolated from each other by small sapphire spheres. Transfer electrodes placed on either side of the 5-electrode trap are designed to mate with the pinbase bottom and the top endcap electrode of the precision trap while minimizing additional capacitance to the precision top endcap so as not to affect the resonant frequency or Q of the precision trap first stage amplifier. These extra electrodes are used to control the voltage and electric field profile for loading and to facilitate transfer of the accumulated positrons from the loading trap to the precision trap. The whole electrode stack, including both traps and the transmission moderator, can be seen in Fig. 4.1.

4.4 Heat Treating the Moderator

Experience suggests that it is necessary to properly heat treat the moderator before use. Our moderators are 2 μm thick single crystal tungsten, (100) orientation. A few attempts were made at loading positrons and electrons from the source into the closed end-cap precision trap using an untreated moderator, but without success. It is not known whether the failure was due to the lack of heat treating or from trying to load directly into the precision trap. We then proceeded to heat treat the moderator. The main reason for heat treating is to remove bulk carbon as well as the oxide layer on the tungsten crystal. The heat treating process chosen is a standard, two-step procedure [93] that was also used previously in ATRAP [86]. Step one is to remove the carbon by heating the tungsten to 1200-1500 °C in oxygen at 10^{-4}-

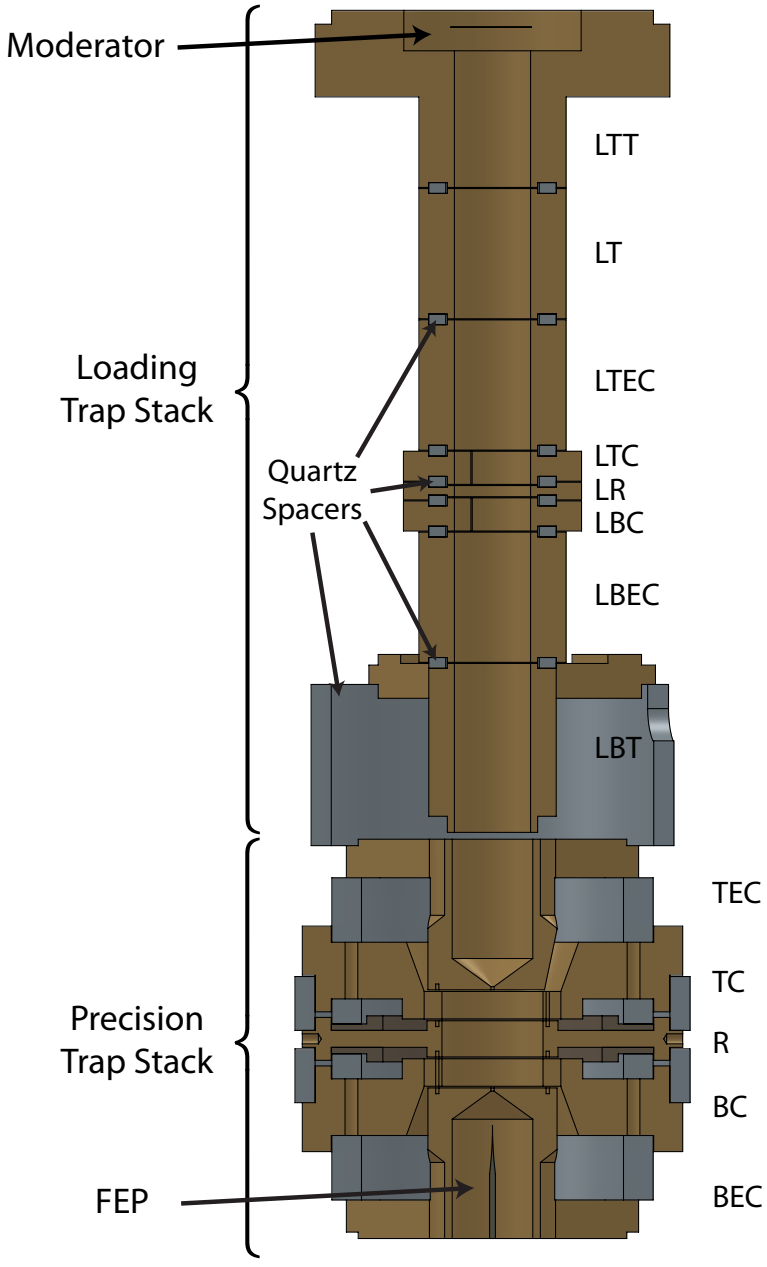

Figure 4.1: Full electrode stack showing the moderator, loading trap, precision trap and FEP.

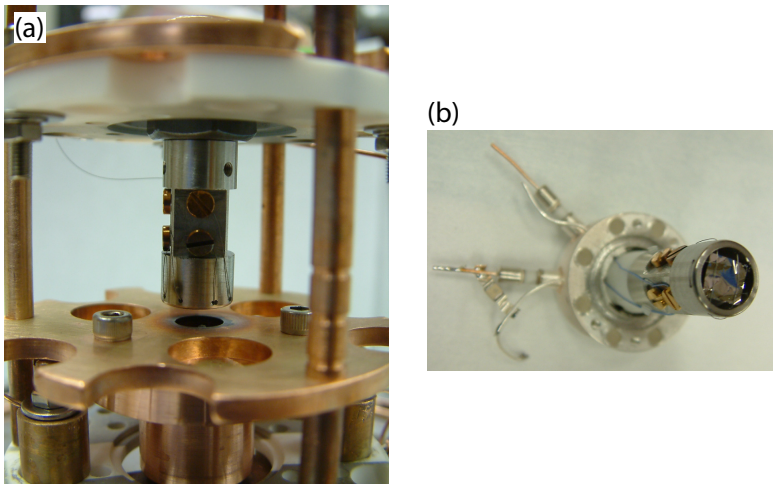

Figure 4.2: The moderator in the heat-treating set-up (a) and in the holder that is installed in the trap can (b).

10^{-5} Pa for 15-30 minutes. Step two is to remove the oxide layer formed in step one by repeated flashings to >2100 °C in ultra-high vacuum [86, 93]. Each of these steps is typically repeated multiple times per moderator. To do this, we mount the moderator right next to a tungsten light bulb filament inside a vacuum chamber. We hold the moderator at a high voltage (typically 1 kV) and apply a smaller (20-30 V) voltage to the filament. As the filament heats up, electrons are emitted and, guided by an external magnet, strike the moderator. An optical pyrometer is used to monitor the temperature of the moderator during this process. A turbo pump is used to keep the chamber at a low vacuum and a variable leak valve is used to let in a small amount of oxygen. Fig. 4.2 shows the moderator holder in the heat-treating set-up as well as the moderator and holder ready to be installed in the trap can.

Once the heat-treating has been performed, care is taken to keep the moderator under vacuum as much as possible, although the moderator used in this thesis spent approximately one day in atmosphere before it could be installed in the trap can and

the trap can pumped out. Additionally, the moderator has spent several fractions of a day in atmosphere when it was necessary to open the trap can at several points to fix connections inside the trap can.

4.5 Source Delivery System

For our positron source, we use a ^{22}Na sealed button source[4] that was 15.6 μCi on Dec. 1, 2009 and between 6.9 and 6.3 μCi when the data in this thesis was taken. Some care must be taken to protect researchers from the gamma radiation emitted from this source, although the small size greatly reduces the danger. The source is placed in a small two-piece capsule, with the top made from Elkonite (90% Tungsten, 10% Copper by weight)[5] to provide some shielding and the bottom made from titanium. This capsule, shown in Fig. 4.3a, allows easier handling of the source. A rotational vacuum feedthrough at the top of the dilution refrigerator turns a spool on which is wound a nylon string[6] that is attached to the source capsule, as can be seen in Fig. 4.3b. This allows the source capsule to be raised and lowered inside the inner vacuum chamber of the dilution refrigerator. Pairs of LEDs[7] and photo-diodes[8] as well as markings on the string are used to monitor the location of the source. The source is raised and lowered by hand.

When loading positrons, the source is positioned directly above the 10 μm titanium vacuum window into the trap vacuum enclosure. When not loading, we need to be

[4]Isotope Products Laboratories custom diameter POSN source
[5]density = 17.23 g/cm^3
[6]Daiwa Samurai Braid 55 lb fishing line
[7]Opto Diode Corporation OD-880W
[8]Hamamatsu S2386-18K

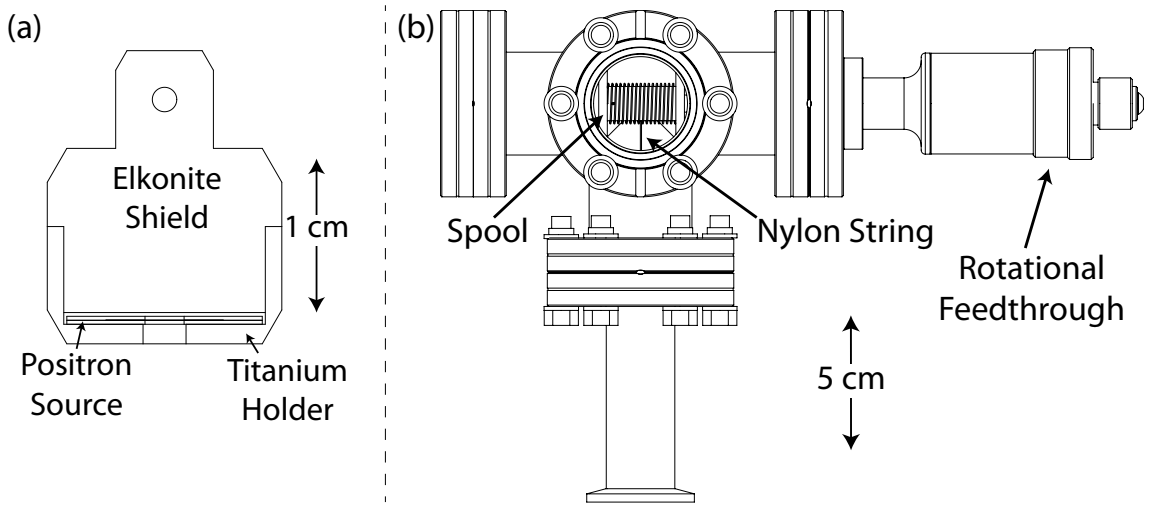

Figure 4.3: (a) Close up diagram of the positron source capsule. (b) Positron source lowering assembly.

able to move the source up and out of the way in order to prevent further, unwanted loading or heating from positrons and gamma radiation. We pull the source up from the loading position (on the central axis) through a carefully bent copper tube that brings the source into the off-axis clear-shot hole that runs down the side of the dilution refrigerator. The source must travel a vertical distance of 17 inches and a horizontal distance of 2 inches between the loading position and the storage position (see Fig. 4.4). Since this storage position is both far away and off-axis from the loading position, it effectively blocks further positrons and gamma rays from entering the trap. The source can be further raised if desired, including being removed entirely when it is necessary to do work on the experiment in order to provide extra protection to the researchers.

The dilution refrigerator cannot handle a very large heat load at or below the mixing chamber and so care must be taken to maintain good thermal isolation between room temperature and the various stages of the dilution refrigerator. To accomplish

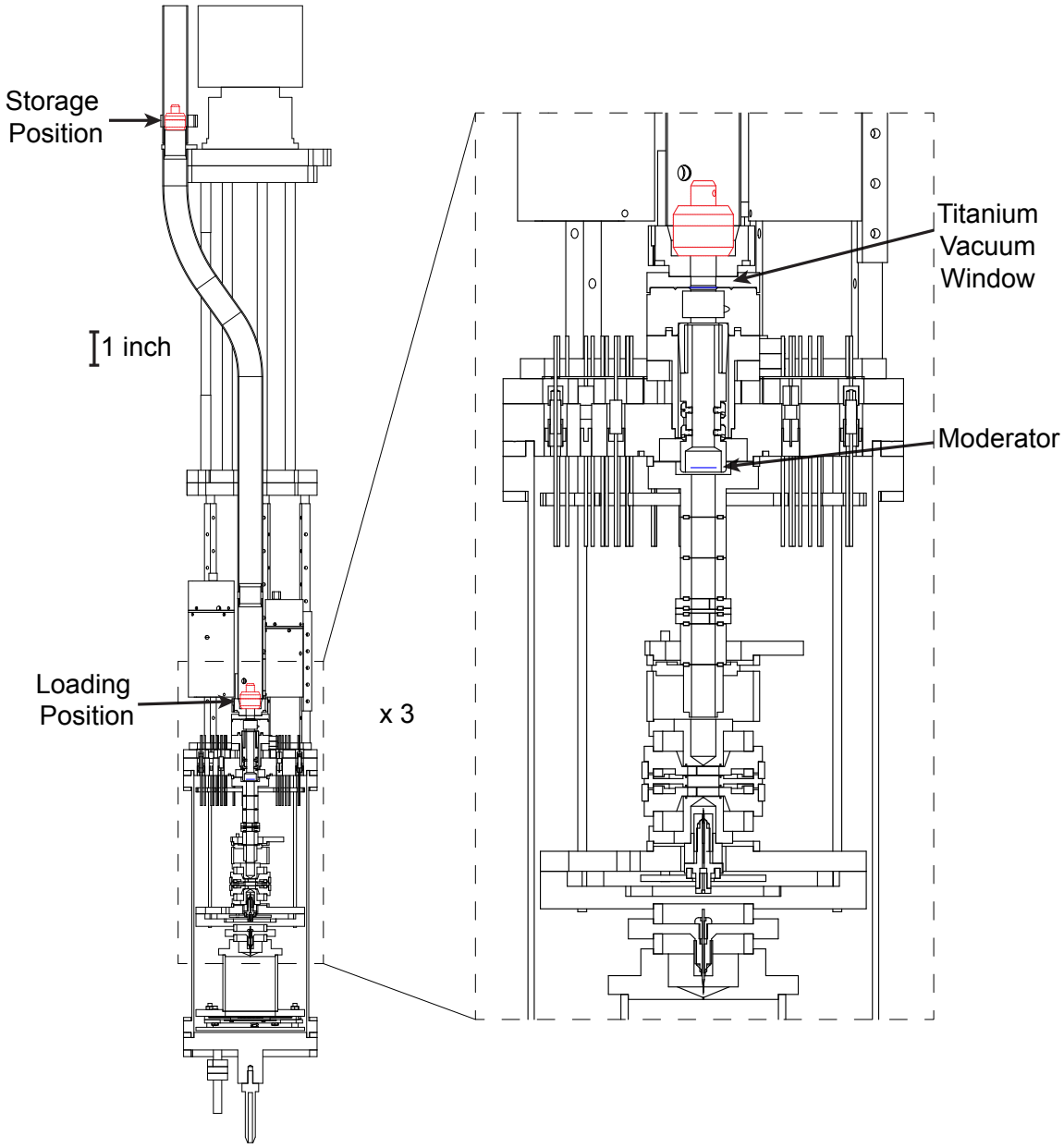

Figure 4.4: Positron source storage and loading positions

this we have a set of 8 baffles that float on the string holding the source. The central holes in these baffles, through which the string passes, are offset to block room temperature radiation down the center. As the source is lowered from the top of the fridge down to the 4K plate of the IVC, a special blocking piece, which also floats on the string between the source and the baffles, mates with a horn mounted to the 4K plate. The baffles come to rest on this blocking piece and stay at the 4K plate to block room temperature radiation while the source remains free to be further lowered. This set-up can be seen in Fig. 4.5.

4.6 Radiation Safety

As mentioned in Section 4.5, some care must be taken to protect researchers from the radioactive positron source. The three main features of radiation safety are time, distance, and shielding. Decreasing the time spent near a radioactive source, increasing the distance from a source, or increasing the shielding around a source can all cut down the radiation exposure from the source. The small size of our ^{22}Na source provides much of the protection and is one of the reasons we chose to use the smallest source possible. Larger sources require significant safety precautions, including substantial shielding both in and around the apparatus. Great care must be taken to ensure a large source does not get stuck in a cryogenic apparatus, thus rendering the apparatus unusable. With our small source, this is not a concern. Additionally, a larger source would be a larger source of noise when not loading and more effort would be required to block unwanted particles from interfering with the measurement. The small source used in this apparatus alleviates all of these concerns.

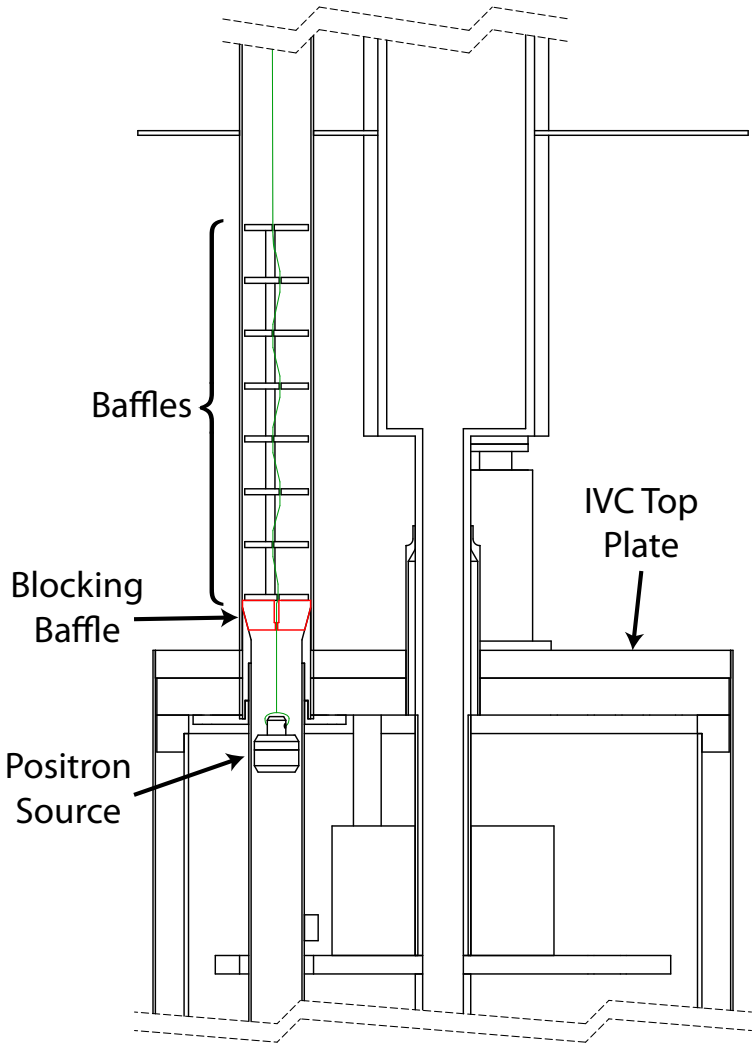

Figure 4.5: Positron source baffles.

Even with our small source, some minor precautions are taken. At 1 m from a 20 μCi unshielded ^{22}Na source the annual dose is a fraction of the average person's total annual dose. Therefore, limiting the amount of time spent within 1 m of the source is the only precaution necessary to achieve a negligible dose. The initial installation of the positron source into the holding capsule was done quickly and at arms length using tweezers to handle the source and then closing the capsule by hand. Once the source has been installed in the capsule, there is generally no need to remove it and the Elkonite shield provides some additional protection when handling the source. When the experiment is cold and running, there is no danger to the researchers, as the source is at the bottom of the fridge, nearly 3 meters below the floor, and surrounded by the layers of the dilution refrigerator, magnet, and dewar. If extended work needs to be performed on the fridge while it is warm, the source is removed entirely from the apparatus and stored in a lead-lined safe for maximum protection.

The source was cold-tested and vacuum-tested before installation to ensure it would not leak, thus contaminating our expensive apparatus, while in use. First the source was slowly lowered into liquid nitrogen, left for several minutes, slowly warmed back to room temperature and then tested for leaks[9]. None were found. The source was then placed in a vacuum chamber which was slowly evacuated (so as not to stress the thin foil seals on the source). We left the source under vacuum for about 30 minutes then slowly vented the chamber and again tested the source for leaks, finding none. With the source installed in the fridge, it is recommended to evacuate or vent the IVC slowly so as not to stress the foil seals on the source.

[9]This involved a visual inspection followed by a wipe test performed by the Harvard Radiation Protection Office

Chapter 5

A Trapped Electron and Its Resonances

The precision trap is the heart of the apparatus and the place where the g-value measurement will be performed. We need a reliable method to load a single positron or a single electron as well as a cloud of electrons to perform the various measurements that go into a determination of the g-value as discussed in Chapter 2. The standard way electrons are loaded into the precision trap, be it a single electron or a cloud of electrons is with a field emission point as described in Section 5.1. The best method for reliably loading a single positron into the precision trap is still being investigated and will be discussed in Chapter 7. In addition to particle loading, this chapter will discuss how we detect and drive the various particle motions in the precision trap.

5.1 Loading Electrons with the FEP

The primary way we load electrons into either trap, but especially the precision trap is by our lab-standard method of field emission. We make a field emission point (FEP), which is a thin tungsten rod etched down to an atomically sharp needle point on one end. We etch the field emission points following the procedure outlined in [74, Appendix A]. The field emission point is carefully positioned close to but not touching the bottom endcap of the precision trap. A small hole (.01" diameter) in the bottom endcap allows access into the precision trap cavity. We apply a large negative voltage (typically 400-800 V, depending on the quality of the tip) to the FEP. Field emission at the sharp tip causes electrons to tunnel from the surface. This stream of energetic electrons follow the magnetic field lines through the hole in the bottom endcap and some portion of them strike the top endcap electrode surface, knocking off some of the adsorbed gas. This gas then collides with the stream of electrons, knocking some of them into the trapping well. We can vary the number of electrons loaded by varying the voltage that we apply or the length of time over which we apply it. We monitor the current going to the FEP, and can also monitor the current from the FEP striking the various electrodes. For a given current and length of time, the number of electrons loaded is reasonably consistent. In this way it is fairly straightforward to load anywhere from one to a few hundred thousand or more electrons.

As described in Section 6.1, the FEP can also be used to load electrons into the loading trap. This method of loading was particularly useful in the initial characterization and tuning of both traps. Additionally, it is the fastest way to load electrons

into the precision trap for any reason, whether a single electron for a g-value measurement or a cloud of electrons for mode-mapping.

5.2 Biasing the Electrodes

Stability is crucial to a high-precision g-value measurement. In particular, maintaining high axial frequency stability is of the utmost importance. As was mentioned in Section 2.2 and will be discussed below in Section 5.4, the axial frequency shift due to a cyclotron or spin-flip is 1.7 Hz, or 8.5 ppb in our precision trap. It is important that we detect cyclotron and spin transitions with high fidelity and therefore it is necessary that the axial frequency be stable to a few ppb. To this end, we take great care with all of the DC and RF connections to the trap. All of the DC lines are on twisted pairs with multiple sets of RC and LC filters at room temperature, intermediate stages on the fridge, and at base temperature. To avoid ground loops, all ground connections are made at the pinbase. Floating supplies are used to source all of the important DC voltages. The RF lines have 20 dB cold attenuators installed at the 1K pot to cut down room temperature noise transmitted to the pinbase and additional capacitive voltage dividers at the pinbase. The wiring diagram for the precision trap can be seen in Fig. 5.1. More details of the RF connections are discussed in Section 5.6. Details of the amplifiers are discussed below in Section 5.3 and in [74] and [70].

There are five different modes in which we typically operate the precision trap:

1. normal (trapping)

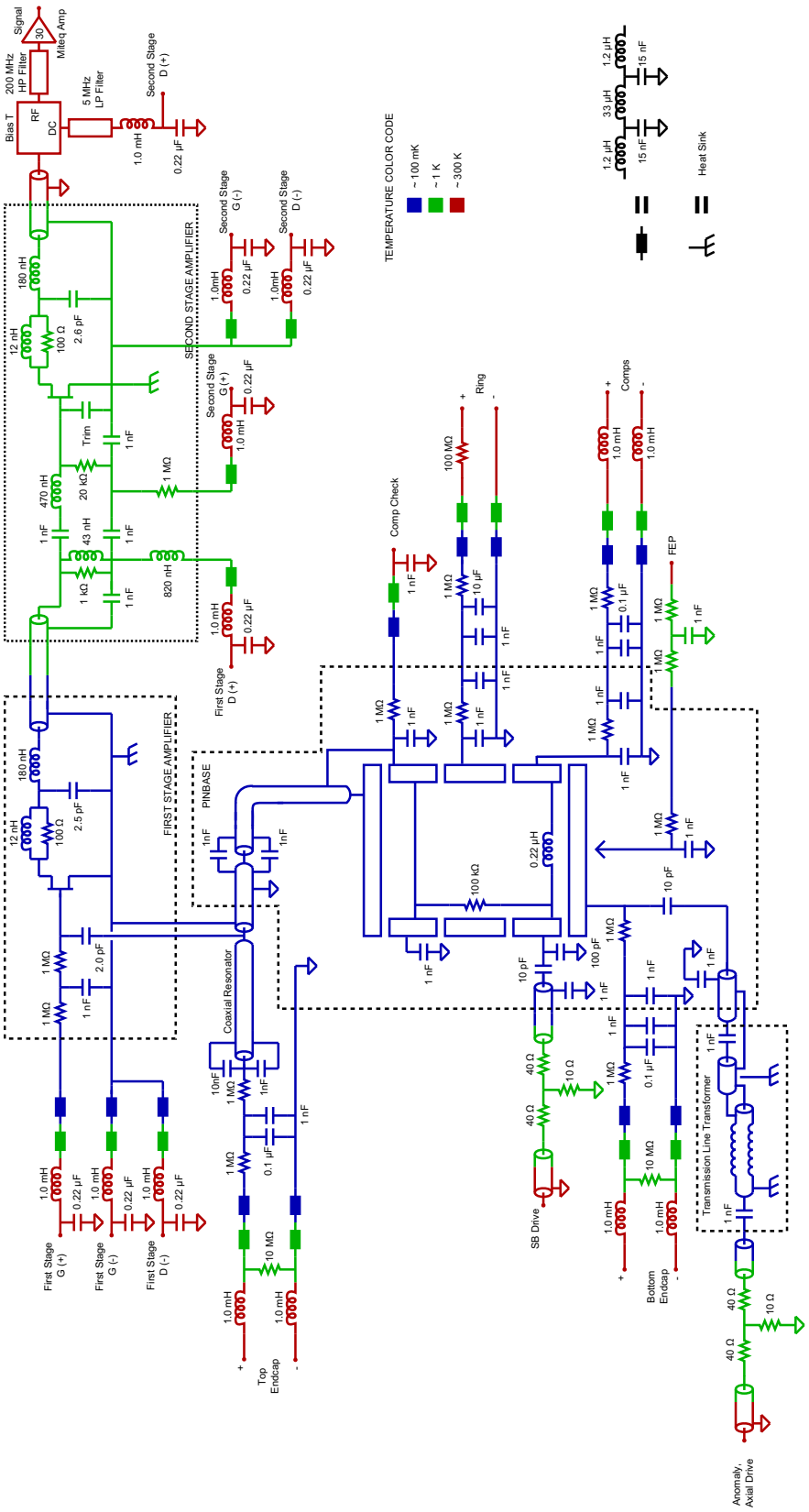

Figure 5.1: Precision trap electrode wiring diagram

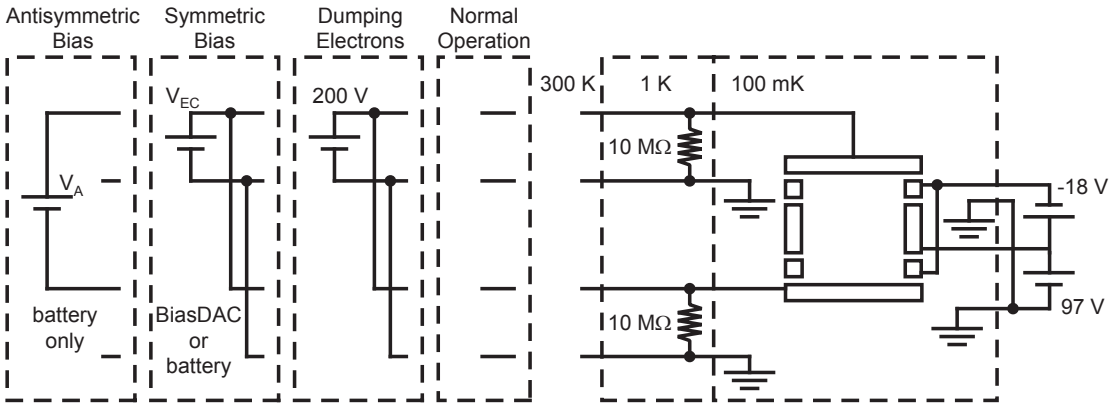

Figure 5.2: Typical endcap bias configurations. Note that the voltages shown here are for electrons. For positrons, the voltages would all have the opposite sign.

2. dumping particles

3. symmetric biasing of the endcaps

4. antisymmetric biasing of the endcaps

5. transferring from the loading trap.

The first four of these (shown in Fig. 5.2) involve changes only to the potential applied to the endcaps and will be discussed here. The last, transferring, will be discussed in Section 7.1.1. Under normal operation, we minimize the number of voltage sources by applying a trapping voltage of $\sim$100 V to the ring electrode while grounding the endcaps. Because the axial frequency is proportional to the square root of the trapping voltage, the trapping voltage must be stable to better than 10 ppb, or 0.1 μV in order to maintain an axial frequency stability of better than 5 ppb (1 Hz). We use a Fluke 5720A voltage calibrator to apply the ring voltage, V_R. The Fluke has a nominal stability of 500 ppb over 24 hours. To provide the necessary short term stability, we

charge a 10 μF capacitor located at base temperature at the tripod. Along with this capacitor, two resistors form an RC circuit with a long time constant (> 15 min) — a 1 MΩ resistor located at the pinbase (∼100 mK) and a 100 MΩ resistor located at room temperature where it can be bypassed for initial charging or large voltage changes on the ring line. Any leakage resistance must be eliminated to prevent it forming a voltage divider with the 100 MΩ resistor. We can monitor and lock the axial frequency by charge-pumping the 10 μF capacitor with 50 ms pulses from a BiasDAC[1] channel stacked on top of the Fluke. After the pulse, the Fluke voltage is updated to maintain long-term stability. Because the trap is orthogonalized[56], the stability requirement for the compensation voltage is much less stringent. We measure a frequency dependence of 7 Hz/mV, implying that we need a stability of 150 μV out of 79 V (2 ppm). Three BiasDAC channels are stacked on top of the Fluke to apply the compensation voltage, giving a range of ±50 V on top of the ring voltage. The compensation lines have 0.1 μF capacitors and 1 MΩ resistors. The endcap electrodes also have 0.1 μF capacitors and 1 MΩ resistors in the line, as well as well-matched 10 MΩ resistors to ground located at the still (∼600 mK). These cut down noise getting to the trap but still allow the endcaps to be biased when necessary. Under normal operation, the endcaps are grounded by these cold resistors.

While the endcaps are grounded during normal operation of the trap, they are often biased for other purposes as mentioned above. To quickly dump electrons from the trap, we briefly put a voltage that is roughly twice the ring voltage on both endcaps. This empties the trapping well without disturbing the ring voltage stability.

[1] A BiasDAC is a low-drift, computer-controlled digital to analog converter (DAC) that is manufactured in-house in the Harvard Electronic Instrument Design Lab.

We also take advantage of the shorter time constants of the endcap bias filters (100 ms) to make quick changes to the axial frequency. Symmetric biasing of the endcaps, where the same voltage is applied to each endcap, is used to detune the axial frequency from the amplifier to decrease the axial damping rate, e.g. for axial sideband cooling as discussed in Section 7.2.1. We have seen hysteresis in rapid detuning of the axial frequency that can be at least partially overcome by briefly overshooting the voltage when tuning back. We typically use a relay for the detuning/retuning so that the endcaps can be retuned by shorting them to ground. Antisymmetric biasing of the endcaps changes the location of the axial potential minimum and is used to move the electron axially in the trap, e.g. to measure the strength of the magnetic bottle. The well-matched 10 MΩ resistors on the endcap lines facilitate this antisymmetric biasing by allowing a single potential V_A to be applied to the "high" leads of each endcap, leaving the "low" leads unconnected. This increases the stability over using two separate voltage sources. We typically source V_A with a battery because the BiasDAC "low" is not truly floating, but only isolated from ground by a 1 Ω resistor.

5.3 Detecting the Axial Motion

The axial frequency of an electron or positron in a Penning trap is generally in the RF range, making it easily accessible in the laboratory. In our case, the axial frequency is ∼200 MHz in the precision trap and ∼53 MHz in the loading trap. The basic detection scheme is as follows. As an electron or positron oscillates along the z-axis in the harmonic electrostatic potential well it induces image charges in the electrodes of the trap. This induced current is proportional to the particle's axial

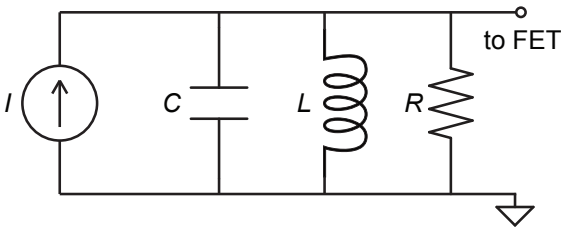

Figure 5.3: Parallel circuit representation of the input to the first stage amplifier. C is the trap capacitance, L is the inductance of the coaxial resonator and R is the effective resistance.

velocity,

$$I = \frac{ec_1}{2z_0}\dot{z}, \tag{5.1}$$

where c_1 is a constant of order unity that depends upon the trap geometry. An inductor is placed in parallel with the trap electrodes to form an LC circuit with the capacitance between nearest electrodes. Losses in this circuit form an effective parallel resistance. This RLC circuit can be seen in Fig. 5.3. The effective resistance is proportional to the axial frequency, the Q of the circuit, and the inductance.

$$R = Q\omega_z L = \frac{Q}{\omega_z C}. \tag{5.2}$$

The induced current passes through this effective resistance and the resulting voltage is amplified and detected. The effective resistance also serves to damp the particle's motion with the damping rate for a single particle given by

$$\gamma_z = \left(\frac{ec_1}{2z_0}\right)^2 \frac{R}{m}. \tag{5.3}$$

We use a commercial high electron mobility transistor[2], a type of field-effect transistor (FET), to amplify the voltage from the particle in the trap. This is an ultra-low noise, high gain amplifier designed to be used between 2 and 18 GHz, dissipating

[2]Fujitsu FHX13LG

180 mW. Because the dilution refrigerator cannot handle nearly that much power, especially at the mixing chamber, we run the amplifier at much lower voltages and use two amplification stages, one right at the pinbase with a typical power dissipation of 100 µW and a second stage amplifier located at the still which we typically run at 250 µW. Additionally, maintaining a low axial temperature requires careful heat-sinking of the transistor. This is accomplished by soldering one of the source leads to the nub of a large silver post that is bolted to one of the tripod legs. In the 2008 trap, the axial temperature cooled to ~ 300 mK in one second when the amplifiers were turned off. Additional details of the amplifier design can be found in [74, ch. 4]. The 200 MHz amplifiers were initially taken from the apparatus used in the 2008 measurement. However, the first stage amp board had to be remade when one of the pads pulled away from the Teflon-glass weave substrate. Additionally, the FETs were swapped out a time or two, the resistors were replaced with new, non-magnetic resistors, and some components were changed to provide better tuning and matching (compare Figure 5.1 to [70, Figure 2.4]).

Due to the high frequency, it is impractical to use a traditional coil as the inductor. Instead we use the distributed inductance of a coaxial line that connects the electrode to the amplifier. This coaxial line is built around a custom vacuum feedthrough into the trap can. The custom feedthrough has an OFE copper outer conductor, a tungsten inner conductor, and a glass-to-metal seal between them. The inner conductor is extended on either side by torch-brazing annealed silver rods to the tungsten. The feedthrough is soft-soldered to a flange that mates with the pinbase. Silver tubing is used to extend the outer conductor. The length of the coaxial line can be adjusted to

set the amplifier resonance frequency. The procedure for assembling the feedthrough is outlined in [74, Appendix B]. It is important to minimize the length of bare wire between the coaxial feedthrough and the electrode in order to minimize the inductance and stray capacitance, so we extended the outer conductor to within $\sim 1/16$" of the electrode. The length of the connection to the top endcap electrode and the length of the extra leads on the top endcap electrode are kept to a minimum in order to minimize stray inductance and capacitance. The first stage amplifier board is enclosed inside a molybdenum box to provide RF shielding and the second stage amplifier is enclosed inside an OFE copper foil box, also to provide shielding. A schematic diagram and board layout as well as a photo of the amplifiers can be see in Fig. 5.4 and Fig. 5.5. Not shown in the figures is the back of each amp board, which serves as a ground plane. This ground plane is cut in half to separate the input and output sides of the board. The two halves are re-joined by a $100\,\Omega$ resistor to minimize resonances that could occur because of this separation.

In the absence of particles, the amplifier circuit is driven by Johnson noise in the resistor,

$$I_N = \sqrt{4k_BTB/R}, \tag{5.4}$$

where k_B is the Boltzmann constant, T is the temperature and B is the measurement bandwidth. The power dissipated in the circuit is then given by $P = I^2\mathrm{Re}(Z)$, where Z is the complex impedance of the parallel RLC circuit. This has the usual Lorentzian lineshape,

$$P \propto \mathrm{Re}(Z) \approx \frac{R(\Gamma/2)^2}{(\Gamma/2)^2 + (\omega - \omega_{LC})^2} \tag{5.5}$$

where $\omega_{LC} = 1/\sqrt{LC}$ and $\Gamma = \omega_{LC}/Q = 1/RC$ is the full-width at half-maximum

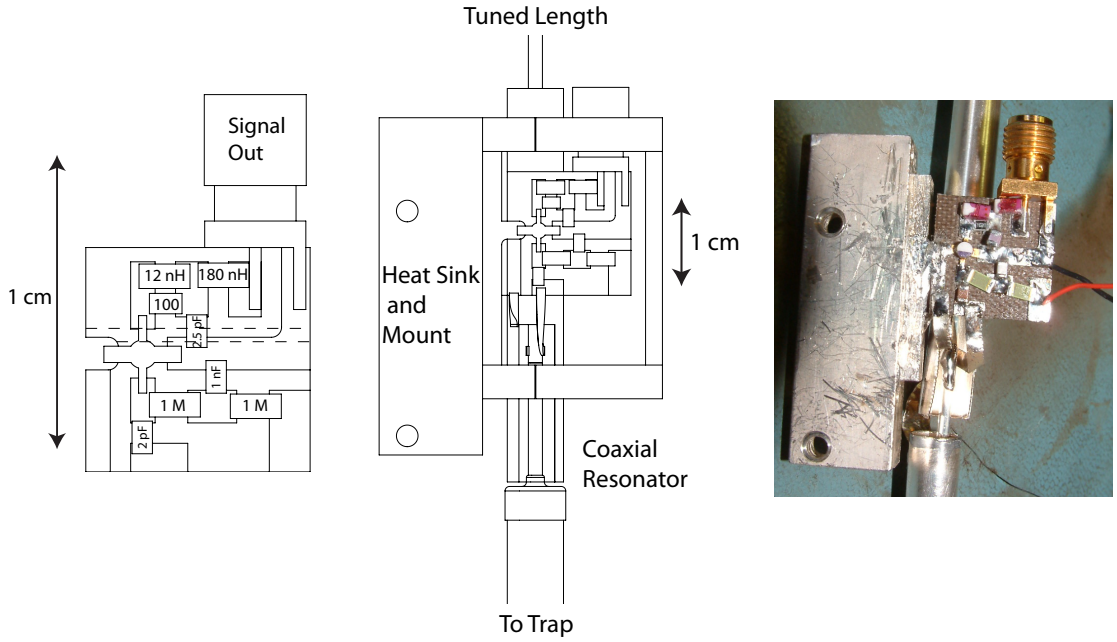

Figure 5.4: Board layout (left), schematic (center) and photo (right) of the precision trap first stage amplifier and coaxial resonator. The dotted lines show the split in the ground plane on the back of the board. Values without units are resistances in ohms.

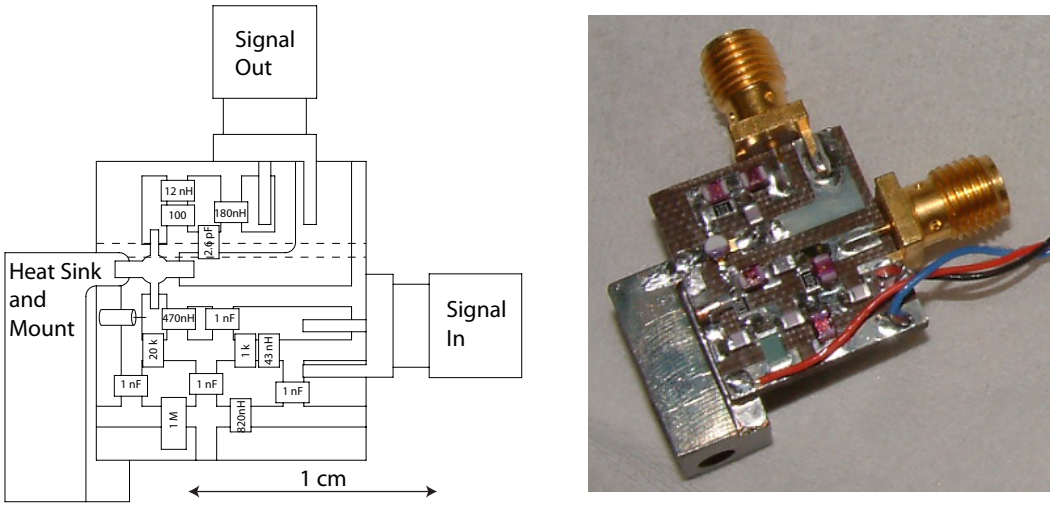

Figure 5.5: Schematic and board layout (left) and photo (right) of the precision trap second stage amplifier. The dotted lines show the split in the ground plane on the back of the board. Values without units are resistances in ohms.

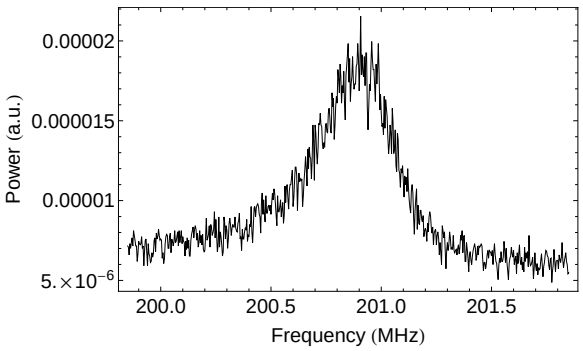

Figure 5.6: A typical noise resonance of the precision trap 1st stage amplifier at 4K. Fitting to Eq. 5.5 gives a Q of 500.

(FWHM). Since the particle signal is the voltage $V = IR$ and the noise signal goes as $\sqrt{R}$ (as seen from Eq. 5.4), the signal-to-noise can be increased by increasing R which, by Eq. 5.2, can be done by increasing Q. A typical amplifier noise resonance can be seen in Fig. 5.6 with a Q of 500.

5.3.1 Dips in the Axial Resonance

When there are particles in the trap, they interact with the tuned circuit and the result is a "dip" in the noise resonance of the amplifier at the axial frequency of the particles. The oscillating particles can be modeled as a series LC circuit in parallel with the amplifier circuit as shown in Fig. 5.7, with values given by [94]

$$\ell = \frac{m}{N}\left(\frac{2z_0}{c_1 e}\right)^2 = \frac{R}{N\gamma_z} \tag{5.6}$$

and

$$c = \frac{N}{\omega_z^2 \ell} \tag{5.7}$$

where N is the number of particles in the trap and γ_z is the single-particle damping width given in Eq. 5.3. With $\omega \approx \omega_{LC}$, the lineshape of the power spectrum is modified

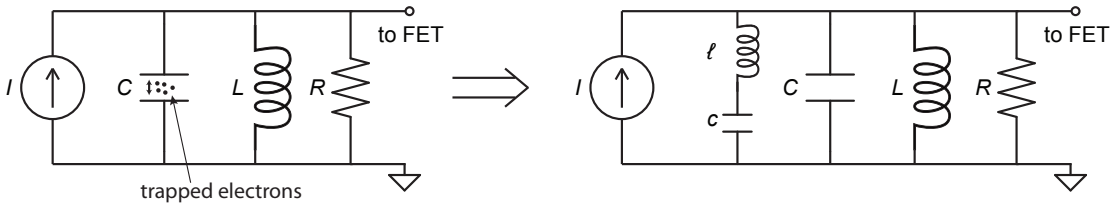

Figure 5.7: Series LC circuit representation of the trapped electrons in the RLC amplifier circuit. C is the trap capacitance, L is the inductance of the coaxial resonator, ℓ and c represent the trapped particles and R is the effective resistance.

to [85]

$$P \propto \frac{\omega_{LC}^4(\omega_z^2-\omega^2)^2}{[(\omega_z^2-\omega^2)(\omega_{LC}^2-\omega^2)-\omega^2\Gamma N\gamma_z]^2+\omega^2\Gamma^2[(\omega_z^2-\omega^2)+\Gamma N\gamma_z]^2}. \tag{5.8}$$

For a small number of particles ($N\gamma_z \ll \Gamma$), and when $\omega_z \approx \omega_{LC}$, Eq. 5.8 results in a Lorentzian "dip" with a FWHM given by $N\gamma_z$ as the particles short out the Johnson noise on resonance. For a large number of particles ($N\gamma_z \gg \Gamma$) the noise resonance splits into two peaks whose separation is given by $\sqrt{N\gamma_z\Gamma}$. Examples of these two limits can be seen in Fig. 5.8. This method is used to quickly detect particles, especially when the exact value of ω_z is unknown (such as when looking for particles in a trap for the first time). It can also be used as a way to count the number of particles in the trap.

5.4 Detecting Cyclotron and Spin Motions

Unlike the axial frequency, the cyclotron and spin flip frequencies in our trap are around 150 GHz — much too high to easily detect, especially for the single quantum transitions that we typically perform. Instead of detecting the motions directly, we

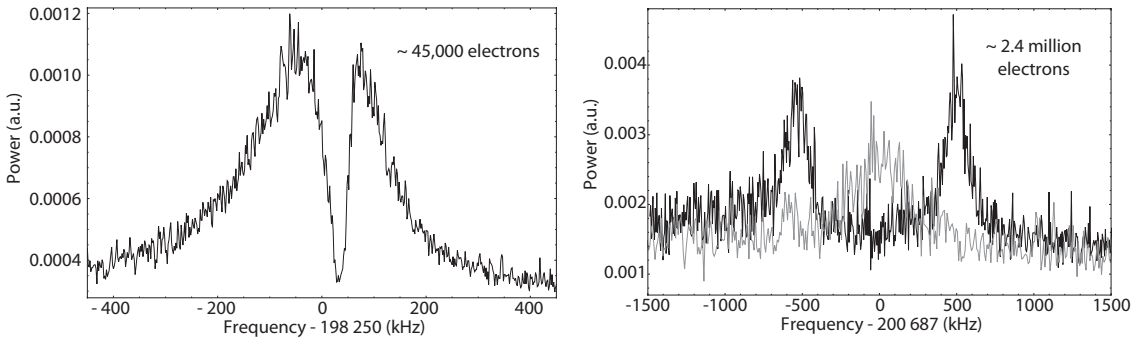

Figure 5.8: Electron dips in the precision trap. $\sim 45,000$ electrons (left) and ~ 2.4 million electron (right). The figure on the right also shows the undistorted amplifier noise resonance in gray for comparison.

use a magnetic bottle (discussed in Section 2.2) to couple the cyclotron and spin flip frequencies to the axial motion, which we can detect.

The presence of the magnetic bottle alters the axial potential, adding a term that is proportional to the strength of the magnetic bottle and the cyclotron and spin states,

$$H' = -\vec{\mu} \cdot \Delta\vec{B}, \tag{5.9}$$

where $\vec{\mu} = (\mu_c + \mu_s + \mu_m)\hat{z}$ and $\Delta\vec{B}$ is defined in Eq. 2.34. In our experiment, the electron is generally near the center of the trap so we can approximate this by setting $\rho = 0$ in Eq. 2.34 so that we get

$$H'_z = 2\mu_B z^2 B_2 \left(n + \frac{1}{2} + \frac{g}{2} m_s\right) \tag{5.10}$$

where we have neglected a small term due to the magnetron motion. This additional term comes into the equation of motion for the axial harmonic oscillator,

$$\ddot{z} + \gamma_z \dot{z} + \left(\omega_{z,0}^2 + \frac{4\mu_B B_2}{m}(n + \frac{1}{2} + \frac{g}{2} m_s)\right) z = 0, \tag{5.11}$$

which modifies the axial frequency to

$$\omega_z^2 = \omega_{z,0}^2 + \frac{4\mu_B B_2}{m}\left(n + \frac{1}{2} + \frac{g}{2}m_s\right). \tag{5.12}$$

This gives a shift of

$$\frac{\Delta\omega_z}{\omega_z} = \frac{2\mu_B B_2(n + \frac{1}{2} + \frac{g}{2}m_s)}{m\omega_{z0}^2}, \tag{5.13}$$

as was mentioned earlier in Section 2.2 (Eq. 2.35).

The modified axial Hamiltonian commutes with both the spin and cyclotron Hamiltonians, making this a quantum non-demolition measurement of the cyclotron and spin transitions. This means that we can make repeated measurements of the cyclotron or spin states via the axial frequency shift without changing the state.

For the 2008 measurement, the magnetic bottle gave an axial frequency shift of 20 ppb, or 4 Hz, for a single cyclotron jump or spin flip. For the smaller magnetic bottle in the current precision trap, the axial frequency shift is 8.5 ppb or 1.7 Hz. Initial trials in the precision trap demonstrate that we can resolve this smaller axial frequency shift with 1 s of averaging time as shown in Fig. 5.9. With better tuning of the self-excited oscillator (described below) it should be possible to cut the averaging time to 0.5 s.

5.5 "Cooling" the Magnetron Motion

Although we shim our magnetic field to maximize the field homogeneity in the trap center and we tune the trapping voltages to minimize inhomogeneities in the electric field, nevertheless inhomogeneities in both the electric and magnetic fields remain. As the particle traverses these inhomogeneities, shifts and broadening of the lines

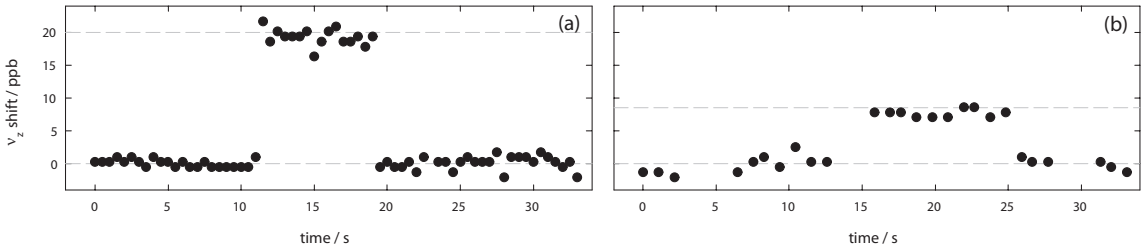

Figure 5.9: A comparison of the axial frequency shift from a cyclotron jump in the 2008 measurement trap (a) and the new precision trap (b). The data in (a) were taken with an 0.5 s averaging time and the data in (b) were taken with a 1.0 s averaging time. The dotted lines indicate the expected axial frequency shift.

can occur. By minimizing the radial and axial extent of the particle's motion we can minimize these effects. The axial motion cools rapidly to the ambient temperature via resistive damping through the tuned circuit that forms part of the amplifier. The cyclotron motion also cools quickly via radiative damping and spontaneous emission. The magnetron motion is intrinsically unstable and thus any dissipation will result in an ever increasing orbit radius until the particle strikes the trap wall. However, since the damping time is so long (see Table 2.2), the magnetron motion is effectively stable. All of the methods for loading particles into the trap leave the particles in an arbitrary (and often quite large) magnetron orbit. Therefore it is necessary to have some way to "cool" the motion, adding energy in order to drive the motion up the repulsive potential well to a smaller radius.

To "cool" the magnetron motion, we rely on the method of 'motional sideband cooling', discussed in detail in [67, Sec. IV]. The magnetron motion is cooled (or heated) by applying an oscillating, inhomogeneous electric field to couple the magnetron motion to the axial motion. This is accomplished by applying a drive at the magnetron sideband of the axial frequency to one half of a split compensation elec-

trode. Applying a drive at the upper sideband, $\nu_z + \nu_m$, takes energy from the axial motion and adds it to the magnetron motion to decrease the radius and 'cool' the motion. The axial motion remains coupled to a thermal bath through the amplifier and thus does not change in temperature. Cooling proceeds until the limit,

$$\frac{T_m}{T_z} = -\frac{\omega_m}{\omega_z}, \tag{5.14}$$

is reached. This limit is equivalent to the thermally averaged quantum numbers being equal. Applying a drive at the lower sideband, $\nu_z - \nu_m$, heats the magnetron motion. We typically cool the particle(s) after loading and again before performing any measurements as noise in the system can cause the magnetron motion to heat with a timescale much shorter than the ideal damping rate.

A similar method can also be used in principle to cool the axial or magnetron motion by coupling to the cyclotron motion, which cools radiatively and at 100 mK is in its ground state. This will be discussed in more detail in Section 7.2.1.

5.6 Driving the Axial Motion

As discussed in Section 5.3, it is possible to detect particles in the trap which are oscillating at their thermal amplitude by observing the dip in the amplifier noise resonance. However, it is often advantageous to drive the axial motion of particles in the trap to a larger amplitude to facilitate easier detection. In particular, it is easier to detect very small numbers of particles when they are driven to a large amplitude. There are two different methods that can be used to drive the axial motion which I will discuss below.

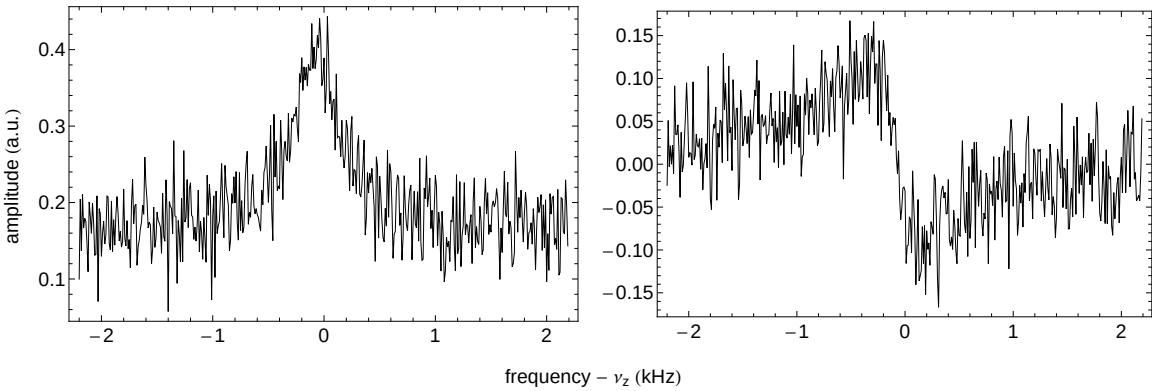

Figure 5.10: In-phase (left) and quadrature (right) driven axial response from a cloud of electrons in the precision trap with $\nu_z \approx 200.7\,\mathrm{MHz}$.

5.6.1 Direct Drives

The most straight-forward way to drive the axial motion is to simply apply a drive near the axial frequency to one of the endcaps and look for the signal. In order to avoid direct feedthrough of the drive into the amplifier, which can swamp the particle signal, we apply not one but two drives, one at $\nu_z - 5\,\mathrm{MHz}$ and one at $5\,\mathrm{MHz}$. The drive at $5\,\mathrm{MHz}$ modulates the trapping potential V_R with the result that the drive applied at $\nu_z - 5\,\mathrm{MHz}$ produces a response at ν_z.

We step the drives across the axial frequency, performing a phase-sensitive detection and observing both the in-phase and quadrature components of the signal. This sweeps out a signal where the in-phase component has a width proportional to the number of particles times the axial damping width γ_z. A diagram depicting this driving scheme can be seen in Fig. 5.11 and a typical driven signal in the precision trap is shown in Fig. 5.10.

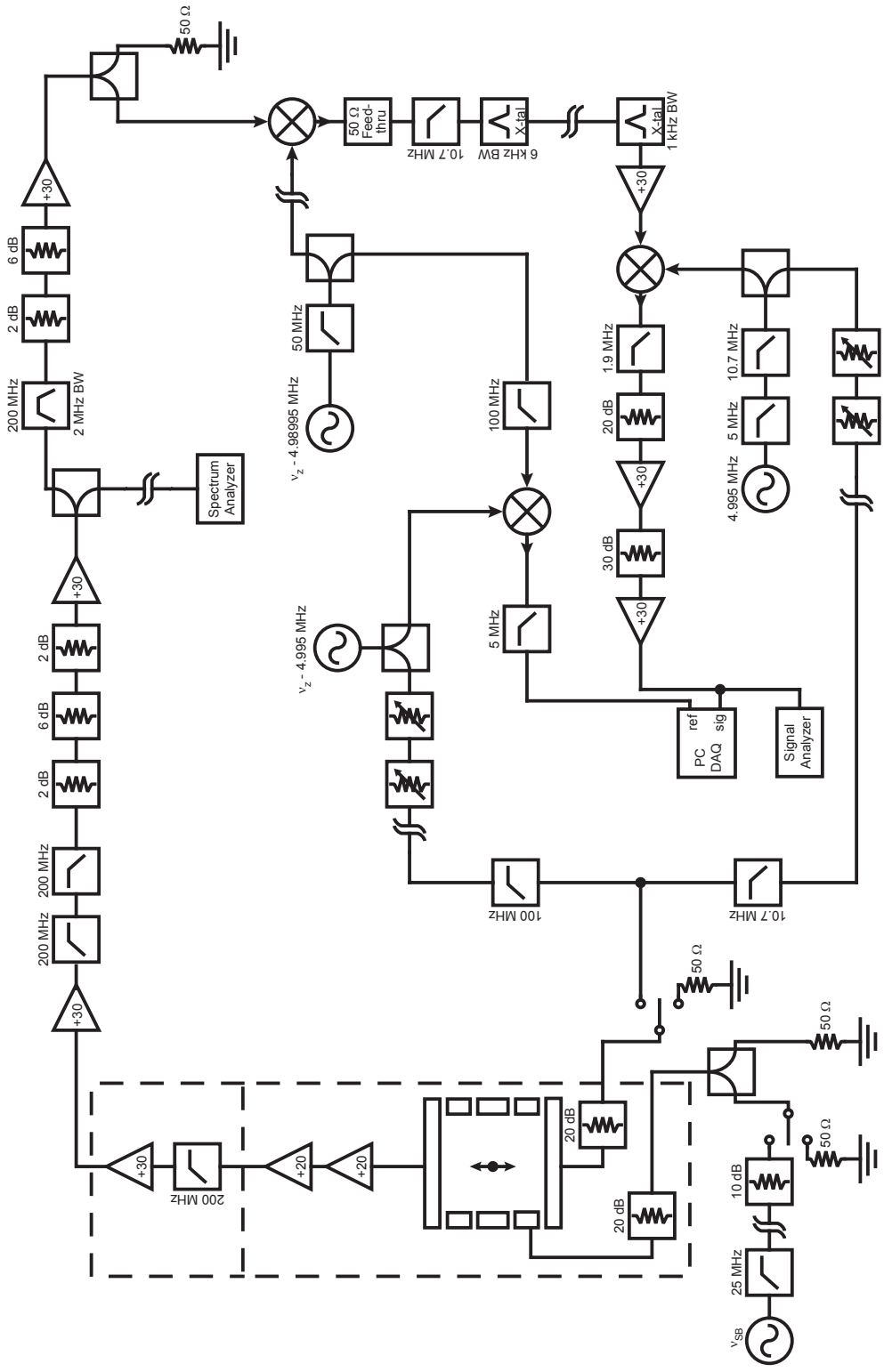

Figure 5.11: RF wiring diagram for driving the axial motion with the direct two-drive scheme.

5.6.2 Anharmonicity Tuning

Driven axial signals are used for initially finding small numbers of particles and for tuning the trap anharmonicities. The axial motion of a particle in a Penning trap is a good example of an anharmonic oscillator. The shape of the in-phase portion of the signal depends on the degree of anharmonicity in the trap, with hysteresis seen when sweeping the drive up and down in frequency across the resonance. Figure 5.12 shows the anharmonic signals seen when the trap is mistuned and when it is fairly well-tuned.

5.6.3 The Self-Excited Oscillator

During the actual measurement, we use a different method to drive the axial motion. In order to reliably detect the small shifts in axial frequency that correspond to a cyclotron transition or a spin flip, it is important that we have a fast, accurate, and reliable method of monitoring the axial frequency. This is accomplished with our self-excited oscillator (SXO), which uses the signal from the particle as the drive. This system is described in detail elsewhere [95, 74, 70] so I will only give a brief overview. As discussed in Section 5.3, the axial motion of a particle induces a voltage, proportional to the particle's velocity, across a tuned circuit. The energy dissipated in this tuned circuit damps the particle's motion with a rate γ_z. To counteract the damping, we can apply an axial drive to the particle. By using a portion of the particle's own signal as the drive, we ensure that the drive always remains on resonance. We use an amplitude-dependent gain that we adjust continuously in real time to perfectly cancel the axial damping and drive the particle to a large stable axial

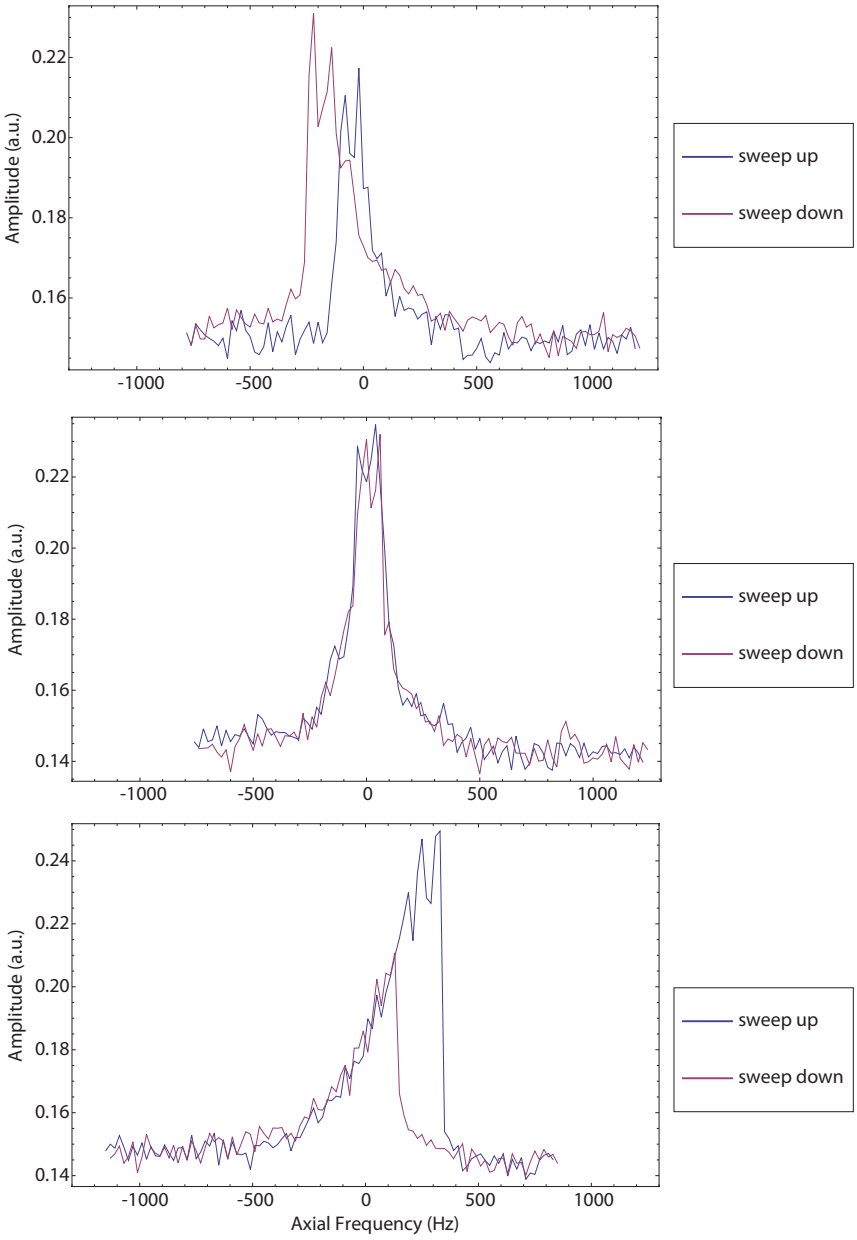

Figure 5.12: Example of anharmonicity tuning in the precision trap, with the compensation potential adjusted such that (a) $C_4 < 0$, (b) $C_4 \approx 0$, and (c) $C_4 > 0$.

amplitude. A digital signal processor is used to calculate a running Fourier transform of the signal and adjust the gain as a function of the amplitude to maintain a stable signal. We can lock the axial frequency by charge-pumping the capacitor on the ring line to make small changes in the ring voltage. When the SXO is well-tuned, we can easily resolve the axial frequency to better than one Hz with a half-second of averaging time. This is more than enough to detect single quantum transitions even with our new smaller magnetic bottle. Details of the RF wiring, including the SXO can be seen in Fig. 5.13. This set-up is largely unchanged from the 2008 measurement.

5.7 Driving Cyclotron Transitions

The cyclotron and spin flip frequencies are both in the microwave regime, around 150 GHz, so driving them requires a different technique. We use an Agilent E8251A Performance Signal Generator (PSG) to generate microwaves at around 15 GHz. This PSG has a low-phase-noise, 10 MHz oven-controlled crystal oscillator that we use as the timebase for all frequencies in the experiment. The 15 GHz signal from the PSG gets transmitted to a custom microwave multiplier through a special low-loss cable. The microwave multiplier uses an impact ionization avalanche transit-time (IMPATT) diode to multiply the frequency by a factor of 10 and output a drive near 150 GHz with 2 mW of power. Although only a small amount of power is needed to drive single cyclotron transitions, the high power is to enable axial sideband cooling which requires significantly more power. Pairs of voltage-controlled attenuators in the multiplier are used to set the strength of the drive. The 150 GHz microwaves are emitted from the multiplier via a waveguide with a horn on the end. In the apparatus used in the 2008

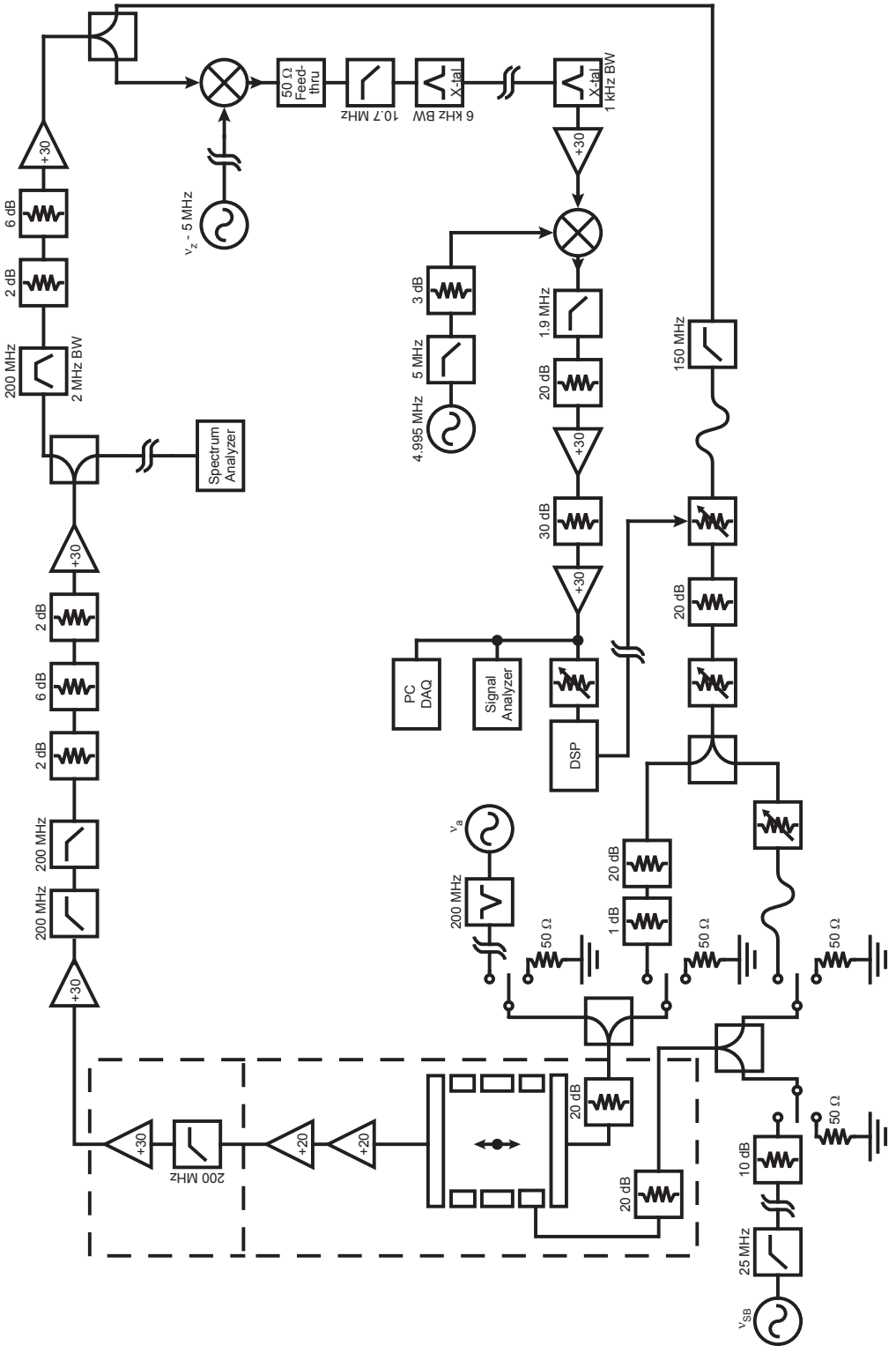

Figure 5.13: RF wiring diagram for the self-excited oscillator.

measurement, the microwave multiplier was mounted below the magnet dewar and the microwaves were broadcast up from the bottom into the trap can. In the new apparatus, the microwaves must enter the dilution refrigerator from the top. This involves a more complicated path through the dilution refrigerator before reaching the trap can, which is described below. Additionally, the microwave multiplier must be moved out of the way when the fridge is being inserted or removed from the dewar. This was accomplished by mounting the microwave multiplier on a hinged post. When the fridge is being raised or lowered, the multiplier can be swung out of the way. When the fridge is cold, the microwave multiplier can be swung into position with the horn directly over a Teflon vacuum window and locked into place.

As the microwaves exit the horn on the multiplier, they pass through a Teflon vacuum window at the hat into the inner vacuum chamber of the dilution refrigerator. They travel through a series of waveguides and horns to go from the 300 K region to the 4 K region. This design, which can be seen in Fig. 5.14, is used to minimize room temperature radiation that is broadcast to 4K and below. Once at the 4K plate of the dilution refrigerator, the microwaves are broadcast from a horn into the IVC where they pass through two Teflon lenses, one located at the still and one at the intermediate cold plate, which focus the microwaves and direct them through the set of 1-inch clear shot holes down the fridge to a horn at the mixing chamber. In addition to steering the path of the microwaves, these lenses also serve as cold attenuators to prevent room temperature and 4 K radiation from reaching the mixing chamber. From the mixing chamber horn the microwaves enter a waveguide which takes them to a sapphire window into the trap vacuum enclosure where they go

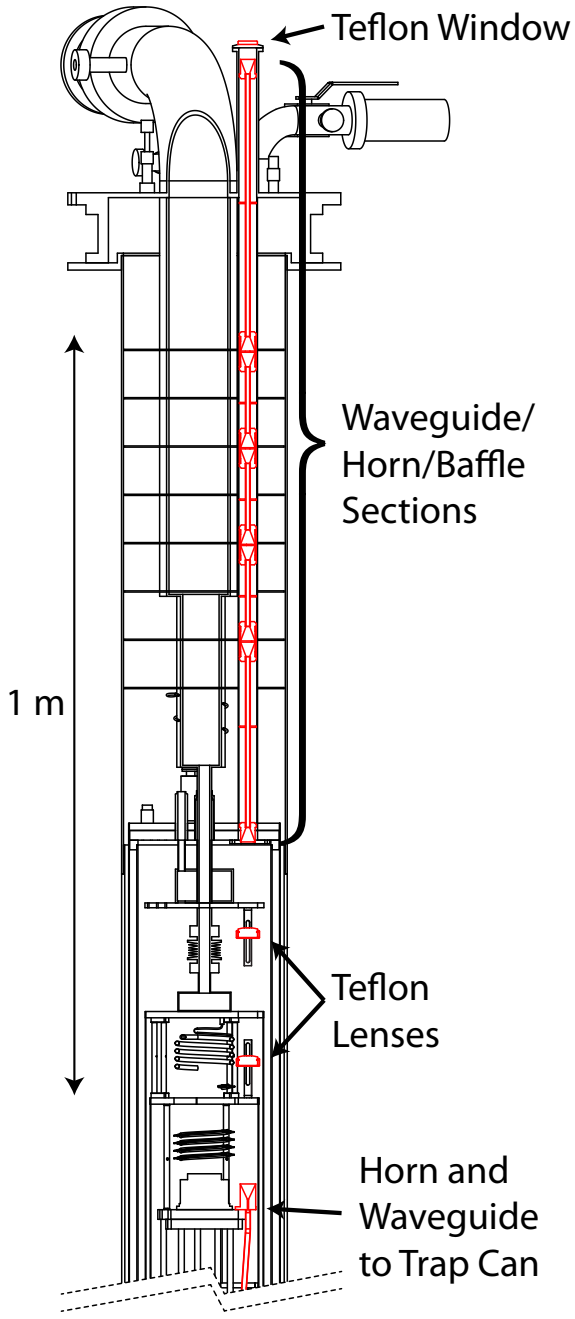

Figure 5.14: The microwave path from the top of the dilution refrigerator (300 K) to the horn at the mixing chamber (100 mK) is shown in red.

through another section of waveguide before being injected through a very small slit into the precision trap cavity. The design from 300 K to the horn at the mixing chamber (100 mK) is shown in Fig. 5.14 and details of the entire set-up can be seen schematically in Fig. 5.15. We have measured approximately 40 dB of attenuation between the microwave multiplier horn and the horn at the mixing chamber. The amount of power that actually makes it into the trap cavity is difficult to quantify and depends upon the proximity of the microwave frequency to cavity modes in the trap.

5.7.1 Cyclotron Measurement Procedure

The following is a typical procedure for measuring a single cyclotron transition attempt. We always start in state $|0,\uparrow\rangle_{\text{electron}}$ or $|0,\downarrow\rangle_{\text{positron}}$.

1. Turn the self-excited oscillator off and the magnetron cooling drive on. Wait 0.5 s.

2. Turn the amplifiers off. Wait 1.0 s.

3. Turn the magnetron cooling drive off. Wait 1.0 s.

4. Apply a cyclotron drive near $\bar{\nu}_c$ and a detuned anomaly drive for 2.0 s.

5. Turn the amplifiers and self-excited oscialltor back on. Wait 1.0 s for the SXO to stabilize.

6. Trigger the computer data-acquisition card (DAQ).

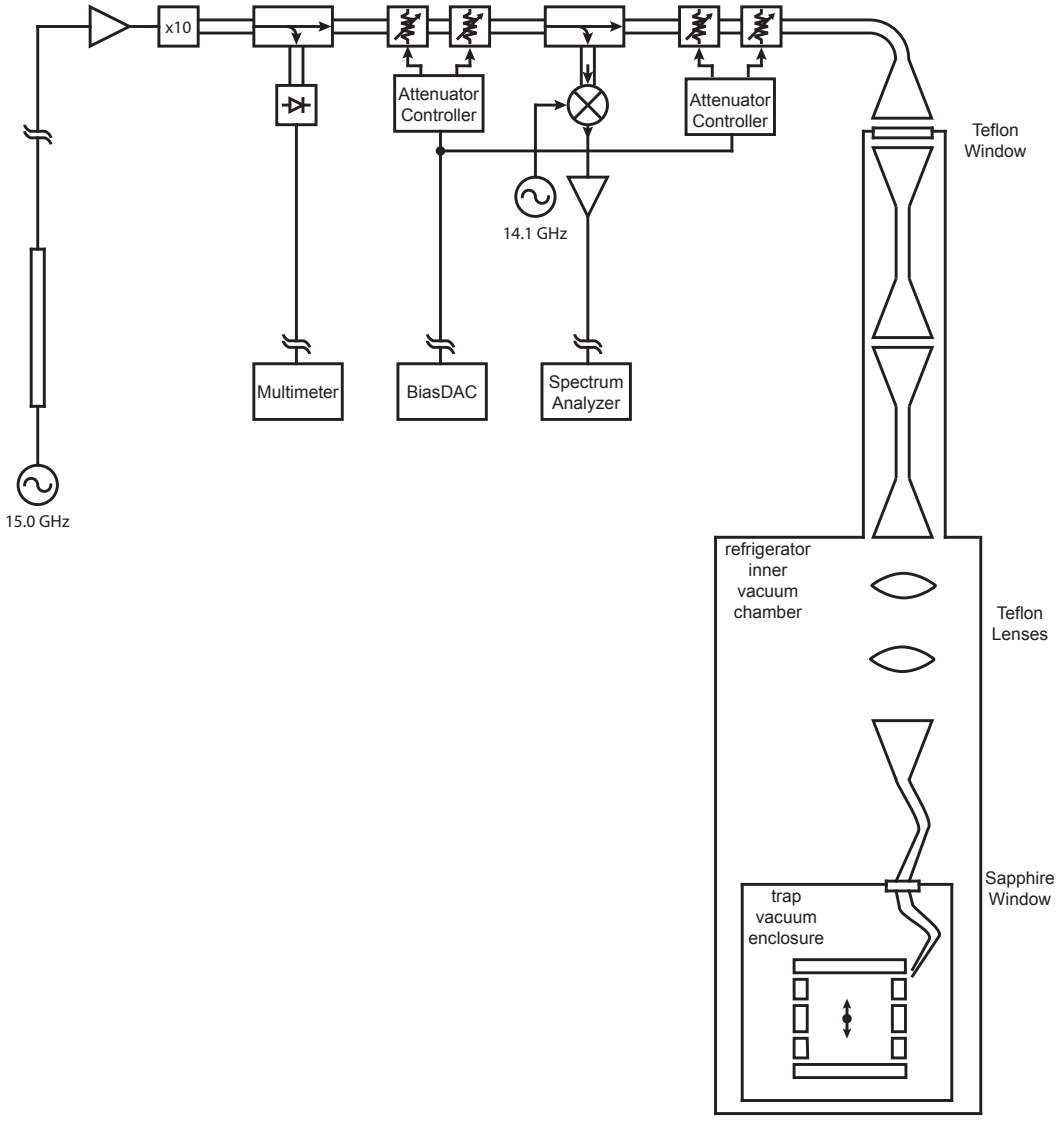

Figure 5.15: Schematic diagram of the microwave system. Single lines represent cables and double lines represent waveguides. Long runs between the experiment and the electronics rack are indicated by a break.

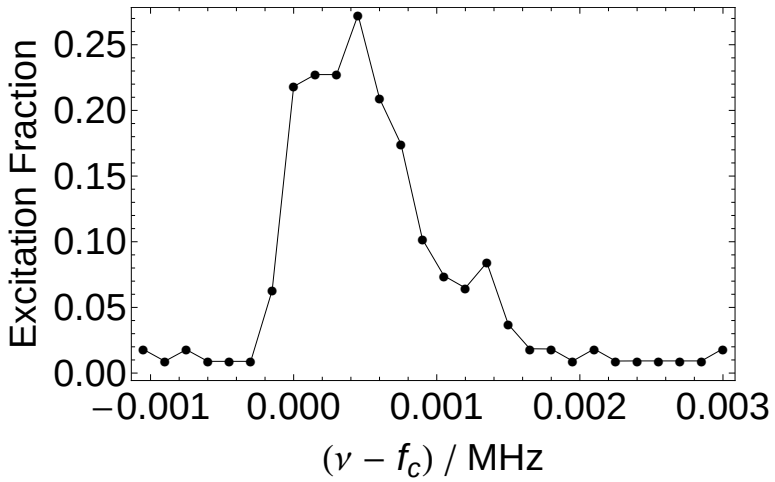

Figure 5.16: Cyclotron lineshape in the new precision trap taken with the self-excited oscillator off but the amplifiers on.

Once the DAQ has been triggered, it reads continuously and a LabVIEW program Fourier transforms the data in chunks, whose length can be adjusted and is typically between 0.25 s and 1.0 s. If a cyclotron transition has been made, the program declares a successful excitation and waits for a decay back to $|0,\uparrow\rangle_{\text{electron}}$ ($|0,\downarrow\rangle_{\text{positron}}$). Then the cyclotron frequency is stepped to the next value and the process is repeated. The entire procedure is automated.

While the procedure given above is used for the g-value measurement, it is not necessary to turn the amplifiers or the SXO off in order to drive cyclotron transitions. The driven cyclotron lineshape (taken with the amplifiers off but the SXO on while the cyclotron drive is applied) is used in the single-particle cavity mode mapping described below (Section 7.1.2). A cyclotron lineshape taken with the SXO off but the amplifiers on will be broadened due to the higher axial temperature and can be used as a probe to determine the axial temperature when the amplifiers are on. The preliminary cyclotron lines we have measured in the new precision trap, such as the

one shown in Fig. 5.16, were all taken with the SXO off but the amplifiers on.

5.8 Driving Anomaly Transitions

There are two ways that have been used in g-value experiments to drive an anomaly transition, both of which involve driving the particle in an oscillating transverse magnetic field. The first method, which we do not use, involves splitting both compensation electrodes to form two effective current loops. A drive is applied to each loop at the anomaly drive frequency, with the current flowing in the opposite direction in each loop. This creates an oscillating transverse magnetic field near the trap center. When the drive frequency equals the anomaly frequency, there is a probability of making an anomaly transition. This method was used in the 1987 University of Washington g-value measurement [11].

While we have split our compensation electrodes in order to cool the magnetron motion (see Section 5.5), we choose to use a different method to drive anomaly transitions that depends on the presence of the magnetic bottle. The magnetic bottle creates a $z\rho\hat{\rho}$ gradient near the trap center. We apply a drive near the anomaly frequency to the bottom endcap electrode to drive the electron axially through this magnetic field gradient. This creates the requisite oscillating transverse magnetic field. As discussed in [74, section 2.3.3], the power required to drive an anomaly transition in this fashion depends upon the proximity of the axial and anomaly frequencies. The closer the axial frequency is to the anomaly frequency, the less power is required to drive an anomaly transition. With $\nu_z \sim 200\,\mathrm{MHz}$ and $\nu_a \sim 170\,\mathrm{MHz}$, we can drive anomaly transitions with low enough power to minimize systematic er-

ror in the g-value measurement and still prevent spurious anomaly transitions from occurring while driving the axial motion.

5.8.1 Anomaly Measurement Procedure

The typical procedure for measuring a single anomaly transition attempt is quite similar to the cyclotron procedure and is given below. Again, we always start in state $|0,\uparrow\rangle_{\text{electron}}$ or $|0,\downarrow\rangle_{\text{positron}}$.

1. Turn the self-excited oscillator off and the magnetron cooling drive on. Wait 0.5 s.
2. Turn the amplifiers off. Wait 1.0 s.
3. Turn the magnetron cooling drive off. Wait 1.0 s.
4. Apply an anomaly drive near $\bar{\nu}_a$ and a detuned cyclotron drive for 2.0 s.
5. Turn the amplifiers and self-excited oscialltor back on. Wait 1.0 s for the SXO to stabilize.
6. Trigger the computer data-acquisition card (DAQ).

The LabVIEW program looks to see if a transition has been made in the same way as for a cyclotron transition. The difference is that we cannot detect the frequency shift from a $|0,\uparrow\rangle_{\text{electron}} \rightarrow |1,\downarrow\rangle_{\text{electron}}$ anomaly transition and so we have to wait several cyclotron lifetimes to look for a spontaneous decay to $|0,\downarrow\rangle_{\text{electron}}$. If there is no decay after several cyclotron lifetimes, the attempt is deemed a failure and the sequence is repeated at the next anomaly frequency step. If there is a decay, the attempt is

declared a success and then resonant cyclotron and anomaly drives are applied to pump the electron back to the $|0,\uparrow\rangle_{\text{electron}}$ state before continuing on. As with the cyclotron transition, the entire procedure is automated. Anomaly transitions have not yet been performed in the new precision trap.

5.9 Directly Driven Spin Flips

In addition to flipping the particle spin by applying a drive at the anomaly frequency as discussed above, it is also possible to drive spin flips directly by applying a drive at the spin flip frequency. Recall that in our apparatus, the spin-flip frequency is approximately 150.2 GHz, so this is a microwave drive just like the cyclotron drive. It takes significant power to drive a spin flip transition - much more than for a single cyclotron jump. For both a cyclotron transition and a spin-flip transition, the probability of making a transition is proportional to the Rabi frequency. Of course the Rabi frequency depends on the drive strength. However, for a given drive strength, the spin-flip Rabi frequency, Ω_s is over four orders of magnitude smaller than the cyclotron Rabi frequency, Ω_c. In addition to turning up the microwave drive power, we can use the cavity mode structure to our advantage. As the drive frequency approaches a cavity mode frequency, the amount of power that is coupled into the cavity increases substantially. Additionally, the "cooling" modes have the right sort of geometry to drive a spin flip. The maximum benefit can gained from tuning the magnetic field such that the cyclotron frequency is approximately 174 MHz below the center of a cooling mode so that the spin frequency, ν_s is on resonance.

The first directly driven spin-flip line in a Penning trap, performed in the 2008

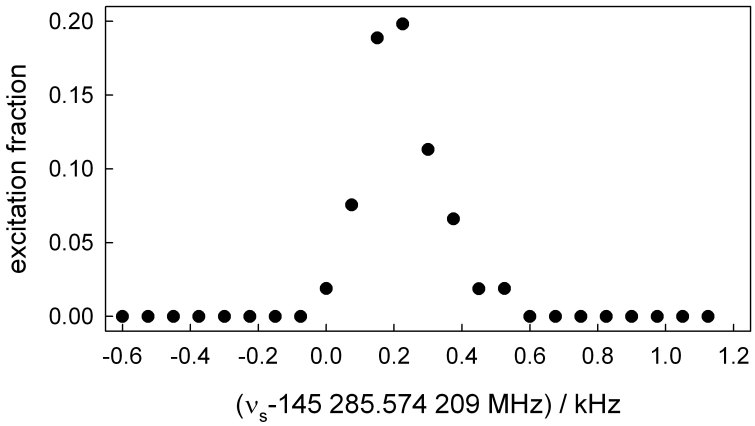

Figure 5.17: Lineshape of a directly driven spin flip.

measurement apparatus, is shown in Fig. 5.17. Because the cooling mode we were using has a cyclotron coupling mode just below it in frequency, we tuned the cyclotron frequency to be $\bar{\nu}_c \approx \nu_{\mathrm{M}} - 1174\,\mathrm{GHz}$, slightly lower than optimal for maximizing spin flip power. This measurement was performed partly as a proof-of-principle measurement for using an electron in a Penning trap as a qubit. An attempt was made to drive coherent spin flips and observe the Rabi oscillations. However, none were observed, indicating we did not have enough microwave power. As mentioned earlier, the presence of the magnetic bottle causes the spin frequency to depend on the axial position. Thermal fluctuations in the axial motion will destroy the coherence of the spin flip rotation. Therefore, in order to drive coherent spin flips, Ω_s must be fast compared to the decoherence time. In this case, the decoherence time is given by the bottle-broadened linewidth, as defined in Eq. 2.36. For typical experimental parameters, this gives $\Delta\omega_s \approx 125\,\mathrm{Hz}$. Because the new precision trap has cooling modes which are far from cyclotron coupling modes, it should be possible to tune the spin frequency to be perfectly aligned with one of the cooling modes to allow even

more power to be coupled into the cavity. If this is still not enough power to drive coherent spin flips, another possibility would be to decouple the axial motion from the amplifier. This of course has its own set of challenges.

Chapter 6

Positrons and Electrons in the Loading Trap

The loading trap was installed in order to facilitate the accumulation of positrons at an acceptable rate using the smallest possible source (Section 4.3). This chapter describes techniques for loading positrons and electrons into the loading trap and detecting and interacting with the loaded particles. These techniques are used to characterize the loading mechanism, confirming that positrons are loaded via field ionization of Rydberg positronium with a similar relative loading rate as in previous experiments which used a much larger source [84].

6.1 Loading Electrons with the FEP

The field emission point used to load electrons into the precision trap as described in Section 5.1 is also used to quickly and easily load electrons into the loading trap.

Not all of the electrons from the FEP strike the top endcap of the precision trap. Up to 60-90% of them pass through another small (.01" diameter) hole in the precision trap top endcap and go on to strike the transmission moderator at the top of the loading trap stack. Loading of varying numbers of electrons proceeds as in the precision trap.

This method of loading was particularly useful in initially finding particles in the loading trap. Once we could easily find electrons loaded from the FEP, we moved on to loading electrons and positrons from the positron source as described in the next section.

6.2 Loading Particles from the Source

A major improvement to this new apparatus over the apparatus used in the 2008 measurement was the addition of a ^{22}Na source for positron loading. The positron source and loading trap were designed to use the positron loading method developed in the ATRAP collaboration for antihydrogen studies [84], discussed in detail in Section 4.1. This method involves field ionization of positronium, giving us the ability to load both electrons and positrons from the ^{22}Na source. The first step in loading either positrons or electrons is to lower the source down into the loading position at the pinbase from the storage position at the mixing chamber. Appropriate loading voltages are then applied to the electrodes of the loading trap as discussed below. After loading is complete, the source is returned to the storage location so that additional positrons or gammas from the source do not interfere with our measurements.

While the ultimate goal is loading positrons, it is easier to begin by loading electrons from the source. This is because the trap could be characterized using electrons

from the FEP to get a good sense for the axial frequency and the necessary magnetron cooling procedure. We could then dump the trap and begin loading from the source, knowing right where the electrons should be and how to cool them.

In principle, one can just reverse the potentials on the electrodes and find positrons in the exact same location. In practice this is not the case. For a given voltage configuration, the axial frequency for electrons differs from that for positrons by about 400 kHz. To put this another way, in order to line up the axial signal from a cloud of electrons and a cloud of positrons in the same location on the amplifier noise resonance (at the same axial frequency) requires a ring voltage offset of ~ 140 mV. A similar phenomenon has been observed in the proton/antiproton magnetic moment experiment when loading electrons, protons, and antiprotons into the same trap [96].

As discussed in Section 4.1, the method we use to load positrons from the source involves formation of Rydberg positronium at the moderator surface followed by field ionization of the positronium. In order for the positron (or electron) to end up in the trap, the electric field must be large enough inside the trapping well in order to ionize the positronium within the trapping well so either the positron or electron can remain trapped. Additionally, the electric field between the moderator and the trapping well must be small enough so as not to prematurely ionize the positronium. There are many possible electrode potential configurations to achieve this. One such configuration is shown in Fig. 6.1. A detailed loading analysis will be presented in Section 6.5.

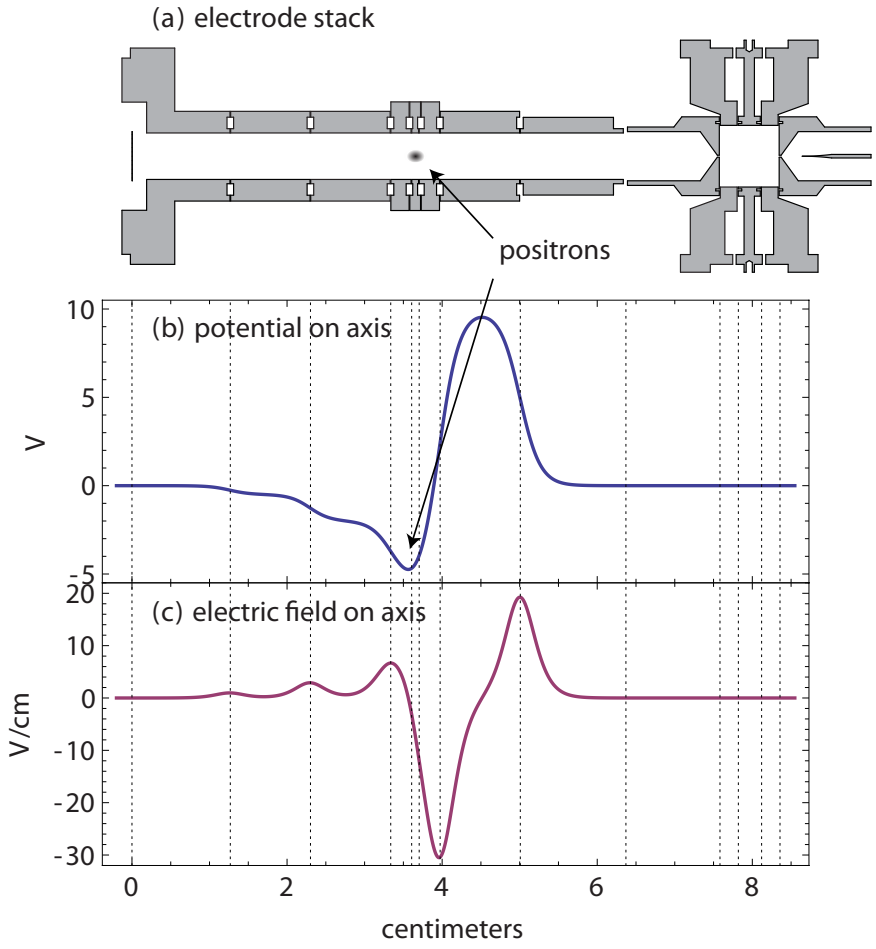

Figure 6.1: A typical trapping potential and electric field configuration used for loading positrons in the loading trap

6.3 Biasing the Electrodes

The loading trap circuitry is quite similar to the precision trap circuitry, and the same care has been taken to eliminate noise as described in Section 5.2. The DC bias lines have the same type of RC and LC filtering from room temperature to base temperature and the RF lines have the same 20 dB cold attenuators at the 1K pot and capacitive dividers at the pinbase. The loading trap ring voltage is supplied by a Fluke 5440B voltage calibrator which has a nominal stability of 300 ppb over 24 hours. As in the precision trap, the Fluke is used to charge a 10 μF capacitor at the pinbase to provide short-term stability for the ring voltage. The loading ring line has a 1 MΩ resistor at the pinbase to form an RC circuit with a 10 s time constant. A 100 MΩ resistor can also be added at room temperature as in the precision trap, although it is generally not used since dumping, loading, trapping and transferring involve a number of large voltage changes and the additional stability is not generally necessary. The ring voltage locking methods used in the precision trap are also unnecessary. The endcaps have matched 10 MΩ resistors to ground, largely for stability as we don't currently have plans to use them for biasing as we do in the precision trap. The compensation voltage used for trapping as well as voltages applied to all other electrodes in the stack and the moderator are supplied by a DecaDAC[1]. The wiring diagram for the positron loading trap can be seen in Figure 6.2. Additional details of the RF wiring are discussed in Section 6.4 and details of the loading trap amplifiers can also be found in Section 6.4.1. Additional details of the loading trap design are discussed in Chapter 4.

[1]Multi-channel digital to analog converter built in-house at the Harvard Electronic Instrument Design Lab, with a range of ±10 V (similar to the BiasDACs used in the precision trap).

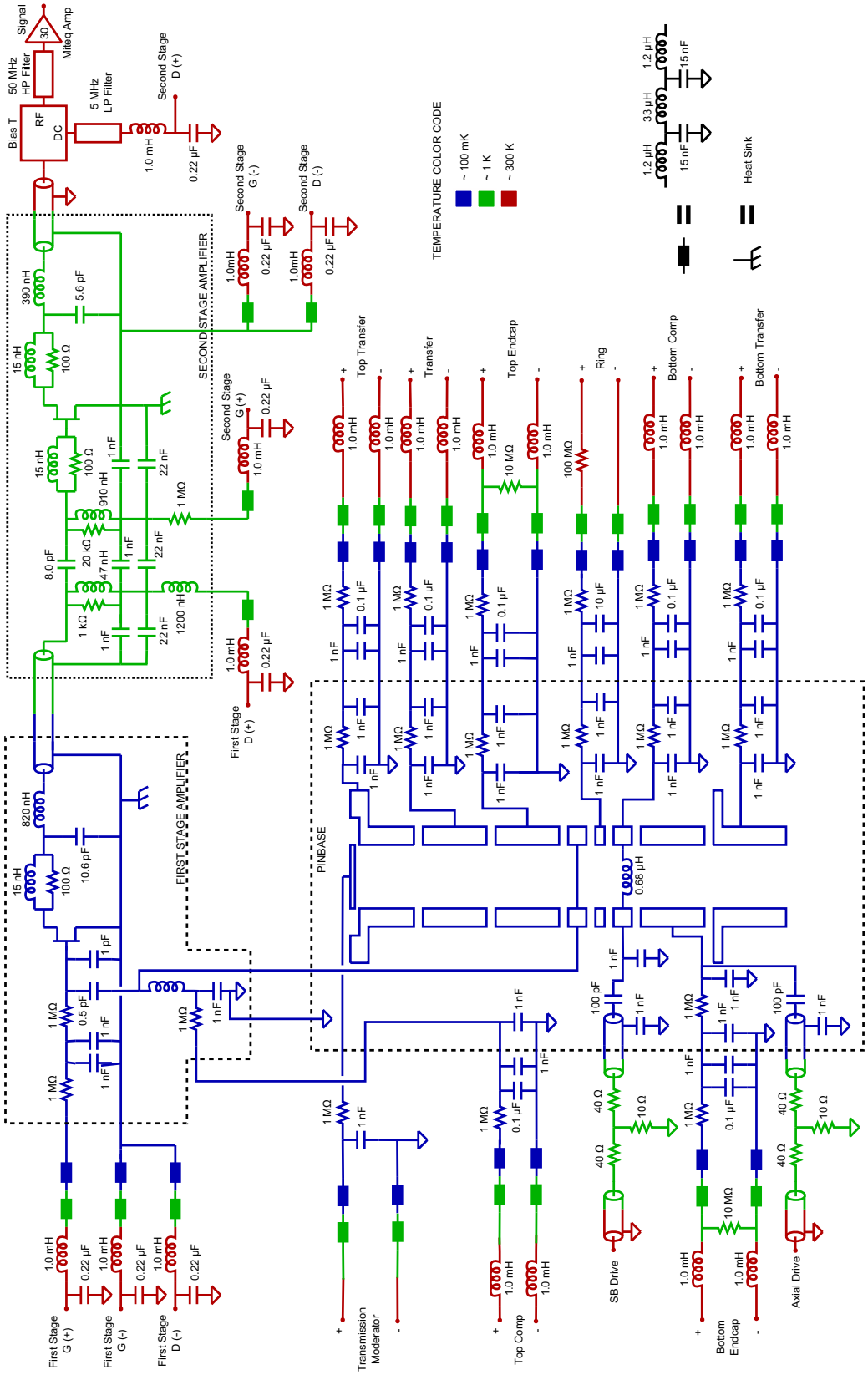

Figure 6.2: Loading trap electrode wiring diagram

6.4 Detecting and Driving Particles in the Loading Trap

The loading trap was built to accumulate positrons from the source at a reasonable rate. It does not need all of the features in the precision trap that are used in the g-value measurement such as a microwave inlet for driving cyclotron transitions or a magnetic bottle for detecting cyclotron transitions. However, it is necessary to detect the presence of positrons or electrons in the loading trap, both for characterization of the loading mechanism and for transferring to the precision trap. Therefore the loading trap has an axial detection and driving scheme that is similar to that used in the precision trap and it also includes a magnetron cooling drive. These features will be discussed below.

6.4.1 Detecting the Axial Motion

As in the precision trap (see Section 5.3), the axial oscillation is the easiest motion to detect in the loading trap. In fact, it is the only motion that we can detect due to the lack of magnetic bottle for detection of the cyclotron and spin motions (see Section 5.4). Because the considerations that went into the choice of 200 MHz for the axial frequency in the precision trap (such as proximity to the anomaly frequency) are unnecessary in the loading trap, we opted to instead work at $\sim$53 MHz. This frequency allows a voltage of less than $\pm$10 V to be applied to the trap electrodes, and amplifiers are easier to construct at these lower frequencies.

The positron loading trap has its own set of amplifiers. These amplifiers are based

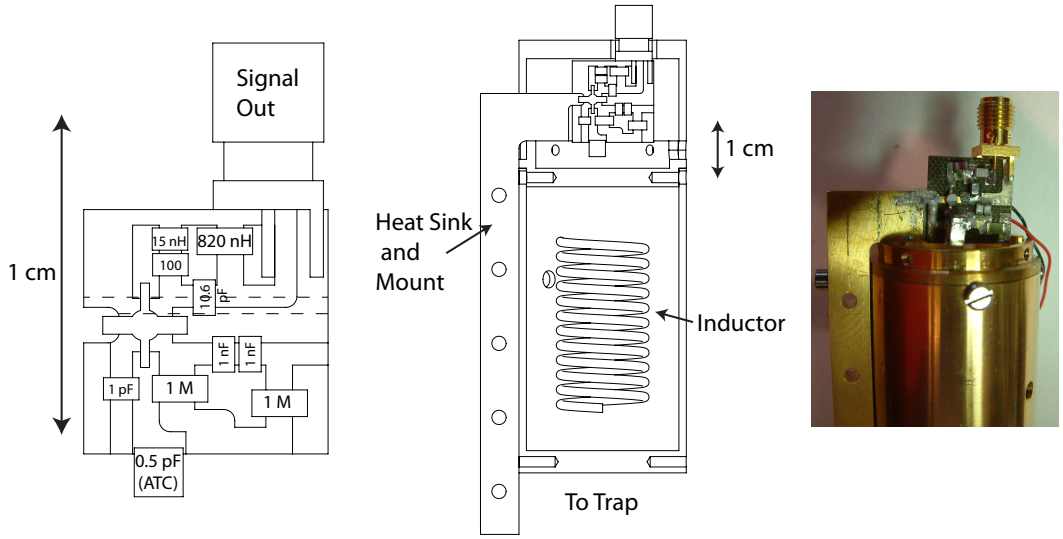

Figure 6.3: Loading trap first stage amplifier layout and photo. The dotted lines show the split in the ground plane on the back of the board. Values without units are resistances in Ω.

on the 60 MHz amplifiers described in detail in [74, Chapter 4] and also used for the planar trap [65]. The design was modified to give an axial frequency of ∼53 MHz. The amplifier schematics can be seen in Figure 6.2 and the amp board layouts can be seen in Figures 6.3 and 6.4. As in the precision trap amplifiers, the ground plane on the back of the boards (not shown) is split to separate the input and output sides of the board and the two halves are joined by a 100 Ω resistor. Because the axial frequency is lower, we use a helical resonator for the inductor, instead of the coaxial resonator used in the precision trap. The inductor for the first stage amplifier was wound from silver-plated copper wire. It can be seen schematically in Figure 6.3. In order to maximize the Q, and thus the signal-to-noise, the first stage amp can was made as large as possible without interfering with the positron source or other amplifiers and wiring already in the pinbase/tripod region [97].

The amplifier is connected to the upper compensation electrode (rather than the

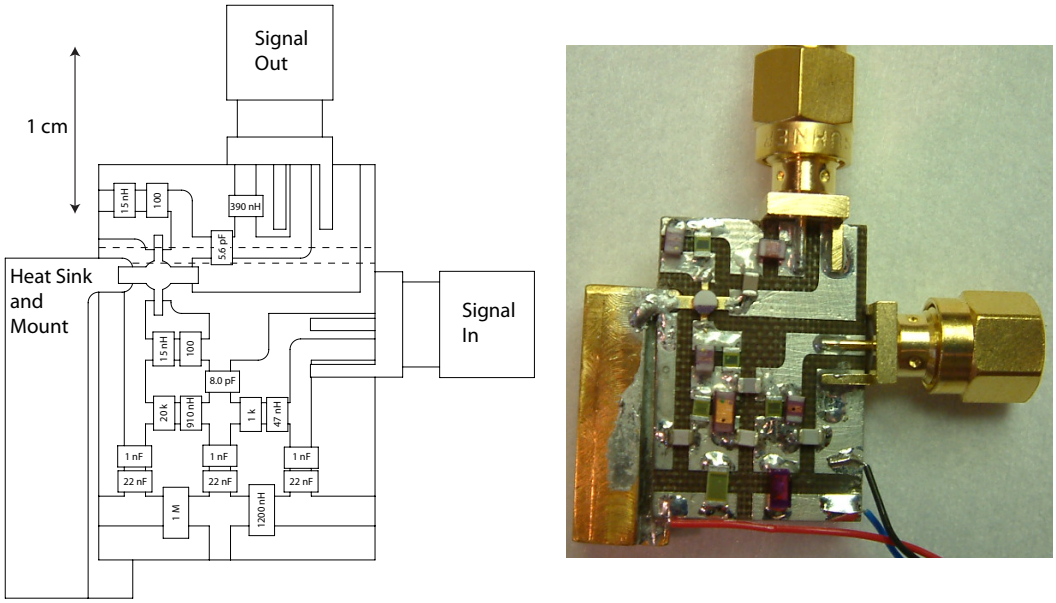

Figure 6.4: Loading trap second stage amplifier layout and photo. The dotted lines show the split in the ground plane on the back of the board. Values without units are resistances in Ω.

top endcap electrode) to increase the axial damping rate. As shown in Eq. 5.3, the damping width depends upon the constant c_1 which in turn depends upon geometry. For a closed-endcap trap, whose endcaps approximate an infinite parallel-plate capacitor, c_1 is nearly unity. For the open-endcap trap, c_1 is larger for a compensation electrode than for an endcap. Both compensation electrodes are split but since we do not require the split for the upper one we can short the two halves together and use the full electrode for detection. A typical loading trap amplifier noise resonance can be seen in Fig. 6.5.

6.4.2 Dips in the Axial Resonance

The same equivalent circuit analysis described in Section 5.3 and Section 5.3.1 is used to describe the loading trap amplifiers. Dips in the axial noise resonance are

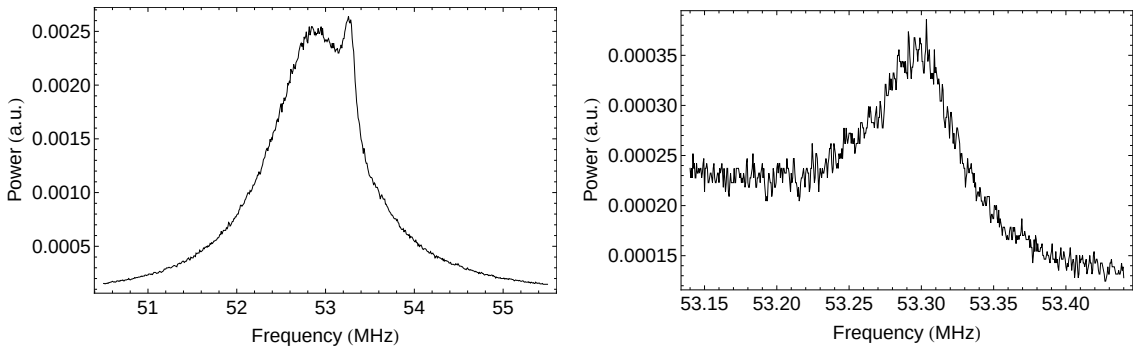

Figure 6.5: Typical loading trap amplifier noise resonances taken at 4K, showing the first stage on top of the second stage (left) and just the first stage (right). The first stage fits to $Q \approx 800$.

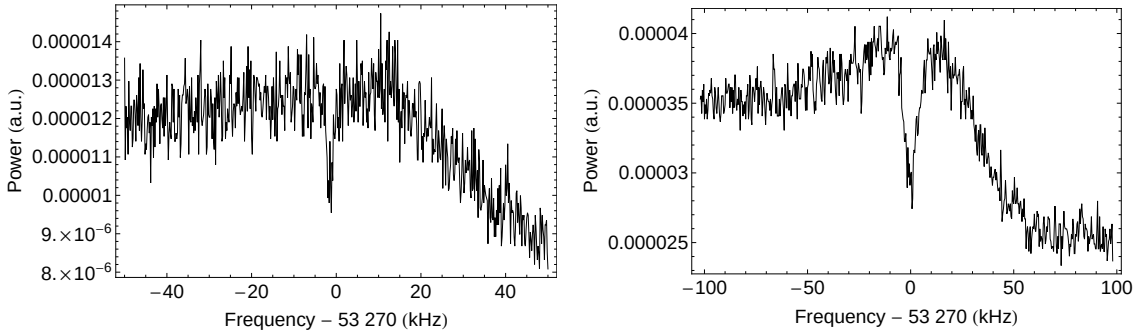

Figure 6.6: Typical dips in the loading trap. A small cloud of positrons (left) and a larger cloud of electrons (right).

the simplest signature of electrons or positrons in the loading trap also. Some typical electron and positron dips can be seen in Fig. 6.6.

6.4.3 Driving the Axial Motion

As in the precision trap, moderately-sized clouds can easily be seen by observing the dip in the amplifier noise resonance while smaller clouds are more easily detected by driving the axial motion. In the loading trap, we use a direct drive similar to that described in Section 5.6.1 for the precision trap. The drive, consisting of two separate

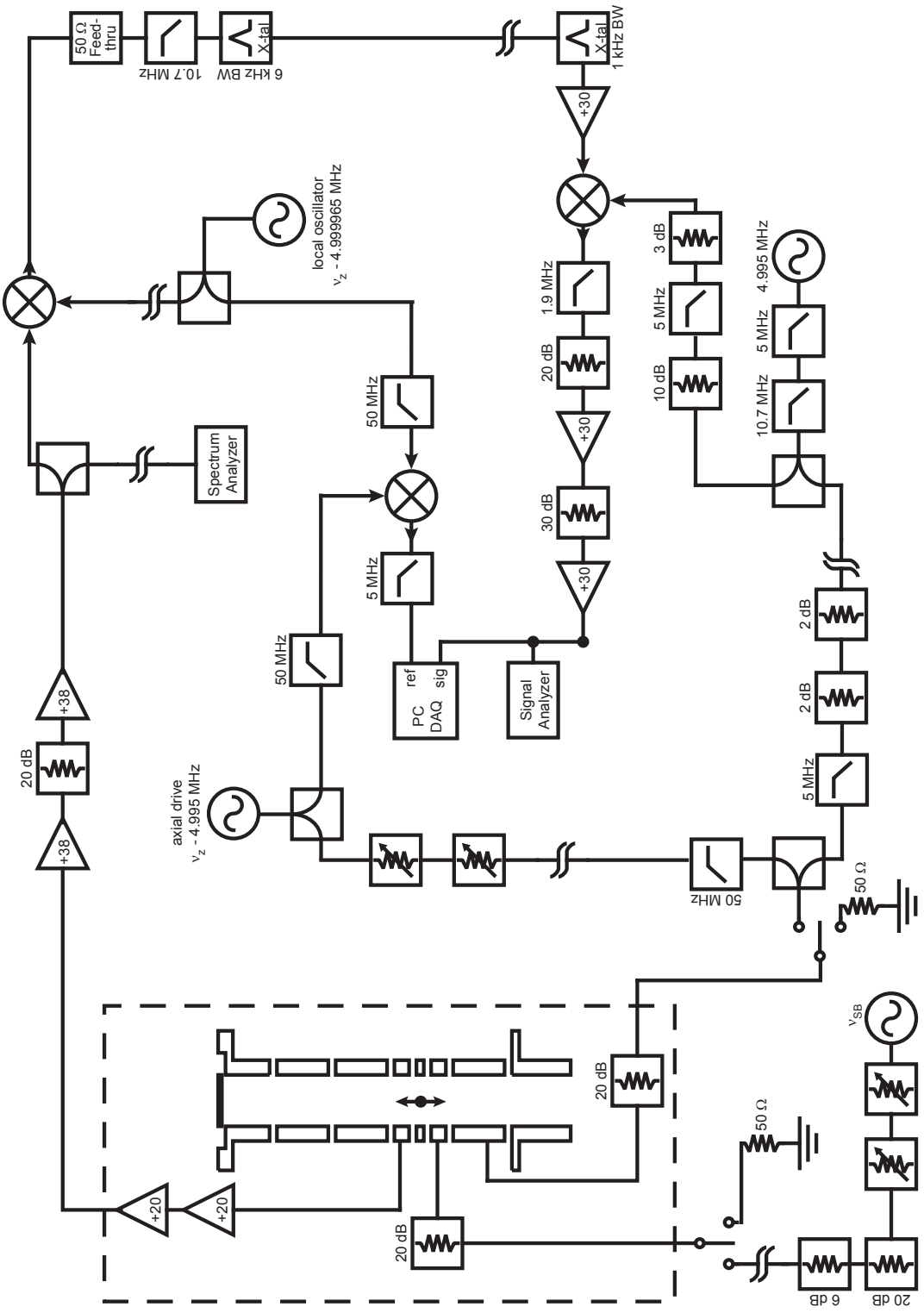

Figure 6.7: RF wiring diagram

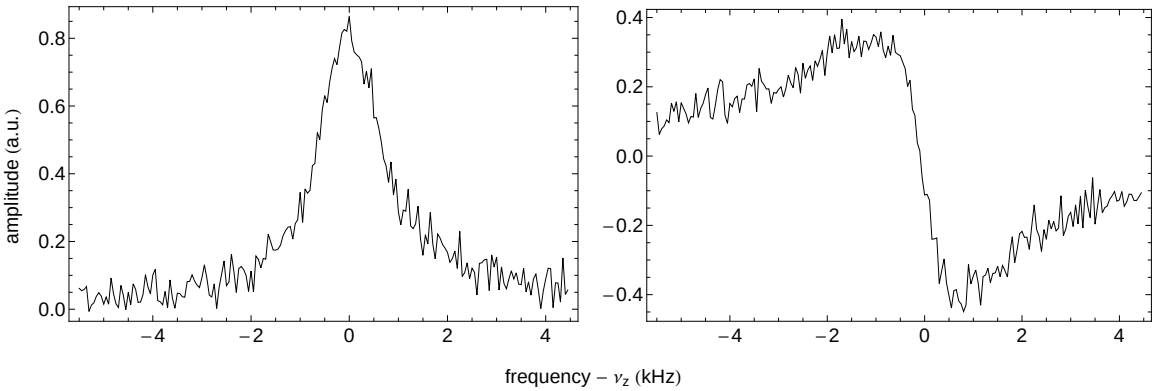

Figure 6.8: In-phase (left) and quadrature (right) driven axial response from a cloud of positrons in the loading trap with $\nu_z \approx 53.3$ MHz.

drives at $\nu_z - 5\,\mathrm{MHz}$ and $5\,\mathrm{MHz}$, is applied to the bottom endcap electrode. The details of the driving and detection scheme can be seen in Fig. 6.7.

As discussed in Section 5.6.1, we use a phase-sensitive detection method and record both the in-phase and quadrature components of the signal. An example of a driven signal can be seen in Fig. 6.8. The in-phase component is a Lorentzian whose FWHM is equal to $N\gamma_z$ and so can be used as a way to count the number of particles. Comparison of the driven signals is the primary means used in this chapter to determine the number of particles loaded in various configurations. Of course to actually determine N, one needs to know the single particle damping width. We have not yet conclusively determined the single particle damping width experimentally in the loading trap. We have calculated it to be $\sim 10\,\mathrm{Hz}$. However, all data in this chapter will simply be given in terms of the width of the driven signal, rather than the absolute number of particles.

6.4.4 "Cooling" the Magnetron Motion

As in the precision trap (see Section 5.5), it is necessary to "cool" the magnetron motion in order to detect the axial signal. As in the precision trap, the SB drive is applied to one-half of the bottom compensation electrode, which is split for this purpose. The main difference comes from the fact that the magnetron frequency is much smaller in the loading trap ($\sim 10\,\mathrm{kHz}$ versus $\sim 130\,\mathrm{kHz}$). For a single particle, or a very small number of particles, magnetron cooling proceeds by applying a drive at $\nu_z + \nu_m$ just as in the precision trap. However, for larger clouds, a strong cooling drive applied at $\nu_z + \nu_m$ might overlap with the axial signal and could excite the axial motion of the particles directly and/or heat the particles. We get around this by applying a strong cooling drive with an additional offset δ, made larger for larger clouds. This prevents the cooling drive from exciting the axial motion of particles in the cloud and heating the particles, although the cooling rate is somewhat slower as only the tail of the drive is at the cooling resonance.

6.5 Detailed Loading Analysis

In addition to simply loading positrons and electrons into the loading trap from the source, we have made a careful study of the loading mechanism to confirm that positrons and electrons are loaded via ionization of Rydberg positronium [84]. Three main potential configurations, as shown in Fig. 6.9, were used to study the loading mechanism. For convenience these three different configurations are labeled A, B, and C as shown. Potential configuration A was chosen and used initially because it

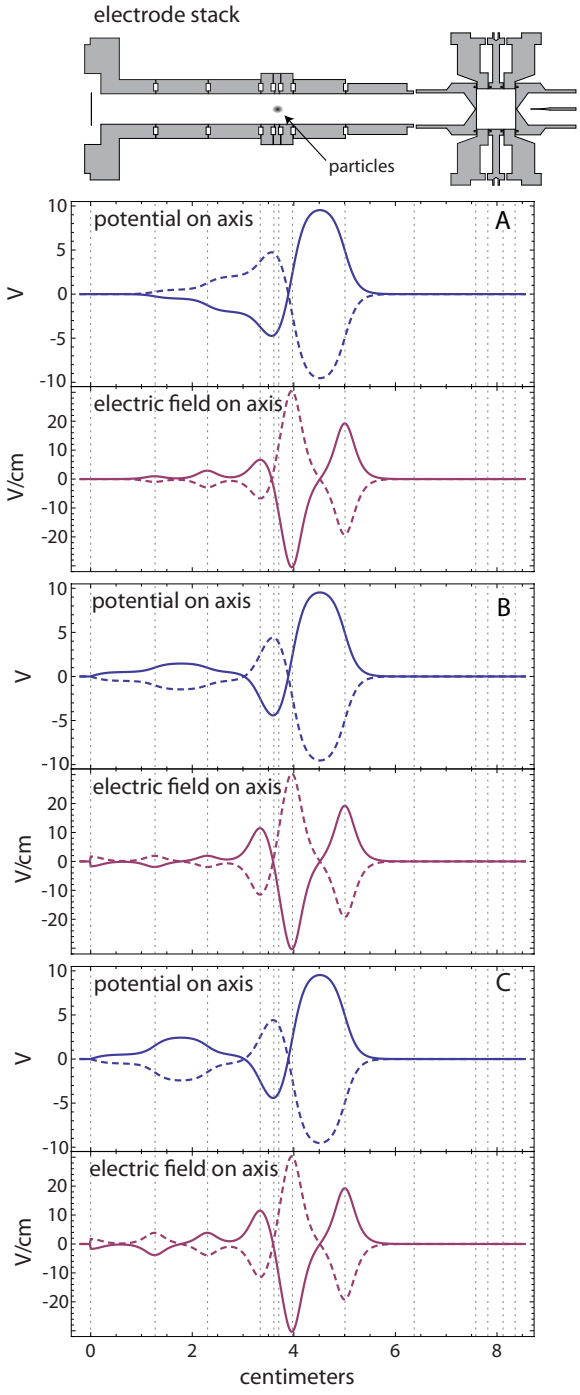

Figure 6.9: The three main potential configurations used in the loading trap to load both electrons and positrons. The solid lines indicate the potential and electric field configuration for positrons and the dashed lines indicate the configuration for electrons (with the potentials reversed). The labels A, B, and C will be used in the text to refer back to these configurations.

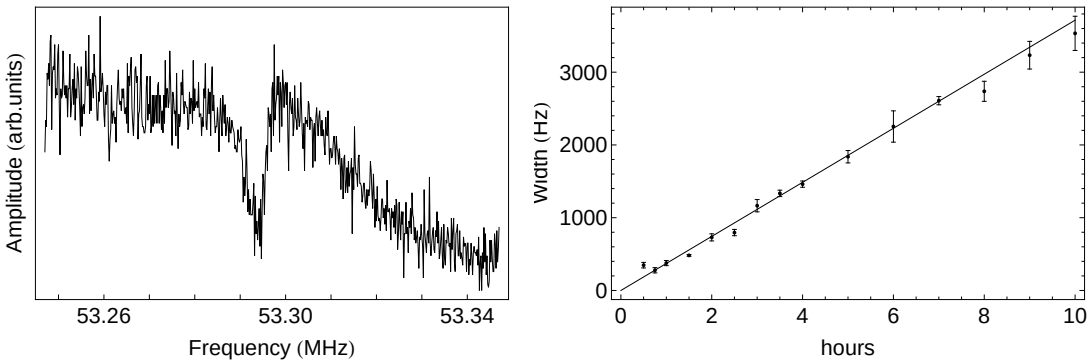

Figure 6.10: The dip from a cloud of positrons measured nondestructively and a plot of the positron loading rate from the source. These data were taken in configuration A and after the FEP had been fired 20 times.

minimizes the electric field at the front of the trapping well, which was found to be ideal in previous work loading positrons from positronium [84, 86, 92, 85], and was similar to typical potential configurations used in those previous studies. Figure 6.10 shows the linear nature of the positron loading rate in potential configuration A and gives an example of the dip from a cloud of positrons loaded for 10 hours. However, in this electrode potential configuration, electrons are loaded at a significantly higher rate than positrons. Figure 6.11 shows the difference in size between a cloud of positrons loaded for one hour into configuration A and a cloud of electrons loaded for one hour into the same configuration. If all of the loading is due to ionization of positronium within the trapping well the rates for positrons and electrons should be identical, and previous experiments that used this loading method (see, e.g. [84]) did indeed find equal electron and positron loading rates. This discrepancy was removed by preventing the loading of additional secondary electrons. The electrodes were biased to put a small potential "hill" between the moderator and the trapping well. The assumption is that this should cut down or eliminate individual charged particles

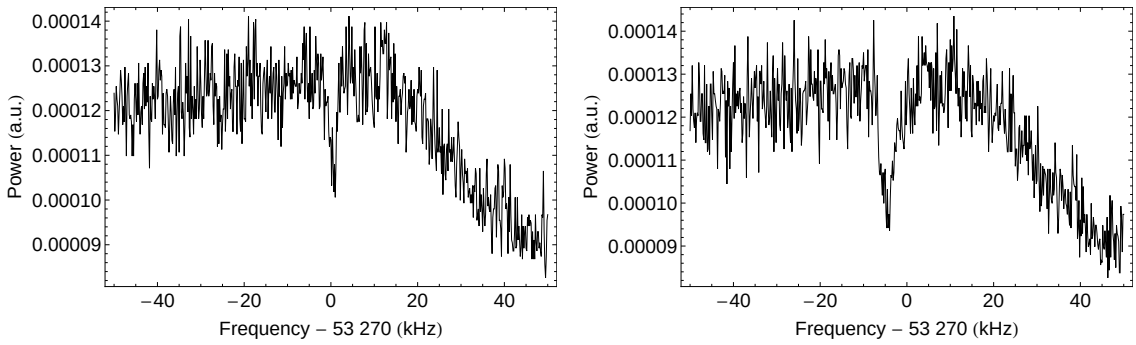

Figure 6.11: A comparison between the number of particles loaded during one hour of loading into potential configuration A as shown in Fig. 6.9. Positrons are shown on the left, electrons on the right.

from reaching the trapping well. We tried two different configurations, B and C as shown in Fig. 6.9, and found that this brought the loading rates for electrons and positrons into agreement as will be seen below.

Several additional tests were performed in addition to taking data in the three configurations given in Fig. 6.9. These included varying the moderator potential for electrons and positrons in several different configurations to determine the effect on loading rate and also moving the source further away from the moderator (and thus trap center). Additionally, we have taken data during two different cooldowns of the experiment. During the first cooldown, the FEP had been fired 20 times, with currents varying from about 100 pA to 2 nA and times varying from about 30 sec to 2 min, before the source loading tests were performed. After cycling the dilution refrigerator and trap to room temperature and back, the additional loading tests were performed immediately, without firing the FEP. The effects of all of these tests will now be discussed.

The same general procedure was used for all of our source loading tests. First,

the trap was dumped by inverting the trapping well and raising all other loading trap electrodes to +5 V (positrons) or -5 V (electrons) and left there for 5 minutes to ensure all particles were gone. Next all electrodes were ramped to the appropriate values for the desired loading configuration and left there for the desired length of time, typically 1-5 hours, although some points were taken at longer and shorter times. Finally the ring and compensation electrodes were ramped to their trapping voltages and all other loading trap electrodes were ramped to 0 V. These steps were automated to ensure uniform loading times. After the loading was complete, a round of magnetron cooling was performed and then a pair of driven axial scans was taken, once sweeping the drive up in frequency across the resonance and once sweeping the drive down in frequency across the resonance. Generally this axial scan was repeated and often an additional round of magnetron cooling was then performed followed by one more pair of axial scans. These steps were sometimes done in an automated fashion and sometimes performed by hand. The data from the automated scans were checked and any signals that were obviously not well magnetron cooled or were too far off the edge of the span were not included in the final data set. Additionally, some data were taken with the source in the loading position for the entire time and some data were taken with the source pulled up to the storage position after the loading was completed and before the scans were taken. No noticeable difference was observed.

The plots shown in the following figures and the data the following tables were generated as follows. The in-phase signal from each axial scan is fit to a Lorentzian to extract the FWHM and an error. Many points were taken at each loading time.

Table 6.1: Loading rate for positrons and electrons in the three main potential configurations, both without firing the FEP (second cooldown) and when firing the FEP 20 times before taking the data (first cooldown). All numbers are given in units of Hz/hour.

	FEP not fired		FEP fired 20 x	
	e^+	e^-	e^+	e^-
Configuration A	664(22)	3170(196)	371(5)	1563(54)
Configuration B	420(13)	222(16)	219(10)	–
Configuration C	224(8)	180(11)	122(8)	285(6)

The full data set for each configuration thus consists of a list of loading time, FWHM, and error. The loading rate and error are found by fitting a line to the full data set, forcing it to go through (0,0). Additionally, the mean value for each loading time was calculated by taking a weighted average of the data points, with an error bar given by the quadrature sum of the individual errors plus the standard deviation of the mean.

As can be seen in Fig. 6.12, the loading rate is generally linear for both positrons and electrons. When compared to the data taken without firing the FEP, the effect of firing the FEP 20 times is to cut the loading rate by approximately a factor of two, as shown in Fig. 6.12 and Table 6.1. This effect is not surprising, given that a similar effect was seen in previous work when a beam of antiprotons was allowed to strike the moderator or when a laser was used to heat the moderator in situ [84, 86, 92]. This loading method thus seems to depend upon a layer of adsorbed gas on the moderator. When this layer of gas is removed (e.g. by local heating and/or sputtering from an energetic beam of electrons from the FEP), the loading rate decreases. In the previous anti-hydrogen work, the effect of the antiproton beam coupled with the need for very

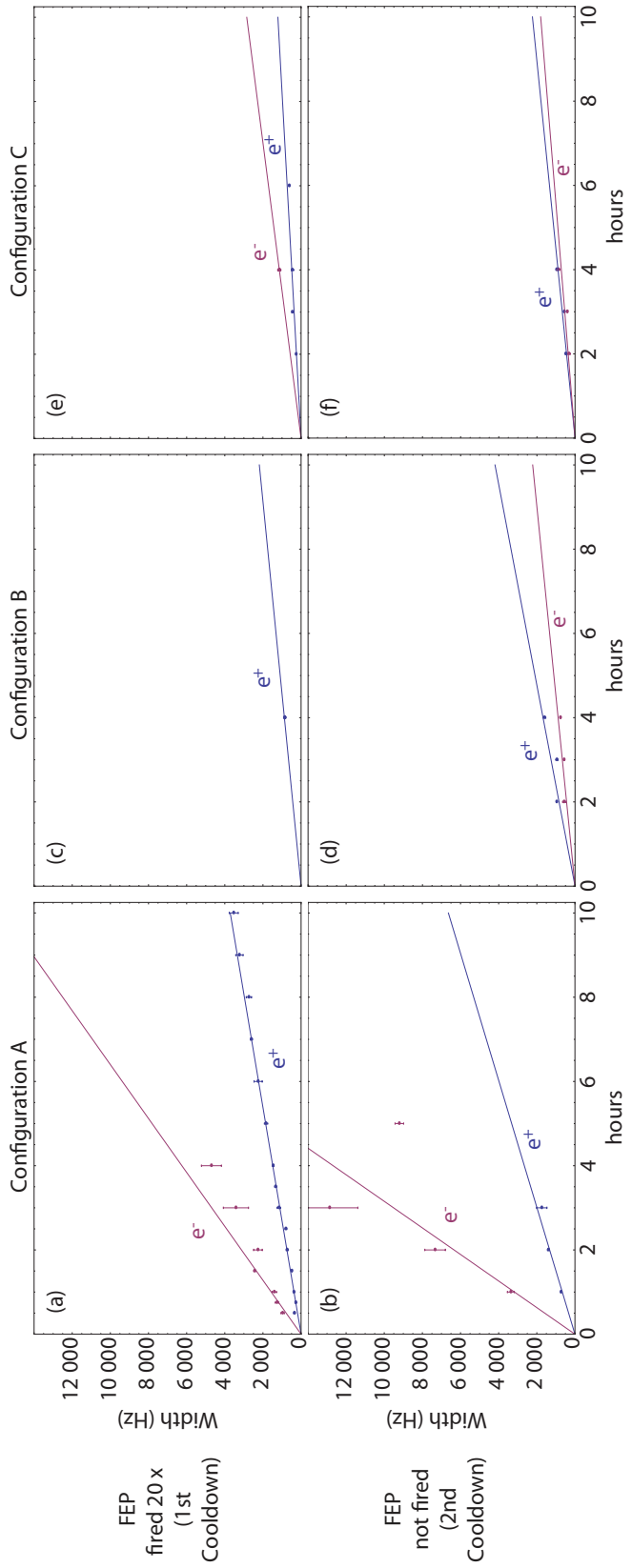

Figure 6.12: Positron and electron loading width versus time for the three potential configurations shown in Fig. 6.9. The upper plots show data from the 1st cooldown where we fired the FEP 20 times before loading particles from the source. The lower plots show data from the 2nd cooldown where we did not fire the FEP before the source loading trials. The loading rates are calculated from the slope and are listed in Table 6.1.

large clouds of positrons necessitated the installation of a special rotating electrode to protect the moderator from the antiproton beam. While the effect does need to be accounted for in our experiment, we do not expect it to prevent our measurement of the positron g-value. Given that only one positron is needed to perform the actual g-value measurement, the effect may ultimately be largely irrelevant. Some care will need to be taken during the remainder of the time spent optimizing the apparatus to minimize the number of times the FEP is fired unless no more positron loading tests need to be performed on a given cooldown. However, depending on the efficiency of transferring positrons from the loading trap to the precision trap (which is currently under investigation as will be discussed in Section 7.1.1) we may need to load only a very small number of positrons into the loading trap. Additionally, during the actual measurement, the FEP is typically only fired a few times in order to load one electron into the precision trap, which is then used to perform all of the measurements at a given value of the magnetic field. The dilution refrigerator will be thermally cycled after taking data at each value of the magnetic field so that the magnetic field can be changed and then shimmed using the helium-3 NMR probe. Thus, one could simply take the positron data at each magnetic field value first, followed by the electron data. The temperature cycle to move the field will then restore the loading rate for the next data point.

The three different potential configurations used to load electrons and positrons have an effect both on the overall loading rates and on the difference between positron and electron loading rates. This can be seen both in Fig. 6.12 and Table 6.1. As mentioned above, loading into configuration A yields significantly more electrons than

positrons (3-5 times more). Comparing the rates for configurations B and C, we see that the rates are in much better agreement although a minor discrepancy remains. The closing of the large discrepancy in configuration A suggests that our hypothesis of additional secondary electron loading is correct. The source of the remaining variation in loading rates in configurations B and C is likely due to a combination of the relative lack of data combined with possible systematic effects. Some variation in the number of electrons or positrons loaded for a given time and configuration was observed in cases when repeated measurements were performed and this variation was typically larger than the error in the signal width. This variation could result from variations in magnetron cooling during the different trials. Multiple repeated measurements at each loading time in each configuration would likely eliminate this remaining discrepancy. However, given that the ultimate goal of this project was to develop an efficient source of positrons to be used in a measurement of the positron g-value — which has been clearly demonstrated — we decided not to take the time to perform the additional loading trials.

To compare our results with previous work we can find a maximum positron loading rate per mCi and compare this to previous loading rates. In [84], the loading rate for positrons from the transmission moderator only (this apparatus also had an additional reflection moderator) is approximately $7\,e^+/s$ as given in Fig. 4(a). The source size is given as 2.5 mCi for a total loading rate of $2.8\,e^+/s/mCi$. This can be compared to our maximum positron loading rate (from configuration A without firing the FEP beforehand) which is 687(10) Hz/hr. At the time these data were taken, the source was approximately $6.3\,\mu Ci$. This gives a loading rate of $30\,Hz/s/mCi$. Using

Table 6.2: Raising the source 1.5 in (1 full turn) decreases the loading rate by nearly 50%. These data were taken in configuration B before firing the FEP. Numbers are given in Hz/hour.

Source Down	Source up 1.5"
420(13)	234(19)

the 10 Hz calculated single-particle damping rate gives a loading rate of 3 e^+/s/mCi. Given that actual value of γ_z tends to be somewhat smaller than the calculated values [67], we can estimate the loading rate to be 3-6 e^+/s/mCi. This is in surprisingly good agreement with previous work. We don't expect the loading rates to be exactly equal given that the different experiments have somewhat different distances between the moderator and the trapping well, losses due to self-absorption within the source should be smaller in our apparatus as discussed in Section 4.2, and our loading was done at 100 mK instead of 4 K. Nevertheless, the fact that the rates are not substantially different is a good sign and demonstrates that this loading mechanism works equally well for very small as well as very large sources. Additionally, as discussed in Section 4.2, we estimated the loading rate for positrons into the loading trap to be on the order of 1-2 e^+/min. This is in perfect agreement with our observed loading rate of 11 Hz/min — 1-2 e^+/min for a damping rate of 5-10 Hz. Finally, our observed loading rate of 1-2 e^+/min is 3-5 times larger than the loading rate achieved in the previous University of Washington positron g-value experiment (which used a different loading mechanism) [81, 52, 11] while our source is 50 times smaller.

The loading rate also depends upon the position of the source and on the voltage applied to the moderator during loading. Raising the source one full turn, or 1.5 in

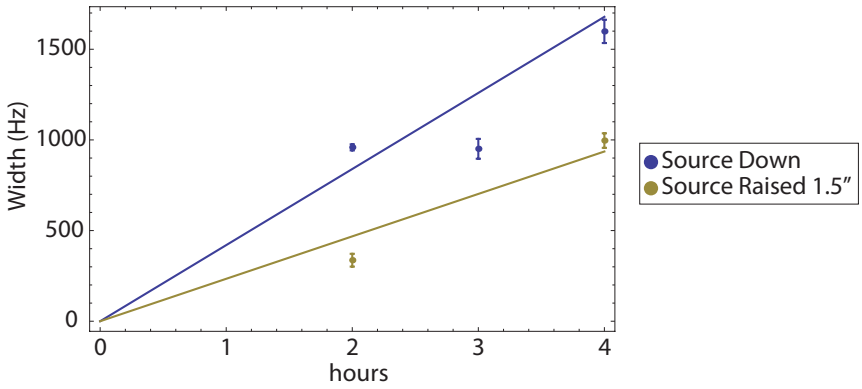

Figure 6.13: Raising the source 1.5 in above the usual loading position decreases the loading rate by nearly a factor of 2. These data were taken in configuration B in Fig. 6.9 and without firing the FEP beforehand.

up from the loading position decreases the loading rate by approximately a factor of two as seen in Fig. 6.13 and Table 6.2. This is expected since the number of positrons from the source that reach the moderator should decrease with increasing distance. Figure 6.14 shows the effect of varying the voltage applied to the transmission moderator during loading. Applying a voltage of V_t to the moderator should add energy eV_t to one species and remove eV_t from the other. This effects the spacing of the electron and positron in the Rydberg positronium, making it easier or more difficult to ionize. Previous work [84, 85, 86], done at 4 K and with a much larger positron source, found that the loading rate peaked with the moderator biased to ~ -0.5 V for both positrons and electrons. However, we found that in our apparatus at 100 mK the positron loading rate peaked with the moderator biased to ~ 0.5 V. It is not known what causes the difference but it is possibly related to the different temperatures in the different experiments.

We believe that we are indeed loading positrons (and electrons) via ionization of positronium for several reasons. The good agreement between our observed positron

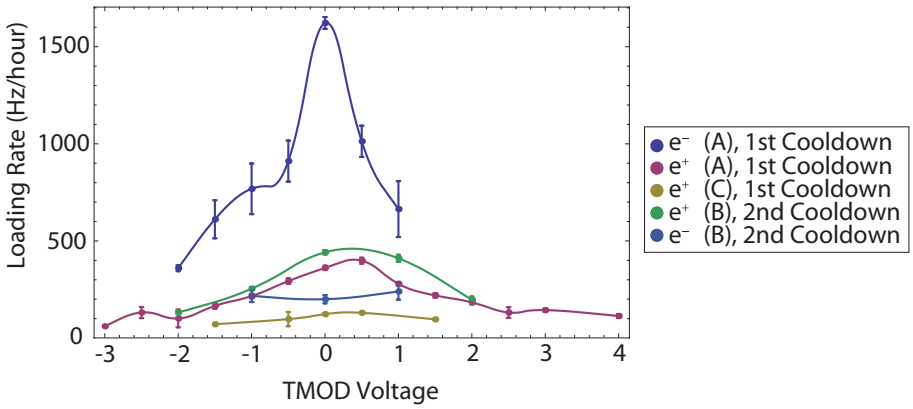

Figure 6.14: Varying the moderator voltage affects the loading rate of electrons and positrons. The peak rate for loading positrons in the configurations shown is around 0.5 V. The peak rate for loading electrons in the unblocked configuration (A in Fig. 6.9) is around 0 V. The difference is likely due to the secondary electron loading.

loading rate and both the predicted loading rate and the loading rate observed in previous experiments is a good indication that the loading mechanism is ionization of positronium. Additionally, there is no other obvious means of removing enough energy and momentum from the positrons leaving the moderator surface so that they can be trapped. The fact that electrons can be loaded from the source into the loading trap, in addition to positrons, by inverting the potentials implies that the loading must be from ionization of positronium unless there is an additional source of electrons. The difference in the relative electron and positron loading rates with and without the potential hill in front of the trapping well suggests that there is indeed a secondary source of electrons but that we are also loading positronium which is then ionized in the trap. Given all of the data, the best explanation is that positrons and electrons are indeed being loaded via field ionization of positronium.

We have developed a simple and relatively efficient means of loading positrons

into our apparatus for use in positron g-value measurements, using an extremely small source. Positrons are loaded via field ionization of Rydberg positronium — first demonstrated with a 2.5 mCi source [84] and a 150 mCi source [98, 86, 92], this method has now been shown to work equally well with a 6.5 μCi source. The loading rate normalized to the source size is 3-6 e^+/s/mCi for the 6.5 μCi source, in good agreement with the 2.8 e^+/s/mCi observed with the 2.5 mCi source [84]. Previous measurements of the positron g-value performed at the University of Washington, used a different loading method to achieve a loading rate of 23 e^+/hour with a 0.5 mCi source. We have demonstrated a 3-5 times higher positron loading rate with a 50 times smaller positron source. This new positron loading capability will allow us to make an improved measurement of the positron g-value.

Chapter 7

Next Steps and Future Directions

This chapter will discuss some of the necessary steps for making a positron g-value measurement in our new apparatus with our demonstrated positron loading capability. New techniques that could be implemented for making an improved g-value measurement will also be discussed.

7.1 Necessary Steps for a Positron g-Value Measurement

Demonstrating robust positron loading in the loading trap of the new apparatus is the first step towards a new positron g-value measurement. Additional steps include transferring positrons from the loading trap into the precision trap and getting down to one positron in the precision trap. The cavity modes need to be mapped to find the proper locations for performing the g-value measurement. Once a single positron is confined in the precision trap, the rest of the positron g-value measurement proceeds

just as the electron measurement, using all of the same techniques that have been developed.

7.1.1 Transferring Particles Between Traps

The ability to accumulate positrons in the loading trap is a huge step forward. Nevertheless it is ultimately not very useful unless at least some of the positrons can be transferred into the precision trap for the g-value measurement. Due to the 0.01" diameter hole in the precision trap top endcap electrode through which the positrons must be transferred, a cloud of particles cannot be transferred adiabatically from one trap to the other. Any heating that the particles experience will drive the magnetron motion to a larger orbit which will quickly send the particles into the electrode walls instead of through the small central transfer hole. Previous work [52, 99], as well as our own failure at transferring adiabatically, suggests that in order to transfer the particles through the small hole with any sort of reasonable efficiency, the transfer time needs to be short compared to an axial oscillation such that the particles do not have time to heat. The University of Washington g-value measurements used two hyperbolic traps for loading positrons and performing the measurement. As such they also had to transfer positrons from the loading trap through a similarly small hole in the top endcap of the measurement trap. This transferring was accomplished by briefly pulsing both endcaps to the common ring voltage for a few μs. They found that the pulses needed to be less than 10 μs in order to ensure a transfer efficiency of greater than 25%-50% [52]. The ATRAP antihydrogen collaboration also developed a fast pulsing scheme (10s of ns) in order to transfer positrons through an irregularly

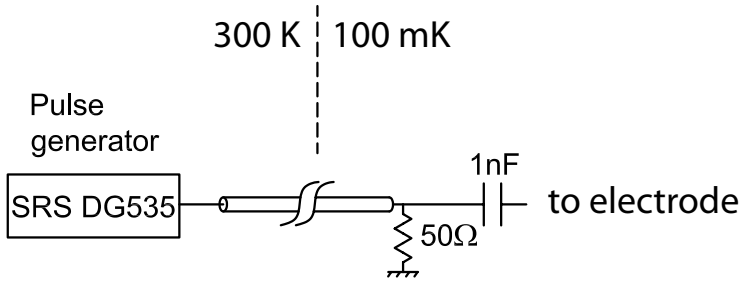

Figure 7.1: This is the basic pulsing scheme we plan to use to pulse positrons from the loading trap to the precision trap. This design is based on the circuit used in [99].

shaped rotating electrode ball valve [100, 99]. Although the ball valve has a larger aperture, the University of Washington work suggests that this scheme should also work for transferring through the 0.01" diameter hole in our precision top endcap.

There is a complication with such a fast pulsing scheme. As discussed in Section 5.2 and Section 6.3 we have carefully filtered our electrode bias lines to ensure the stability needed for the g-value measurement. All of the electrode bias lines in both traps have a minimum RC time constant of 100 ms (larger for the ring electrodes). Therefore to get the few volt pulse necessary to transfer the positrons we need to install additional pulsing lines which are unfiltered but we also need to minimize noise on these lines. We have installed two pulse lines, one on the loading trap bottom endcap and one on the precision trap top endcap, using the same design as in the antihydrogen work [99, Ch. 4]. These lines are microcoax lines which are capacitively coupled to the electrodes through a 1 nF capacitor, with a 50 Ω resistor to ground. When not in use, the lines are disconnected at room temperature and the connectors going into the fridge are shielded to minimize the transmission of noise to the electrodes. The basic circuit we intend to use is shown in Fig. 7.1, chosen based on

the design used in the previous antihydrogen work [99, Ch. 4]. The pulsing lines have been installed and preliminary tests have demonstrated the ability to pulse electrons out of either trap. Work on pulsing particles out of the loading trap and catching them in the precision trap is currently underway [101].

7.1.2 Cavity Mode Mapping

In order to perform a precise g-value measurement, it is necessary to map out the cavity mode structure. Before beginning the actual measurement, it will be important to confirm that the cavity mode structure matches the designed mode structure so that the proper magnetic field locations in which to perform the g-value measurements are known. Additionally, for any cavity-assisted axial sideband cooling attempts (see Section 7.2.1) we will need to know where the relevant cooling modes are located. This preliminary cavity mode mapping will be performed using the parametric motion of a small cloud of electrons. During the course of the g-value measurement the cavity modes will be carefully mapped out a second time using a single electron (or positron) to eliminate the systematic effects from the cavity on the g-value measurement at the highest levels of precision.

Parametric Mode Maps

A cloud of electrons in a Penning trap forms a system of well-controlled coupled oscillators. A drive applied to such a cloud at $\omega_d \approx 2\omega_z$ modulates the trapping potential V_R and parametrically excites the axial center-of-mass (CM) motion of the cloud at ω_z. This parametric drive displays threshold behavior, with no excitation

below a threshold drive strength. In a particular range of parameter space, the CM motion that is excited by the parametric drive above the threshold is proportional to the cyclotron damping rate. Thus, by applying a parametric drive above threshold and monitoring the CM motion while sweeping the magnetic field, the cavity mode structure can be determined. A sweep over the relevant magnetic field range can be performed in several hours.

The parametric excitation of a cloud of electrons and its use for probing the cavity mode structure were first observed in early work towards a g-value measurement with closed-endcap cylindrical Penning traps [102, 103, 104]. This ability to directly probe the cavity mode structure in a closed-endcap cylindrical Penning trap [56] and thus correct for the effects of the cavity on the cyclotron motion was one of the techniques that led to the significant improvement of our 2006 g-value measurement over the 1987 University of Washington g-value measurement. Work is currently underway on mapping the cavity mode structure of the precision trap using such parametric drives [105].

Single-Particle Mode Mapping

Because the cyclotron damping rate of a single particle depends up on the location of the cyclotron frequency with respect to the cavity modes, the single particle itself can be used as a high-precision probe of the relevant mode structure. This ability to accurately map the cavity mode interactions with a single electron was one of the key steps in the 2008 measurement of the electron g-value, and it will remain necessary in future g-value measurements of positrons and electrons in the new precision trap.

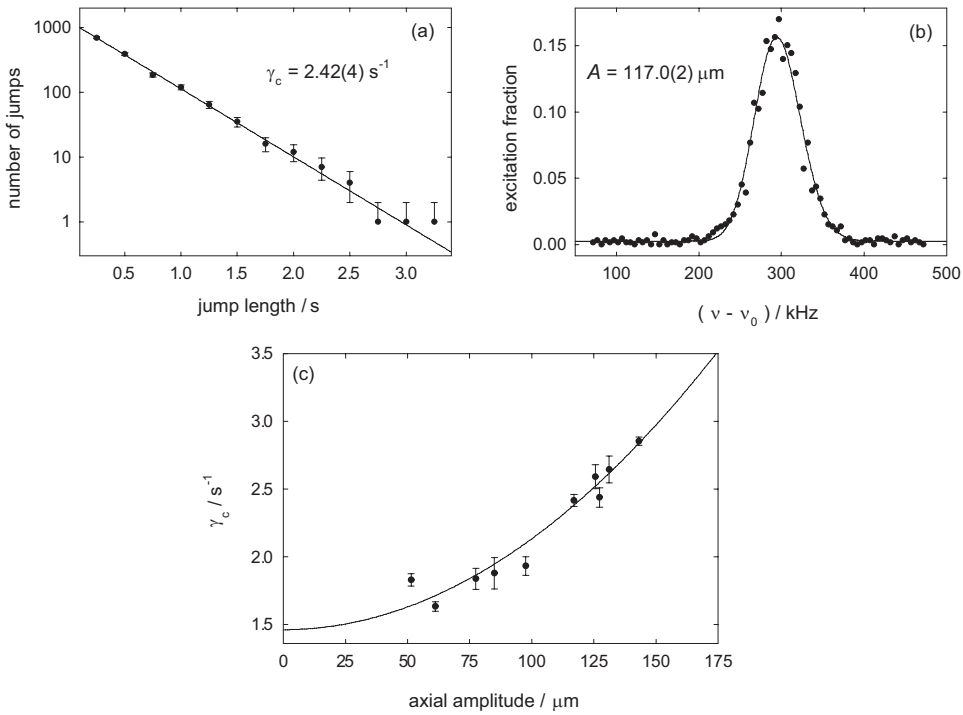

Figure 7.2: Measurement of the cyclotron damping rate at 146.7 GHz for single-particle mode-mapping in the old trap used in the 2008 g-value measurement. We measure the cyclotron damping rate as a function of amplitude to extract the zero amplitude lifetime and curvature as shown in (c). Each data point in (c) consists of a damping rate measured from a histogram of cyclotron lifetimes (a) and an axial amplitude measured from a driven cyclotron line (b). This figure was produced using data from the 2008 g-value measurement that were also used in [70].

This single-particle mode mapping technique uses the variation in the cyclotron damping rate as the cyclotron frequency comes into and out of resonance with the cavity modes. The procedure is as follows. At a particular cyclotron frequency, many (typically hundreds) of cyclotron transitions are excited and a histogram of cyclotron jump length is made as shown in Fig. 7.2a. We fit this distribution to a decaying exponential with time constant γ_c^{-1} to determine the cyclotron damping rate γ_c. The presence of the cavity modes adds an amplitude-dependence to γ_c so we also determine the thermal axial amplitude by fitting a cyclotron line taken with the amplifiers off but the SXO on as shown in Fig. 7.2b. Such a line has a center frequency that is shifted from the SXO-off cyclotron frequency with the shift proportional to the axial amplitude. This procedure is repeated for several different values of thermal axial amplitude, accomplished by varying the compensation voltage which changes the amplitude of the axial oscillation in the SXO. We then fit the γ_c versus amplitude data to determine the zero amplitude damping rate and the curvature (see Fig. 7.2c). The entire procedure is repeated at many different values of magnetic field throughout the region of interest. When the cyclotron frequency is far from any mode, the damping rate curvature is relatively flat. When the cyclotron frequency is near a mode with a node at the center, such as a cooling mode, γ_c will increase with increasing amplitude. Conversely, near a mode with an anti-node at the center, such as a cyclotron-coupling mode, γ_c will decrease with decreasing amplitude. Further details of this procedure can be found in [2] and [70, Ch. 5]. This method yields a very accurate determination of the cavity shift since it uses the single particle coupling directly. However it is significantly slower than the parametric mode maps — 1-2 days worth of data are

needed at each value of the magnetic field and ~ 10 magnetic field values are required to map out the region in which the g-value measurement is performed.

7.1.3 Positron g-Value Measurement

Once a single positron is trapped in the precision trap, the positron g-value measurement proceeds exactly like the electron measurement. All of the same techniques that have been developed to enable a measurement of the electron g-value to 0.28 ppt [1, 2] can be implemented without change to measure the positron g-value. In particular, the cyclotron and anomaly frequency measurements proceed in the same fashion as discussed in Section 5.7.1 and Section 5.8.1. Only the time required to accumulate the necessary statistics and to account for and eliminate the systematic effects in the same way as for electrons is needed.

7.2 Future Improvements

The new high-stability apparatus, smaller magnetic bottle, and positron source should provide an improved measurement of the positron g-value requiring no new techniques. Going forward, there are a number of possible additional techniques that could be implemented to enable an even more precise measurement of the electron and positron g-values. Two of these will be mentioned below.

7.2.1 Cavity-Assisted Axial Sideband Cooling

One possible method for improving the precision of the electron and positron g-value measurements beyond any improvement that comes solely from the new apparatus and the smaller magnetic bottle is to cool the axial motion. Because the width of the cyclotron and anomaly lines are dependent upon the axial temperature, a reduction in axial temperature would result in a narrowing of the lines, allowing a more precise determination of the frequencies. In the current set-up, the axial motion is coupled to the thermal reservoir of the axial amplifier, which is at or near the base temperature of the dilution refrigerator. Due to the ever-decreasing amount of cooling power available as the temperature of the dilution refrigerator is lowered, it is not practical to run the dilution refrigerator with the mixing chamber much below 100 mK, even with the increased amount of cooling power available in the new fridge. Therefore, more clever techniques will need to be implemented if one hopes to achieve further cooling of the axial motion.

One such technique that seems quite promising is the method of cavity-assisted axial sideband cooling. In the same way that the magnetron motion can be cooled by coupling it to the axial motion as discussed in Section 5.5, the axial motion can be cooled by coupling it to the cyclotron motion. The theoretical limit is equal quantum numbers which would be the axial ground state, although any level of cooling would be beneficial. The key is that the axial motion must be decoupled from the thermal reservoir of the amplifier during the cooling and subsequent cyclotron or anomaly transition driving, and only re-coupled at the end to see whether or not a transition has been made. Due to the difficulty of constructing an RF switch that is non-

magnetic, works at 100 mK and does not destroy the amplifier Q, this decoupling is done by detuning the axial frequency from resonance with the amplifier and then bringing it back into resonance with the amplifier for the detection. As discussed in Section 2.1.2, the new precision trap was designed with several accessible cooling modes to facilitate cavity-assisted axial sideband cooling attempts. However, the cooling procedure still needs to be developed and implemented.

The rate for heating (upper sign) and cooling (lower sign) of the axial motion coupled to the cyclotron motion is given by ([67, Sec. IV.C])

$$\gamma_z^{(\pm)}(\epsilon) = \mathrm{Im}\left[(\epsilon + \imath\gamma_c/2)\left(1 - \sqrt{1 \mp \frac{\gamma_0\gamma_c}{(\epsilon + \imath\gamma_c/2)^2}}\right)\right], \tag{7.1}$$

where ϵ is the detuning of the drive from the sideband frequency and, for a plane wave coupling of the motions,

$$\gamma_0 = \frac{e^2 E_0^2 \omega_d \omega_c^{'}}{4\gamma_c m^2 c^2 \omega_z(\omega_c^{'} - \omega_m)}, \tag{7.2}$$

where E_0^2 is the strength of the plane wave coupling drive. Near resonance with one of the cavity cooling modes, a geometric term is added to γ_0 that depends upon the particular mode. While this geometric term can be larger than 1 for some cavity modes, the primary reason for tuning near a cavity mode is to enable large amounts of power to be coupled into the cavity, since the cooling rate is proportional to the strength of the drive. In order to get appreciable cooling rates, significant amounts of microwave power are required. Additionally, the cooling modes ($\mathrm{TE}_{1n(\mathrm{even})}$ and $\mathrm{TM}_{1n(\mathrm{even})}$) have the appropriate geometry to encourage the coupling between the axial and cyclotron motions.

Some preliminary trials were performed in the old apparatus, both at 147.5 GHz[70,

Ch. 7] and later at 145.1 GHz. The former was 30 linewidths above the nearest cooling mode (TE_{136}) but the later was 200 MHz above TE_{144}, to put the cooling sideband right on resonance with the cavity cooling mode. With the cyclotron frequency at 147.5 GHz we saw only a noisier cyclotron line, as the cooling drive excited the cyclotron motion but the cooling rate was so low that even with a 15 minute cooling pulse at full microwave power we saw no indication of cooling. Moving the cyclotron frequency to 145.1 GHz was marginally more successful. We saw some indication of cooling when driving the cooling sideband — as the cooling pulse time increased, the excitation fraction on the sideband decreased. The excitation fraction is expected to eventually go to zero as the axial state cools to zero, at which point there is no more axial energy to make up the difference between the drive (at the sideband frequency) and the cyclotron frequency and thus no more cyclotron excitations. Attempts to see narrower (cooled) cyclotron lines remained unsuccessful. There was a significant amount of hysteresis and some noise in the frequency of the axial signal as the axial frequency was detuned from and retuned into resonance with the amplifier. The hysteresis was partially overcome by first overshooting the voltage when retuning into resonance with the amplifier as discussed in Section 5.2 but not eliminated. It may prove helpful to untie the defined $n = 0$ axial frequency and just look for cyclotron transitions of the correct size after retuning the axial frequency and declaring the final frequency after any transitions to be $n = 0$. Another possibility might be to actually install a larger magnetic bottle. The larger cyclotron jump size would minimize the effects of axial frequency instability although the effect of the still non-zero ground state axial amplitude in the bottle field would have to be carefully considered.

Finding a way to physically decouple the amplifier from the electrode may be an even better option.

7.2.2 Regulated Liquid Helium Level

In addition to allowing us to insert and remove the dilution refrigerator directly into the helium space, the outer G-10 and aluminum sleeve on the fridge serves to separate the helium space into an inner space around the fridge and an outer space in the rest of the dewar. This provides the possibility of regulating the helium level around the dilution refrigerator by pressurizing the outer dewar space to force the helium level in the inner space to remain at a constant level. By maintaining the liquid helium at a constant level around the dilution refrigerator, any instabilities due to changing thermal gradients, including thermoelectric effects, would by minimized. A capacitive helium level sensor that is accurate to better than 100 μm has been constructed and installed on top of the IVC top plate. A proof-of-principle demonstration has been done on a system to pressurize the outer helium space in order to maintain a constant level in the inner space. More work will be required if a robust system is to be incorporated into the apparatus and used during g-value measurements.

Chapter 8

Conclusion

A single particle confined in a cylindrical Penning trap provides an excellent platform for precision measurements of the particle g-value. Our 2008 electron g-value measurement provides the most precise determination of the electron g-value at 0.28 ppt [1], which in turn is the most precise determination of a fundamental property of any elementary particle. When combined with QED theory, this measurement yields the most precise determination of the fine structure constant.

An entirely new apparatus has been constructed for a next generation of measurements of the electron or positron magnetic moments. The new apparatus contains a positron source designed to robustly provide positrons from the smallest possible source to minimize disruptions of the precision measurement. This new apparatus will allow an improved positron g-value measurement as well as an even more precise measurement of the electron g-value and fine structure constant and more stringent tests of CPT invariance.

This new apparatus has a number of features that will improve our g-value mea-

surements. The electric and magnetic portions of the precision Penning trap are mechanically coupled at 4 K to minimize the effect of vibrations and thermal fluctuations. Centering pins provide radial alignment of the trap and solenoid. An improved passive shield coil minimizes magnetic fluctuations. A smaller magnetic bottle narrows the cyclotron and anomaly linewidths, increasing the precision with which they can be measured. Preliminary tests in the new apparatus demonstrate some of these improvements including the ability to detect cyclotron transitions with the smaller magnetic bottle installed.

The new apparatus also contains a robust positron loading mechanism. A retractable positron source can be moved between loading and storage positions while cold and also can be removed entirely from the apparatus when necessary. A secondary positron loading trap facilitates the accumulation of positrons at a reasonable rate. The successful loading of positrons from the source in the loading trap has been demonstrated. Up to 1-2 e^+/min are accumulated in the loading trap from a 6.5 μCi ^{22}Na positron source. This rate is 3-5 times larger for a fifty times smaller source than was used in previous positron g-value measurements [52, 11]. A method to transfer positrons (or electrons) from the loading trap to the precision trap is now being developed. With the new apparatus fully functional and the positron loading working reliably, prospects are good for a single-positron quantum cyclotron and a new measurement of the positron g-value.

Appendix A

Magnet Calculations

Because the stability and homogeneity of the magnetic field and the magnetic shielding are so important for making precise measurements of the electron and positron magnetic moments, we worked closely with Cryomagnetics during the design and construction of the superconducting solenoid to ensure that it met our needs. In particular, we spent some effort confirming that the winding parameters used in the design would give the appropriate self- and mutual inductances, the correct magnetic field strength and homogeneity, and that the shield coil design and testing would give the largest possible shielding factor for uniform ambient magnetic field fluctuations.

The calculations were performed for the main coil, the Z0 coil, the shield coil, and the Z, Z^2 and Z^3 shim coils. The effect of the radial shim coils was not taken into consideration. Each coil was broken down into several sub-coils, with the following data inputs given to us by Cryomagnetics for each sub-coil.

```
inner radius

outer radius
```

```
length
z-position of coil center
number of layers
number of turns per layer
current
wire cross-section width
wire cross-section height
```

The input data for each sub-coil in the system, listed above, is converted into a list of current loops of radius ρ_x and axial position z_x. This list takes the form $((\rho_1, z_1), (\rho_1, z_2), \ldots, (\rho_2, z_1), (\rho_2, z_2), \ldots)$. The following equations are then used in the calculations discussed below. The mutual inductance between two current loops with radii ρ_1 and ρ_2 and axial separation z is computed using [106]

$$M(\rho_1, \rho_2, z) = 2\pi \times 10^{-7} r[2(K(k) - E(k)) - k^2 K(k)], \tag{A.1}$$

where $r = ((\rho_1 + \rho_2)^2 + z^2)^{1/2}$, $k = (4\rho_1\rho_2/r^2)^{1/2}$ and $K(k)$ and $E(k)$ are complete elliptic integrals of the first and second kinds. The z-component of the magnetic field due to a current loop of radius ρ at a point (r, z) in cylindrical coordinates can be found by (see, e.g. [69, Sec. 5.5])

$$B_z(r, z, I, \rho) = \frac{I\mu_0}{2\pi}\left(\frac{1}{\sqrt{\gamma}}\left(E(k)\frac{\rho^2 - r^2 - z^2}{(\rho + r)^2 + z^2 - 4\rho r} + K(k)\right)\right), \tag{A.2}$$

where μ_0 is the permeability of free space, $\gamma = (\rho + r)^2 + z^2$ and $k^2 = \frac{4\rho r}{(\rho+r)^2+z^2}$ and again $K(k)$ and $E(k)$ are complete elliptic integrals of the first and second kinds. The self inductance of a current-carrying loop is found by integrating B_z around the loop to find the flux through the loop and dividing the flux by the current in the loop.

The expression then is

$$L_{\text{loop}}(\rho, \delta) = \frac{2\pi}{I} \int_0^{\rho-\delta} B_z(r, 0, I, \rho) r \, \mathrm{d}r, \tag{A.3}$$

where ρ is the radius of the loop, δ is the radius of the wire, and I is the current in the loop. The z-component of the magnetic field at a point z on the axis due to a finite solenoid can be found by integrating $B_z(0, z, I, \rho)$ over a range of axial displacements and radii to get

$$B_z(z) = \frac{\mu_0 I n}{2(\rho_2 - \rho_1)} \left[(z+l) \ln \left(\frac{\rho_2 + \sqrt{\rho_2^2 + (z+l)^2}}{\rho_1 + \sqrt{\rho_1^2 + (z+l)^2}} \right) - z \ln \left(\frac{\rho_2 + \sqrt{\rho_2^2 + z^2}}{\rho_1 + \sqrt{\rho_1^2 + z^2}} \right) \right], \tag{A.4}$$

where ρ_1 is the inner radius of the solenoid, ρ_2 is the outer radius of the solenoid, n is the number of turns per unit length of the solenoid and l is the length of the solenoid.

The self-inductance of each sub-coil is found by summing the self-inductance of each loop (calculated from Eq. A.3) plus twice the mutual inductance between each pair of loops (calculated from Eq. A.1). The mutual inductance between each pair of sub-coils is found by summing the mutual inductance of each current loop in one sub-coil with each current loop in the other sub-coil, as computed by Eq. A.1.

The calculation of the shielding factor for a system of solenoid circuits is discussed in [79, Sec. IV]. We have a system of N superconducting coils, each of which is composed of a sub-set of the $\tilde{N}$ sub-coils. We define an inductance matrix, $\tilde{\mathbf{L}}$ where $\tilde{L}_{ii}$ is the self-inductance of sub-coil i and $\tilde{L}_{ij}$ is the mutual inductance between sub-coils i and j, calculated as above. We define an area column vector, $\tilde{\mathbf{A}}$ for each-sub coil by summing the area of each current loop in the sub-coil. We also define a column vector $\tilde{\mathbf{g}}$ where $\tilde{\mathrm{g}}_i = B_i(0,0)/I_i$, with $B_i(0,0)$ computed from Eq. A.4 for each sub-coil. To contract the system of sub-coils into the system of coils (main, Z0, etc.), we define

an $N \times \tilde{N}$ matrix, Ω, such that $\Omega_{ij} = 1$ if coil i includes sub-coil j and the sub-coil has current flowing in the same direction as the majority of the system, $\Omega_{ij} = -1$ if coil i includes sub-coil j but the sub-coil has current flowing in the opposite direction as the rest of the system, and $\Omega_{ij} = 0$ otherwise. Then the shielding factor for the system is found by solving

$$S^{-1} = 1 - \mathbf{g}^T \mathbf{L}^{-1} \mathbf{A}, \tag{A.5}$$

where $\mathbf{g} = \Omega\tilde{\mathbf{g}}$, $\mathbf{A} = \Omega\tilde{\mathbf{A}}$, and $\mathbf{L} = \Omega\tilde{\mathbf{L}}\Omega^T$ with the superscript T indicating transposition.

To confirm the design given by Cryomagnetics, we compared the total self-inductance of each coil, the mutual inductance between each pair of coils, the maximum value of the magnetic field at the center of the main coil, the homogeneity of the main coil, and the shielding factor for the system, both with and without the shield coil, and with different numbers of turns on the shield coil. These checks were repeated before and after the various sections of the solenoid were wound.

Bibliography

[1] Hanneke, D., Fogwell, S. & Gabrielse, G. New measurement of the electron magnetic moment and the fine structure constant. *Phys. Rev. Lett.* **100**, 120801 (2008).

[2] Hanneke, D., Fogwell Hoogerheide, S. & Gabrielse, G. Cavity control of a single-electron quantum cyclotron: Measuring the electron magnetic moment. *Phys. Rev. A* **83**, 052122 (2011).

[3] Uhlenbeck, G. E. & Goudsmit, S. Spinning electrons and the structure of spectra. *Nature* **117**, 264–265 (1926).

[4] Dirac, P. A. M. The quantum theory of the electron. *Proceedings of the Royal Society of London. Series A, Containing Papers of a Mathematical and Physical Character* **117**, pp. 610–624 (1928).

[5] Dirac, P. A. M. The quantum theory of the electron. Part II. *Proceedings of the Royal Society of London. Series A* **118**, 351–361 (1928).

[6] Kusch, P. & Foley, H. Precision measurement of the ratio of the atomic 'g values' in the $^2P_{3/2}$ and $^2P_{1/2}$ states of gallium. *Physical Review* **72**, 1256 (1947).

[7] Schwinger, J. On quantum-electrodynamics and the magnetic moment of the electron. *Phys. Rev.* **73**, 416–417 (1948).

[8] Rich, A. & Wesley, J. C. The current status of the lepton g factors. *Rev. Mod. Phys.* **44**, 250–283 (1972).

[9] Roberts, B. L. & Marciano, W. J. *Lepton Dipole Moments*, vol. 20 (World Scientific, 2010).

[10] Wineland, D., Ekstrom, P. & Dehmelt, H. Monoelectron oscillator. *Phys. Rev. Lett.* **31**, 1279–1282 (1973).

[11] Van Dyck, Jr., R. S., Schwinberg, P. B. & Dehmelt, H. G. New high-precision comparison of electron and positron g factors. *Phys. Rev. Lett.* **59**, 26–29 (1987).

[12] Odom, B., Hanneke, D., D'Urso, B. & Gabrielse, G. New measurement of the electron magnetic moment using a one-electron quantum cyclotron. *Phys. Rev. Lett.* **97**, 030801 (2006).

[13] Petermann, A. Fourth order magnetic moment of the electron. *Helv. Phys. Acta* **30**, 407–408 (1957).

[14] Sommerfield, C. M. Magnetic dipole moment of the electron. *Phys. Rev.* **107**, 328–329 (1957).

[15] Sommerfield, C. M. The magnetic moment of the electron. *Ann. Phys.* **5**, 26–57 (1958).

[16] Laporta, S. & Remiddi, E. The analytical value of the electron $(g-2)$ at order α^3 in QED. *Phys. Lett. B* **379**, 283–291 (1996).

[17] Aoyama, T., Hayakawa, M., Kinoshita, T. & Nio, M. Tenth-order QED contribution to the electron $g-2$ and an improved value of the fine structure constant. *Phys. Rev. Lett.* **109**, 111807 (2012).

[18] Aoyama, T., Hayakawa, M., Kinoshita, T. & Nio, M. Quantum electrodynamics calculation of lepton anomalous magnetic moments: Numerical approach to the perturbation theory of QED. *Progress of Theoretical and Experimental Physics* **01A**, 107 (2012).

[19] Passera, M. Precise mass-dependent QED contributions to leptonic $g-2$ at order α^2 and α^3. *Phys. Rev. D* **75**, 013002 (2007).

[20] Mohr, P. J., Taylor, B. N. & Newell, D. B. CODATA recommended values of the fundamental physical constants: 2010. *Rev. Mod. Phys.* **84**, 1527–1605 (2012).

[21] Bouchendira, R., Cladé, P., Guellati-Khélifa, S., Nez, F. m. c. & Biraben, F. m. c. New determination of the fine structure constant and test of the quantum electrodynamics. *Phys. Rev. Lett.* **106**, 080801 (2011).

[22] Mount, B. J., Redshaw, M. & Myers, E. G. Atomic masses of ^{6}Li,^{23}Na,^{39,41}K,^{85,87}Rb, and ^{133}Cs. *Phys. Rev. A* **82**, 042513 (2010).

[23] Farnham, D. L., Van Dyck, Jr., R. S. & Schwinberg, P. B. Determination of the electron's atomic mass and the proton/electron mass ratio via Penning trap mass spectroscopy. *Phys. Rev. Lett.* **75**, 3598–3601 (1995).

[24] Gerginov, V., Calkins, K., Tanner, C. E., McFerran, J. J., Diddams, S., Bartels, A. & Hollberg, L. Optical frequency measurements of $6s\,^2S_{1/2} - 6p\,^2P_{1/2}$ (D_1) transitions in ^{133}Cs and their impact on the fine-structure constant. *Phys. Rev. A* **73**, 032504 (2006).

[25] Wicht, A., Hensley, J. M., Sarajlic, E. & Chu, S. A preliminary measurement of the fine structure constant based on atom interferometry. *Phys. Scr.* **T102**, 82–88 (2002).

[26] Müller, H., Chiow, S.-W., Long, Q., Vo, C. & Chu, S. A new photon recoil experiment: towards a determination of the fine structure constant. *Appl. Phys.B* **84**, 633–642 (2006).

[27] Pohl, R., Antognini, A., Nez, F., Amaro, F. D., Biraben, F., Cardoso, J. M. R., Covita, D. S., Dax, A., Dhawan, S., Fernandes, L. M. P., Giesen, A., Graf, T., Hnsch, T. W., Indelicato, P., Julien, L., Kao, C.-Y., Knowles, P., Le Bigot, E.-O., Liu, Y.-W., Lopes, J. A. M., Ludhova, L., Monteiro, C. M. B., Mulhauser, F., Nebel, T., Rabinowitz, P., dos Santos, J. M. F., Schaller, L. A., Schuhmann, K., Schwob, C., Taqqu, D., Veloso, J. F. C. A. & Kottmann, F. The size of the proton. *Nature* **466**, 213–216 (2010).

[28] Antognini, A., Nez, F., Schuhmann, K., Amaro, F. D., Biraben, F., Cardoso, J. M. R., Covita, D. S., Dax, A., Dhawan, S., Diepold, M., Fernandes, L. M. P., Giesen, A., Gouvea, A. L., Graf, T., Hnsch, T. W., Indelicato, P., Julien, L., Kao, C.-Y., Knowles, P., Kottmann, F., Le Bigot, E.-O., Liu, Y.-W., Lopes, J. A. M., Ludhova, L., Monteiro, C. M. B., Mulhauser, F., Nebel, T., Rabinowitz, P., dos Santos, J. M. F., Schaller, L. A., Schwob, C., Taqqu, D., Veloso, J. F. C. A., Vogelsang, J. & Pohl, R. Proton structure from the measurement of 2S-2P transition frequencies of muonic hydrogen. *Science* **339**, 417–420 (2013).

[29] Brodsky, S. J. & Drell, S. D. Anomalous magnetic moment and limits on fermion substructure. *Phys. Rev. D* **22**, 2236–2243 (1980).

[30] Bourilkov, D. Hint for axial-vector contact interactions in the data on $e^+e^- \to e^+e^-(\gamma)$ at center-of-mass energies 192–208 GeV. *Phys. Rev. D* **64**, 071701 (2001).

[31] Nakamura, K. & Particle Data Group. Review of particle physics. *Journal of Physics G: Nuclear and Particle Physics* **37**, 075021 (2010).

[32] Wu, C. S., Ambler, E., Hayward, R. W., Hoppes, D. D. & Hudson, R. P. Experimental test of parity conservation in beta decay. *Phys. Rev.* **105**, 1413–1415 (1957).

[33] Christenson, J. H., Cronin, J. W., Fitch, V. L. & Turlay, R. Evidence for the 2π decay of the K_2^0 meson. *Phys. Rev. Lett.* **13**, 138–140 (1964).

[34] Alavi-Harati, A., Albuquerque, I. F., Alexopoulos, T., Arenton, M., Arisaka, K., Averitte, S., Barker, A. R., Bellantoni, L., Bellavance, A., Belz, J., Ben-David, R., Bergman, D. R., Blucher, E., Bock, G. J., Bown, C., Bright, S.,

Cheu, E., Childress, S., Coleman, R., Corcoran, M. D., Corti, G., Cox, B., Crisler, M. B., Erwin, A. R., Ford, R., Glazov, A., Golossanov, A., Graham, G., Graham, J., Hagan, K., Halkiadakis, E., Hanagaki, K., Hidaka, S., Hsiung, Y. B., Jejer, V., Jennings, J., Jensen, D. A., Kessler, R., Kobrak, H. G. E., LaDue, J., Lath, A., Ledovskoy, A., McBride, P. L., McManus, A. P., Mikelsons, P., Monnier, E., Nakaya, T., Nauenberg, U., Nelson, K. S., Nguyen, H., O'Dell, V., Pang, M., Pordes, R., Prasad, V., Qiao, C., Quinn, B., Ramberg, E. J., Ray, R. E., Roodman, A., Sadamoto, M., Schnetzer, S., Senyo, K., Shanahan, P., Shawhan, P. S., Slater, W., Solomey, N., Somalwar, S. V., Stone, R. L., Suzuki, I., Swallow, E. C., Swanson, R. A., Taegar, S. A., Tesarek, R. J., Thomson, G. B., Toale, P. A., Tripathi, A., Tschirhart, R., Wah, Y. W., Wang, J., White, H. B., Whitmore, J., Winstein, B., Winston, R., Wu, J.-Y., Yamanaka, T. & Zimmerman, E. D. Observation of direct CP violation in $K_{S,L} \to \pi\pi$ decays. *Phys. Rev. Lett.* **83**, 22–27 (1999).

[35] Fanti, V. *et al.* A new measurement of direct CP violation in two pion decays of the neutral kaon. *Physics Letters B* **465**, 335 – 348 (1999).

[36] Aubert, B. *et al.* Direct CP violating asymmetry in $B^0 \to K^+\pi^-$ decays. *Phys. Rev. Lett.* **93**, 131801 (2004).

[37] Chao, Y. *et al.* Improved measurements of the partial rate asymmetry in $B \to hh$ decays. *Phys. Rev. D* **71**, 031502 (2005).

[38] Aaij, R. *et al.* Evidence for CP violation in time-integrated $D^0 \to h^-h^+$ decay rates. *Phys. Rev. Lett.* **108**, 111602 (2012).

[39] Aaij, R. *et al.* First evidence of direct CP violation in charmless two-body decays of B_s^0 mesons. *Phys. Rev. Lett.* **108**, 201601 (2012).

[40] Hudson, J. J., Kara, D. M., Smallman, I. J., Sauer, B. E., Tarbutt, M. R. & Hinds, E. A. Improved measurement of the shape of the electron. *Nature* **473**, 493–496 (2011).

[41] Lüders, G. Proof of the TCP theorem. *Annals of Physics* **2**, 1 – 15 (1957).

[42] Beringer, J. *et al.* Review of particle physics. *Phys. Rev. D* **86**, 010001 (2012). Particle Data Group.

[43] DiSciacca, J., Marshall, M., Marable, K., Gabrielse, G., Ettenauer, S., Tardiff, E., Kalra, R., Fitzakerley, D. W., George, M. C., Hessels, E. A., Storry, C. H., Weel, M., Grzonka, D., Oelert, W. & Sefzick, T. One-particle measurement of the antiproton magnetic moment. *Phys. Rev. Lett.* **110**, 130801 (2013).

[44] Gibbons, L. K., Barker, A. R., Briere, R. A., Makoff, G., Papadimitriou, V., Patterson, J. R., Schwingenheuer, B., Somalwar, S. V., Wah, Y. W., Winstein, B., Winston, R., Woods, M., Yamamoto, H., Bock, G. J., Coleman, R., Enagonio, J., Hsiung, Y. B., Ramberg, E. J., Stanfield, K., Tschirhart, R., Yamanaka, T., Swallow, E. C., Gollin, G. D., Karlsson, M., Okamitsu, J. K., Debu, P., Peyaud, B., Turlay, R. & Vallage, B. CP and CPT symmetry tests from the two-pion decays of the neutral kaon with the Fermilab E731 detector. *Phys. Rev. D* **55**, 6625–6715 (1997).

[45] Gabrielse, G., Khabbaz, A., Hall, D. S., Heimann, C., Kalinowsky, H. & Jhe, W. Precision mass spectroscopy of the antiproton and proton using simultaneously trapped particles. *Phys. Rev. Lett.* **82**, 3198–3201 (1999).

[46] DiSciacca, J. & Gabrielse, G. Direct measurement of the proton magnetic moment. *Phys. Rev. Lett.* **108**, 153001 (2012).

[47] Marshall, M. & Marable, K. Private communication.

[48] Colladay, D. & Kostelecký, V. A. Lorentz-violating extension of the standard model. *Phys. Rev. D* **58**, 116002 (1998).

[49] Bluhm, R., Kostelecký, V. A. & Russell, N. Testing CPT with anomalous magnetic moments. *Phys. Rev. Lett.* **79**, 1432–1435 (1997).

[50] Bluhm, R., Kostelecký, V. A. & Russell, N. CPT and Lorentz tests in Penning traps. *Phys. Rev. D* **57**, 3932–3943 (1998).

[51] Dehmelt, H., Mittleman, R., Van Dyck, Jr., R. S. & Schwinberg, P. Past electron-positron $g-2$ experiments yielded sharpest bound on CPT violation for point particles. *Phys. Rev. Lett.* **83**, 4694–4696 (1999).

[52] Schwinberg, P. B., R. S. Van Dyck, J. & Dehmelt, H. G. New comparison of the positron and electron g factors. *Phys. Rev. Lett.* **47**, 1679–1682 (1981).

[53] Shi, W., Redshaw, M. & Myers, E. G. Atomic masses of ^{32,33}S, ^{84,86}Kr, and ^{129,132}Xe with uncertainties $\leq$0.1 ppb. *Phys. Rev. A* **72**, 022510 (2005).

[54] Dilling, J., Baartman, R., Bricault, P., Brodeur, M., Blomeley, L., Buchinger, F., Crawford, J., Lpez-Urrutia, J. C., Delheij, P., Froese, M., Gwinner, G., Ke, Z., Lee, J., Moore, R., Ryjkov, V., Sikler, G., Smith, M., Ullrich, J. & Vaz, J. Mass measurements on highly charged radioactive ions, a new approach to high precision with TITAN. *International Journal of Mass Spectrometry* **251**, 198 – 203 (2006).

[55] Brodeur, M., Ryjkov, V., Brunner, T., Ettenauer, S., Gallant, A., Simon, V., Smith, M., Lapierre, A., Ringle, R., Delheij, P., Good, M., Lunney, D. & Dilling, J. Verifying the accuracy of the TITAN Penning-trap mass spectrometer. *International Journal of Mass Spectrometry* **310**, 20 – 31 (2012).

[56] Gabrielse, G. & MacKintosh, F. C. Cylindrical Penning traps with orthogonalized anharmonicity compensation. *Int. J. Mass Spectrom. Ion Processes* **57**, 1–17 (1984).

[57] Gabrielse, G., Haarsma, L. & Rolston, S. L. Open-endcap Penning traps for high-precision experiments. *Int. J. Mass Spectrom. Ion Processes* **88**, 319–332 (1989). Ibid. **93**, 121 (1989).

[58] Gabrielse, G., Bowden, N. S., Oxley, P., Speck, A., Storry, C. H., Tan, J. N., Wessels, M., Grzonka, D., Oelert, W., Schepers, G., Sefzick, T., Walz, J., Pittner, H., Hänsch, T. W. & Hessels, E. A. Background-free observation of cold antihydrogen with field-ionization analysis of its states. *Phys. Rev. Lett.* **89**, 213401 (2002).

[59] Gabrielse, G., Larochelle, P., Le Sage, D., Levitt, B., Kolthammer, W. S., McConnell, R., Richerme, P., Wrubel, J., Speck, A., George, M. C., Grzonka, D., Oelert, W., Sefzick, T., Zhang, Z., Carew, A., Comeau, D., Hessels, E. A., Storry, C. H., Weel, M. & Walz, J. Antihydrogen production within a Penning-Ioffe trap. *Phys. Rev. Lett.* **100**, 113001 (2008).

[60] Gabrielse, G., Kalra, R., Kolthammer, W. S., McConnell, R., Richerme, P., Grzonka, D., Oelert, W., Sefzick, T., Zielinski, M., Fitzakerley, D. W., George, M. C., Hessels, E. A., Storry, C. H., Weel, M., Müllers, A. & Walz, J. Trapped antihydrogen in its ground state. *Phys. Rev. Lett.* **108**, 113002 (2012).

[61] Guise, N., DiSciacca, J. & Gabrielse, G. Self-excitation and feedback cooling of an isolated proton. *Phys. Rev. Lett.* **104**, 143001 (2010).

[62] Guise, N. *Spin-Flip Resolution Achieved with a One-Proton Self-Excited Oscillator*. Ph.D. thesis, Harvard University (2012). (advisor: G. Gabrielse).

[63] Goldman, J. & Gabrielse, G. Optimized planar Penning traps for quantum-information studies. *Phys. Rev. A* **81**, 05235 (2010).

[64] Lamata, L., Porras, D., Cirac, J. I., Goldman, J. & Gabrielse, G. Towards electron-electron entanglement in Penning traps. *Phys. Rev. A* **81**, 022301 (2010).

[65] Goldman, J. *Planar Penning Traps with Anharmonicity Compensation for Single-Electron Qubits*. Ph.D. thesis, Harvard University (2011). (advisor: G. Gabrielse).

[66] Gabrielse, G. Relaxation calculation of the electrostatic properties of compensated Penning traps with hyperbolic electrodes. *Phys. Rev. A* **27**, 2277 (1983).

[67] Brown, L. S. & Gabrielse, G. Geonium theory: Physics of a single electron or ion in a Penning trap. *Rev. Mod. Phys.* **58**, 233–311 (1986).

[68] Peil, S. E. *Quantum Jumps Between Fock States of an Ultracold Electron Cyclotron Oscillator*. Ph.D. thesis, Harvard University (1999). (advisor: G. Gabrielse).

[69] Jackson, J. D. *Classical Electrodynamics* (John Wiley & Sons, 1999), third edn.

[70] Hanneke, D. *"Cavity Control in a Single-Electron Quantum Cyclotron: An Improved Measurement of the Electron Magnetic Moment"*. Ph.D. thesis, Harvard University (2007). (advisor: G. Gabrielse).

[71] Brown, L. S. & Gabrielse, G. Precision spectroscopy of a charged particle in an imperfect Penning trap. *Phys. Rev. A* **25**, 2423–2425 (1982).

[72] Dehmelt, H. & Ekstrom, P. Proposed $g - 2/\delta\omega_z$ experiment on single stored electron or positron. In *Bulletin of the American Physical Society*, vol. 18, 727 (1973).

[73] Brown, L. S. Geonium lineshape. *Ann. Phys.* **159**, 62–98 (1985).

[74] D'Urso, B. R. *Cooling and Self-Excitation of a One-Electron Oscillator*. Ph.D. thesis, Harvard University (2003). (advisor: G. Gabrielse).

[75] Van Dyck, R., Moore, F., Farnham, D. & Schwinberg, P. Variable magnetic bottle for precision geonium experiments. *Review of scientific instruments* **57**, 593–597 (1986).

[76] Gabrielse, G. & Dehmelt, H. Geonium without a magnetic bottle - a new generation. In Taylor, B. N. & Phillips, W. D. (eds.) *Precision Measurements and Fundamental Constants II*, vol. 1, 219 (1984).

[77] Van Dyck, Jr., R. S., Schwinberg, P. B. & Dehmelt, H. G. Experiments with single electrons. In Hestenes, D. & Weingartshofer, A. (eds.) *The Electron: New Theory and Experiment*, 239–293 (Kluwer Academic Publishers, Netherlands, 1991).

[78] Odom, B. C. *Fully Quantum Measurement of the Electron Magnetic Moment*. Ph.D. thesis, Harvard University (2004). (advisor: G. Gabrielse).

[79] Gabrielse, G. & Tan, J. Self-shielding superconducting solenoid systems. *J. Appl. Phys.* **63**, 5143–5148 (1988).

[80] Gabrielse, G., Tan, J., Clateman, P., Orozco, L. A., Rolston, S. L., Tseng, C. H. & Tjoelker, R. L. A superconducting system which cancels fluctuations in the ambient magnetic field. *J. Mag. Res.* **91**, 564–572 (1991).

[81] Schwinberg, P. B., Van Dyck, Jr., R. S. & Dehmelt, H. G. Trapping and thermalization of positrons for geonium spectroscopy. *Phys. Lett.* **81A**, 119–120 (1981).

[82] Haarsma, L., Abdullah, K. & Gabrielse, G. Extremely cold positrons accumulated electronically in ultrahigh vacuum. *Phys. Rev. Lett.* **75**, 806–809 (1995).

[83] Haarsma, L. *"Accumulating Positrons in an Ion Trap"*. Ph.D. thesis, Harvard University (1994). (advisor: G. Gabrielse).

[84] Estrada, J., Roach, T., Tan, J. N., Yesley, P. & Gabrielse, G. Field ionization of strongly magnetized Rydberg positronium: A new physical mechanism for positron accumulation. *Phys. Rev. Lett.* **84**, 859–862 (2000).

[85] Hall, D. S. *"Positrons, Antiprotons and Interactions for Cold Antihydrogen"*. Ph.D. thesis, Harvard University (1997). (advisor: G. Gabrielse).

[86] Estrada, J. K. *Cold Trapped Positrons and Progress to Cold Antihydrogen*. Ph.D. thesis, Massachusetts Institute of Technology (2002). (advisor: G. Gabrielse).

[87] Hulett, L. D., Dale, J. M. & Pendyala, S. The effect of source window material and thickness on the intensity of moderated positrons. *Surface and Interface Analysis* **2**, 204–206 (1980).

[88] Massoumi, G., Schultz, P. J., Lennard, W. & Ociepa, J. Positron emission yields for encapsulated ^{22}Na sources. *Nuclear Instruments and Methods in Physics Research Section B: Beam Interactions with Materials and Atoms* **30**, 592 – 597 (1988).

[89] Canter, K. F., Mills, J., A. P. & Berko, S. Efficient positronium formation by slow positrons incident on solid targets. *Phys. Rev. Lett.* **33**, 7–10 (1974).

[90] Mills, J., A. P. Positronium formation at surfaces. *Phys. Rev. Lett.* **41**, 1828–1831 (1978).

[91] Lynn, K. G. & Welch, D. O. Slow positrons in metal single crystals. I. Positronium formation at Ag(100), Ag(111), and Cu(111) surfaces. *Phys. Rev. B* **22**, 99–110 (1980).

[92] Bowden, N. B. *Production of Cold Antihydrogen during the Positron Cooling of Antiprotons*. Ph.D. thesis, Harvard Univ. (2003). (advisor: G. Gabrielse).

[93] Musket, R., McLean, W., Colmenares, C., Makowiecki, D. & Siekhaus, W. Preparation of atomically clean surfaces of selected elements: A review. *Applications of Surface Science* **10**, 143 – 207 (1982).

[94] Wineland, D. J. & Dehmelt, H. G. Principles of the stored ion calorimeter. *J. Appl. Phys.* **46**, 919–930 (1975).

[95] D'Urso, B., Van Handel, R., Odom, B., Hanneke, D. & Gabrielse, G. Single-particle self-excited oscillator. *Phys. Rev. Lett.* **94**, 113002 (2005).

[96] DiSciacca, J. *First Single Particle Measurements of the Proton and Antiproton Magnetic Moments*. Ph.D. thesis, Harvard University (2013). (advisor: G. Gabrielse).

[97] Macalpine, W. & Schildknecht, R. Coaxial resonators with helical inner conductor. *Proceedings of the IRE* **47**, 2099–2105 (1959).

[98] Gabrielse, G., Estrada, J., Tan, J., Yesley, P., Bowden, N., Oxley, P., Roach, T., Storry, C., Wessels, M., Tan, J., Grzonka, D., Oelert, W., Schepers, G., Sefzick, T., Breunlich, W., Cargnelli, M., Fuhrmann, H., King, R., Ursin, R., Zmeskal, J., Kalinowsky, H., Wesdorp, C., Walz, J., Eikema, K. & Hnsch, T. First positron cooling of antiprotons. *Physics Letters B* **507**, 1 – 6 (2001).

[99] Oxley, P. K. *Production of Slow Antihydrogen from Cold Antimatter Plasmas*. Ph.D. thesis, Harvard University (2003). First Single Particle Measurements of the Proton and Antiproton Magnetic Moments.

[100] Oxley, P., Bowden, N., Parrott, R., Speck, A., Storry, C., Tan, J., Wessels, M., Gabrielse, G., Grzonka, D., Oelert, W., Schepers, G., Sefzick, T., Walz, J., Pittner, H., Hnsch, T. & Hessels, E. Aperture method to determine the density and geometry ofantiparticle plasmas. *Physics Letters B* **595**, 60 – 67 (2004).

[101] Dorr, J. Private communication.

[102] Tan, J. & Gabrielse, G. Synchronization of parametrically pumped electron oscillators with phase bistability. *Phys. Rev. Lett.* **67**, 3090–3093 (1991).

[103] Tan, J. & Gabrielse, G. Parametrically pumped electron oscillators. *Phys. Rev. A* **48**, 3105–3122 (1993).

[104] Tan, J. N. *Cooperative Behavior in Cavity-cooled, Parametrically-pumped Electron Oscillators*. Ph.D. thesis, Harvard University (1992). First Single Particle Measurements of the Proton and Antiproton Magnetic Moments.

[105] Novitski, E. Private communication.

[106] Garrett, M. W. Calculation of fields, forces, and mutual inductances of current systems by elliptic integrals. *Journal of Applied Physics* **34**, 2567–2573 (1963).